Superlattices in charge

Band occupation and electron transport in 2D PbSe and CdSe superlattices

PhD thesis, Universiteit Utrecht

Superlattices in charge
Band occupation and electron transport in 2D PbSe and CdSe superlattices

Maryam Alimoradi Jazi, March 2019

Printed by: Ipskamp Printing || proeschriften.net

ISBN: 978-94-028-1395-1

Superlattices in charge

Band occupation and electron transport in 2D PbSe and CdSe superlattices

Lading gedragen superstructuren

Bandbezetting en elektronengeleiding in 2D PbSe en CdSe superstructuren
(met een samenvatting in het Nederlands)

Proefschrift

ter verkrijging van de graad van doctor aan de Universiteit Utrecht op gezag van de rector magnificus, prof. dr. H.R.B.M. Kummeling, ingevolge het besluit van het college voor promoties in het openbaar te verdedigen

op maandag 25 maart 2019

des middags te 2.30 uur

door

Maryam Alimoradi Jazi

geboren op 22 december 1984 te Isfahan, Iran

Promotoren:

Prof. dr. D.A.M. Vanmaekelbergh

Copromotor:

Dr. A. J. Houtepen

This thesis was accomplished with financial support from the Marie Skłodowska Curie Action Innovative Training Network PHONSI- Nanophotonics by Nanocrystals and from the European Research Council under the European Union's Seventh Framework Programme (Horizon 2020)/ ERC advanced grant agreement "First step" under grant number 692691.

Table of Contents

Chapter 1

Introduction and outline of this thesis

Abstract

In the past few decades, research into the field of nanoscience has led to the invention of many new materials with a vast range of applications. Especially semiconductor nanomaterials emerge in new fields of nanoscience and hold promise for information technology, optoelectronics, energy sources and medical treatments. For that reason, there has been substantial interest in the preparation and characterization of colloidal semiconductor nanocrystals. In my PhD thesis work, I used colloidal nanocrystals to prepare 2D semiconductor nanostructures with nanoscale square and hexagonal periodicity. For these nanostructured 2D semiconductors, remarkable electronic band structures have been predicted. This chapter provides an introduction to the thesis work. A brief overview of the use of the nanoparticles throughout history is given. Further, I introduce several more modern developments. I conclude with an outline of the chapters presented in this thesis.

1

1.1 Introduction

Nano means "billionth", so a nanometer is one billionth of a meter. We live on the scale of meters and kilometers, so it is quite difficult for us to imagine an object that small. The following examples may hopefully help to visualize the nanoscale concept. A piece of paper is roughly 100000 nanometers thick. If you cut one of your hairs along the length in 100000 pieces, each piece is one nanometer. A nanocrystal has at least one dimension on a nanometer scale. The atoms that compose such a nanocrystal are arranged in a regular, crystalline structure.

1.2 Nanoparticles in previous times

Although nanoparticles are associated with modern science, they emerged throughout history and were used unintentionally. The fourth century Roman Lycurgus cups, made from dichroic glass (Figure 1.1a), is an astonishing example: the dichroic effect that is visible in the cup is due to small amounts of gold and silver nanoparticles dispersed in colloidal form throughout the glass. These cups appear green during daylight. When the light shines through the glass, the cup turns into a ruby color.[1] Another example is luster decoration used as a pottery painting technique, which originated in the Muslim world between the 4th and 8th centuries AD.[2] This luster is caused by a metallic film of silver and copper nanoparticles in the glassy matrix of the ceramic glaze. Figure 1.1b shows a 13th-century bowl from Kashan, Iran. Ancient Egyptians used a mixture of lead oxide and slaked lime with a small amount of water to form PbS nanoparticles to produce hair dyes.[3] Successive applications on gray or light hair give rise to the black color illustrated in Figure 1.1c.

1.3 Modern application of nanoparticles

The examples mentioned above involved ancient and probably unintentional applications of metallic nanoparticles. Genuine nanoscience and technology, however, started to flourish only recently. Michael Faraday provided the first scientific description of the optical properties of nanometer-scale metals in 1857.[4] The American physicist, Richard

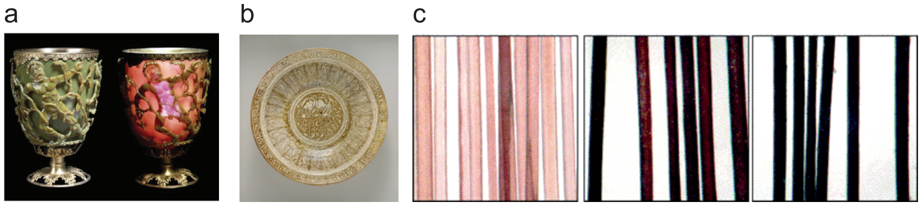

Figure 1.1. Use of nanoparticles throughout history. (a) A fourth century Roman Lycurgus cup from dichroic glass which appears green during daylight (left) and turns into a ruby color (right) when the light shines through the glass. The dichroic effect is achieved by making the glass with small amounts of gold and silver nanoparticles dispersed in colloidal form throughout the glass material. Reused with permission from reference [1]. (b) A 13th-century lustreware bowl from Kashan, Iran. This luster is caused by a metallic film of silver and copper nanoparticles in the glassy matrix of the ceramic glaze. Reused from https://www.metmuseum.org. (c) Ancient Egyptians used a mixture of lead oxide and slaked lime with a small amount of water to form PbS nanoparticles to produce hair dyes. Successive applications on gray or light hair give rise to the black color. Reused with permission from reference [3].

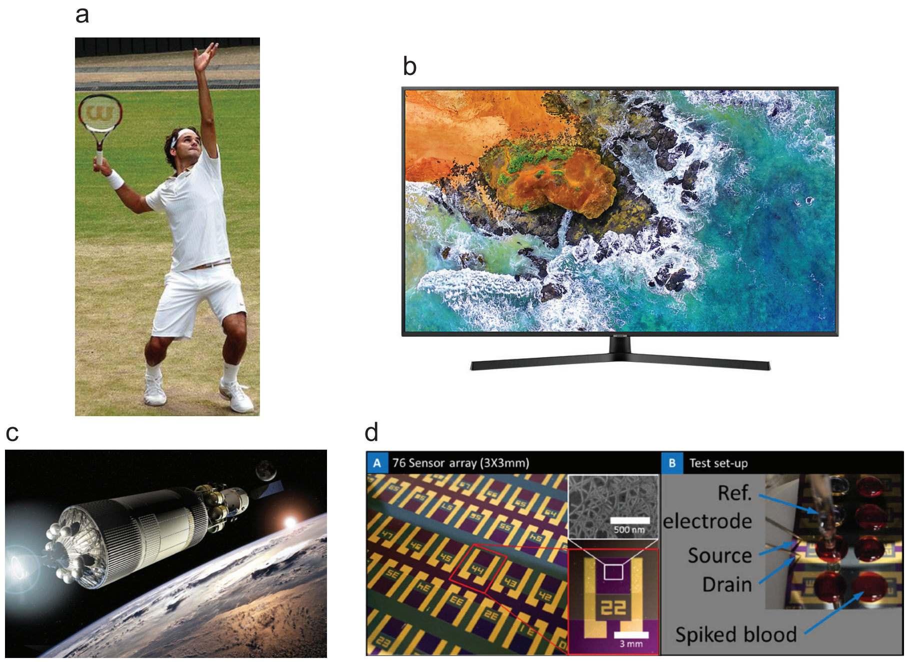

Figure 1.2. Modern applications of nanoparticles. (a) Roger Federer at Wimbledon 2009 with a Wilson K Factor racquet containing silica nanoparticles. (b) Samsung television screens containing semiconductor nanocrystals. (c) A NASA space vehicle using carbon nanotubes for its shielding systems. (d) The optical image of 76-element single wall carbon nanotube sensor arrays and the test set-up used to identify metastatic cancer cells in a small amount of blood by researchers at Worcester Polytechnic Institute. Reproduced with permission from ref [6].

Feynman (1918-1988), is widely credited for his - for that time - futuristic insights and predictions on the use of atoms to create nanostructures, to be used as bits of information. Some science historians see Feynman as the father of nanoscience and technology as we know today.[5]

During the last decades, nanoparticles have been investigated extensively, with applications in diverse fields such as medicine, optics and electronics. Even sporting goods have wandered into the nano realm. Adding silicon dioxide nanoparticles to the frame of tennis racquets increases their strength and stability (Figure 1.2a). Nowadays, colloidal semiconductor nanocrystals are used as phosphors in LEDs and television screens to increase the range of colors and the brightness (Figure 1.2b). Researchers at the National Aeronautics and Space Administration (NASA) are employing materials made from carbon nanotubes to shield the personnel and sensitive electronic equipment on a space vehicle from radiation damage (Figure 1.2c).[6] Mechanical engineers at Worcester Polytechnic Institute developed a chip from carbon nanotubes which can trap and identify metastatic cancer cells in a small amount of blood from a cancer patient (Figure 1.2d).[7]

In this thesis, we use colloidal semiconductor lead selenide (PbSe) and cadmium selenide

(CdSe) semiconductor nanocrystals as building blocks to form extended semiconductor sheets of a nanocrystal monolayer in thickness and with a square or trigonal periodicity of voids, with the eventual goal of developing novel optoelectronic devices.

1.4 Outline of this thesis

The thesis is structured as follows:

Chapter 2 provides the fundamental theory behind the colloidal nanocrystals (NCs) and their opto-electronic properties. Furthermore, the process of self-assembly of NCs at the NC dispersion/air interface followed by oriented attachment of the NCs resulting in two-dimensional superlattices is presented. Finally, we describe electrochemical gating, which has been used throughout this thesis work as the main method to characterize the optoelectronic properties of NC superlattices.

Chapter 3 presents the light absorption properties of nanocrystal monolayer PbSe and CdSe superlattices with a square and honeycomb geometry. We demonstrate that the magnitude of the light absorption (*i.e.* the absorptivity) by a single nanocrystal sheet on quartz has a specified value, proportional to the fine structure constant, regardless of the superlattice geometry and material. One additional layer of the superlattice enhances the absorptivity by a factor of two. We have incorporated the PbSe honeycomb superlattices in a photoconductive device. The responsivity spectrum closely reproduces the light absorption spectrum, though with a better signal-to-noise ratio.

In **Chapter 4** we discuss the injection of charge carriers into PbSe superlattices with a square geometry, which were self-assembled on top of a liquid substrate. We have used three variations of liquid electrolyte gating. By means of a differential absorption experiment and a differential capacitance measurement the carrier density is quantified. The superlattice conductivity was determined by two- and four-probe conductance measurements in a Hall-bar geometry.

Chapter 5 presents a study of the band occupation and charge transport in PbSe honeycomb superlattices at room temperature, using both electrochemical gating and terahertz spectroscopy. The electron mobility obtained from the two methods was similar. The magnitude of the mobility and the frequency dependence of the terahertz function indicate that, despite the strong electronic coupling between the nanocrystals in these superstructures, the mobility is limited by scattering on superlattice imperfections.

In **Chapter 6** we show that the rock salt square and honeycomb superlattices of PbSe NCs are transformed to wurtzite/zinc blende core/shell superlattices of CdSe *via* cation exchange. Further, we incorporated the CdSe superlattices in an electrochemical gating device and investigated the band occupation and charge transport properties of the CdSe superlattices.

In **Chapter 7** we give a short summary of the results of this thesis and an outlook on possible future research on superlattices.

References

1. Freestone, I., Meeks, N., Sax, M. & Higgitt, C. The Lycurgus Cup - A Roman nanotechnology. *Gold Bull.* **40**, 270–277 (2007).
2. Pradell, T., Molera, J., Smith, A. D. & Tite, M. S. The invention of lustre: Iraq 9th and 10th centuries AD. *J. Archaeol. Sci.* **35**, 1201–1215 (2008).
3. Walter, P. *et al.* Early use of PbS nanotechnology for an ancient hair dyeing formula. *Nano Lett.* **6**, 2215–2219 (2006).
4. Faraday, M. X. The Bakerian Lecture. Experimental relations of gold (and other metals) to light. *Philos. Trans. R. Soc. London.* **147**, 145–181 (1857).
5. Feynman, R. P., Leighton, R. *The Feynman Lectures on Physics.* (1964).
6. Chen, B., Alto, P. Radiation Shielding Systems Using Nanotechnology. (2011). *US-Patent-7*,923,709.
7. Khosravi, F. *et al.* Static micro-array isolation, dynamic time series classification capture and enumeration of spiked breast cancer cells in blood : the nanotube - CTC chip. *Nanotechnology* **27**, 1–18 (2016).

Chapter 2

Semiconductor nanocrystals, self-assembly, oriented attachment and electrochemical gating

Abstract

Semiconductor nanocrystals (NCs) constitute an important class of materials for a variety of optoelectronic applications. Since the mid-1990s, colloidal semiconductor NCs have become a masterpiece of semiconductor research due to their unprecedented compositional and morphological tunability. This chapter, at first, addresses some basic aspects of colloidal NCs and their optoelectronic properties. The NCs can also be used as building blocks to create two- and three-dimensional structures through NC self-assembly. The thermodynamics driving this self-assembly is discussed in terms of inter-particle interactions. Further, we discuss the basic aspects of NC assembly at the dispersion/air interface followed by oriented attachment of the NCs. This results in 2D NC superlattices, here in fact atomically coherent 2D chalcogenide semiconductors, with a square or honeycomb geometry on the nanoscale. Finally, we discuss how such superlattices can be incorporated in transistor-type devices with electrochemical gating. This is the main technique used in this thesis to characterize the optoelectronic properties of NC superlattices.

2.1 Colloidal semiconductor nanocrystals

Semiconductor nanocrystals (NCs) have optical and electronic properties that make them promising materials with potential electronic, optoelectronic and thermoelectric applications. The unusual properties of semiconductor NCs are a consequence of their dimensionality on a nanoscale. Quantum confinement, the effect for which electron and hole wave functions are influenced by the physical boundaries of the NC particle, lies at the origin of these unusual properties. This confinement also makes the semiconductor NC properties size- and shape dependent.

In this section, we first discuss the origin of the size-dependent properties of semiconductor NCs. Next, we describe various examples of classes of semiconductor NCs. At last, we show how semiconductor NCs can self-assembly into superstructures.

2.1.1 Nanoscale size effects

A bulk semiconductor has groups of quasi-continuous delocalised energy levels, called bands. These bands are separated by energy regions without any allowed state, called gaps. The formation of bands and gaps in a bulk semiconductor can be understood by the Linear Combination of Atomic Orbitals (LCAO) theory: A large number of atoms in a bulk semiconductor (around $10^{22}/cm^3$) contribute orbitals to form bonding, non-bonding and antibonding molecular orbitals (MOs) by linear combination. When a large number of atoms come together to form a solid, the atomic orbitals combine. Due to the large number of atoms, the number of MOs is very large and thus they are very closely spaced in energy. Therefore, the collection of energy states is better described as a quasi-continuum or a band. In a semiconductor, the energy band that is occupied by electrons is called valence band (VB) and the unoccupied energy band is called conduction band (CB). Between the CB and VB is an energy region that does not allow the existence of any states. This is the band gap, with energy E_g. The Fermi level is the energy where the orbitals change from filled to empty, and this lies for a semiconductor within the bandgap. Transitions will take place around the Fermi level, which makes the bandgap the region of interest in a semiconductor. The optoelectronic properties of semiconductors are determined by allowed transitions of electrons between the valence and conduction bands.

As stated above, the optoelectronic properties of materials change when they reach dimensions on the nanoscale and this effect is called quantum confinement. Firstly, the quantum confinement effect can be explained either by LCAO theory or by the nearly free electron model. A semiconductor NC contains much fewer atoms (10^2 to 10^5) compared to the bulk materials. Therefore, following LCAO theory, fewer orbitals combine and, as a result, fewer energy states are formed. This leads to the discrete density of electronic states (DOS) near the edges of the VB and the CB in semiconductor NCs. Furthermore, by decreasing the size of semiconductor NCs, it is possible to decrease the number of atoms present (and thus the number of MOs); therefore, the energy separation between the discrete energy in the VB and the CB increases and the band gap (E_g) of the NC becomes larger, as illustrated in Figure 2.1a.

Secondly, the increase in the bandgap by decreasing the size of the NCs can be easily understood from the nearly free electron model. An electron can be excited from the

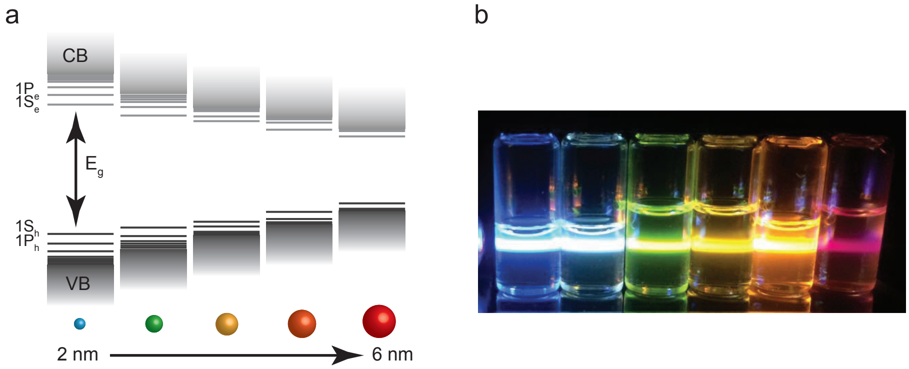

Figure 2.1. Quantum confinement effect in CdSe nanocrystals. (a) The band gap of CdSe nanocrystals (NCs) increases by decreasing the size of the NCs due to quantum confinement. This also results in discrete levels with increasing separation near the band edges. (b) A photograph of CdSe NCs dispersions with different sizes under UV illumination showing blue to red photoluminescence. Photograph courtesy of Federico Montanarella.

VB to the CB by absorbing a photon of sufficient energy, promoting an electron from a filled valence level into an empty conduction level. In small NCs, the electron and hole wave functions are confined in the limited space of the nanocrystal. There is also a Coulomb attraction between the electron and the hole. The electron-hole excitation can be described as a confined exciton. The exciton Bohr radius (a_0) reflects the size of an electron-hole pair held together by Coulomb attraction in a macroscopic semiconductor. Semiconductor NCs are smaller than the exciton Bohr radius, which is why one speaks of quantum confined excitons.[1] The smaller the NCs, the stronger the confinement and hence, the larger the bandgap. The profound impact of quantum confinement on the optical properties of semiconductor NCs is presented in Figure 2.1b. The emission color of the CdSe QDs can be varied from blue to red by increasing the size of the QDs from 2 to 6 nm.[2]

The surface area-to-volume ratio may also influence the optoelectronic properties of colloidal semiconductor NCs. When the size of the NCs is reduced, there are relatively more atoms present on the surface. Surface atoms can have dangling orbitals that result in localized states. Such localized states can have energy levels in the band gap, enhancing non-radiative electron-hole recombination, lowering the photoluminescence quantum yield.[2,3] It has been one of the major victories in nanocrystal science that this undesired surface recombination has been reduced considerably with (in)organic ligand molecules attached to the surface atoms or epitaxial inorganic shells, *i.e.* electronically passivation of the dangling orbitals.[4–10]

2.1.2 Nanocrystal dimensionality

The quantum confinement effect, which was discussed in the previous section, depends strongly on the NCs dimensionality. If the exciton is confined in all directions, a colloidal quantum dot (0D) is obtained. If the exciton experiences a two-dimensional confinement, the NC will be referred as quantum rod or quantum wire (1D). In a quantum well (2D),

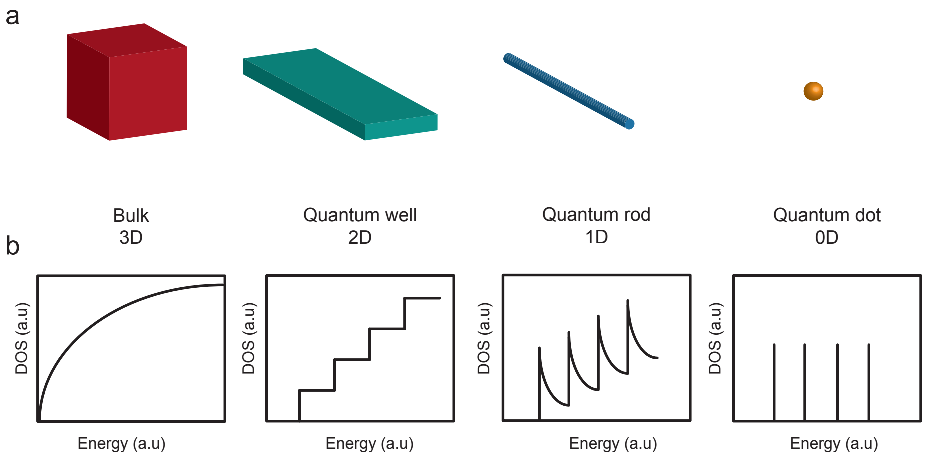

Figure 2.2. Nanocrystal dimensionality and the density of electronic states. (a) Schematic illustration of a macroscopic semiconductor crystal and NCs with different dimensionality. (b) The density of electronic states (DOS) for the different cases. The DOS changes from sharp peaks (0D) to a step-like dependence for a quantum well. The bulk semiconductor shows a quasi-continuous band of energy levels increasing with the square root of the energy.

the exciton is confined only in the thickness direction. The electronic density of states (DOS) demonstrates clearly the difference between the bulk, quantum well, quantum rod and quantum dots (Figure 2.2). For a quantum well, the DOS changes from a square root dependence (for bulk) to a step-like feature. Quantum rods show $E^{-1/2}$ dependency in each discrete group of energy levels, while a QD has discrete energy levels.

The research presented in this thesis deals with atomically coherent 2D superlattices, formed from Pb- and Cd- chalcogenide nanocrystals that are epitaxially connected. The superlattices show a square or a honeycomb (hexagonal) arrangement of the NCs.[11,12] These materials are a very interesting class that is somehow in between quantum dots and quantum well, but with a specific band structure that depends on the symmetry of the nanocrystal arrangement. Quantum confinement prevails in the direction perpendicular to the nanocrystal sheet. Atomistic tight-binding calculations have shown that, provided that the coupling between the NCs is strong enough, a novel material emerges with a geometry-specific band-structure.[13,14] In that respect, it has been predicted that 2D superlattices with a honeycomb geometry show Dirac-type valence and conduction bands, combining semiconductor properties with those of graphene.[14,15] The formation mechanism of the superlattices will be explained in detail below.

2.1.3 Self-assembly and oriented attachment

Colloidal NCs are able to form 3D and (quasi) 2D self-assembled superlattices. Several methods have been developed for the formation of single-component and binary superlattices since the first self-assembly of CdSe NCs superlattices was reported in 1995 by Murray *et al.*[16] Here, we explain how these NC superlattices form and what the key driving forces are.

The formation of the superlattices from a NC suspension is a spontaneous process under certain experimental conditions. At constant temperature and pressure, the change in the Gibbs free energy of the suspension during colloidal crystallization is:

$$\Delta G = \Delta H - T\Delta S \qquad \text{(Eq. 2.1)}$$

ΔG is the change in Gibbs free energy, ΔH is the change in enthalpy, T is the temperature and ΔS is the change in entropy of the system, here the NC suspension. The enthalpy contribution accounts for the attraction between the NCs in the superlattice with respect to those in the suspension.

The colloidal NCs studied here are capped by organic molecules rendering colloidal stability in an apolar organic solvent (for example toluene and hexane). These capping molecules keep the cores of the NCs at a considerable distance; in such a way the core-core attraction remains weak, preventing particle aggregation. The magnitude of the interaction energy between two semiconductor NCs is below the thermal energy k_BT. The semiconductor NCs in such an ideal solvent can be considered as hard spheres, for which the enthalpy component ΔH is close to zero. A system undergoes a spontaneous crystallization if there is a lowering in Gibbs free energy $\Delta G<0$. Thus the entropy of the particles in the colloidal crystal must be larger than that in the dense suspension ($\Delta S>0$). This can be understood by looking at free volume per NC which has a small value in a chaotic dense dispersion compared to the ordered superlattice of the NCs with the same density.[17,18]

Analogous to the description above, the spontaneous colloidal crystallization from a colloid suspension can also be described using the chemical potential μ of the NCs in the suspension:

$$\mu = \mu^0 + k_B T \ln(c/c^0) \qquad \text{(Eq. 2.2)}$$

In order to initiate spontaneous colloidal crystallization from a colloid suspension, the NCs should get a high chemical potential in the suspension. Therefore, either the standard chemical potential μ^0 in solution or, alternatively, the concentration c should be increased. Adding an anti-solvent to a dispersion increases the potential energy per particle and as a result μ^0. Superlattice formation by adding an anti-solvent has been studied in several works.[16,19–21] Generally, three-dimensional crystals are formed by homogeneous nucleation in the suspension. Evaporation of the solvent increases the chemical potential *via* the nanoparticle concentration. Several methods have been used to form 2D and 3D superlattices from the NC dispersion based on the evaporation of the solvent, such as dip-coating,[22] spin-coating,[23] Langmuir-Blodgett,[24–29] doctor blading,[30] solid substrate tilted with respect to suspension/air interface[20,31–36] and drop casting on a (functionalized) solid or an immiscible liquid substrate.[16,37–45]

The highly ordered 2D PbSe and CdSe superlattices studied in this thesis, with square and honeycomb geometry, are formed by using the liquid substrate procedure pioneered by Murray *et al.*.[41] The NCs do not dissolve in the liquid substrate, but adsorb at liquid/air interface. The process is outlined in Figure 2.3a. We use a suspension of truncated

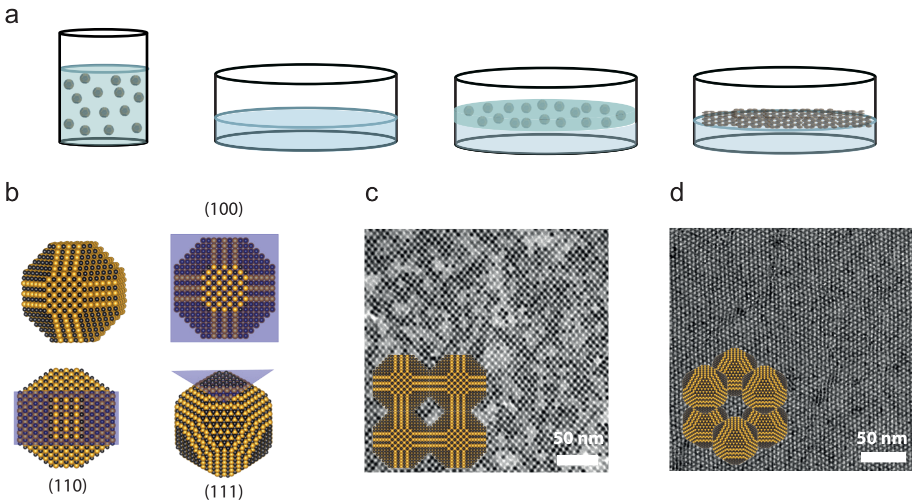

Figure 2.3. (a) Schematic representation of the experimental setup for self-assembly and oriented attachment of PbSe NCs. We use a suspension of truncated PbSe nanocubes. The suspension is drop casted on an immiscible liquid substrate (ethylene glycol) after which the solvent evaporates and the NCs attach via their {100} facets and form 2D square and honeycomb superlattices. (b) Atomic scheme of the truncated cubes of PbSe NCs with 6 {100}, 12 {110} and 8 {111} planes. The black (yellow) spheres represent the Pb (Se) atoms. (c) TEM image of a part of a PbSe square superlattice. The PbSe NCs are attached using the four vertical {100} facets, as depicted in the inset. (d) TEM image of a part of a PbSe buckled silicene-type honeycomb superlattice. The PbSe NCs are attached along the {100} facets. Inset: Atomistic scheme of six NCs in the honeycomb superlattice with the NCs oriented with their [111] axis perpendicular to the substrate. Atomic scheme courtesy of Joep Peters.

PbSe nanocubes with 6 {100}, 12 {110} and 8 {111} facets illustrated in Figure 2.3b. The suspension is drop casted on an immiscible liquid substrate (ethylene glycol) after which the solvent evaporates. The NCs attach *via* their {100} facets and form 2D square and honeycomb superlattices with just a monolayer thickness (Figure 2.3c and d).[11,12,46,47] In the square superlattices, the four vertical {100} facets are used in epitaxial attachment, as depicted in the inset of the Figure 2.3c. In the honeycomb superlattices the attachment occurs via 3 of the {100} facets per nanocrystal and the [111] axis is perpendicular to the interface surface (Figure 2.3d inset). An *in-situ* X-ray scattering study by Geuchies *et al.* revealed that the formation involves a sequence of phase transformations, from a hexagonal NC monolayer through a quasi-hexagonal intermediate phase transforming into a square superlattice, finally.[44] Whitham *et al.* described how the underlying entropic and enthalpic interactions as well as the kinetics of assembly and attachment influence the formation of epitaxially connected superstructures.[48]

After solvent evaporation, the superlattices float on the liquid substrate, and can then be transferred to a TEM grid, a quartz substrate, or a transistor-type device for structural, optical and electrical characterization, respectively. The PbSe superlattices can also be transformed into CdSe superlattices *via* a cation exchange reaction.[49,50] In the cation exchange reaction, the Pb cations are exchanged with Cd cations from a solution contacting the superlattice. This chemical transformation can be complete and preserves the nanoscale square or honeycomb geometry of the superlattice.

2.2 Structural, optical and electrical characterization of the superlattices

For the first structural characterization of the superlattices, conventional bright-field transmission electron microscopy (TEM) is generally used: a collimated beam of electrons is transmitted through the sample to form an image. To obtain high-resolution images, scanning transmission electron microscopy (STEM) in high-angle annular dark-filed (HAADF) mode is used where the images are formed by collecting scattered electrons with an annular dark-field detector.[51]

In Chapter 3 of this thesis, we study the optical absorption properties of 2D square and honeycomb superlattices. Single layers of 2D systems appear to have a universal value of the light absorptivity defined by fundamental constants.[52,53] The theory behind this unique phenomenon is explained in the following section. The optical properties of the honeycomb and square superlattices are characterized with absorption spectroscopy and photoconductivity measurements, measuring the enhancement of the electrical conductivity of the superlattices upon electron and hole photogeneration.

To study the transport properties of the superlattices, we incorporate single layers of superlattices into an electrochemical-gated transistor and study electron injection by measurement of the differential capacitance and the differential absorption (Chapters 4, 5 and 6). This technique has been exploited by several groups to study many different properties of NCs such as absolute energy levels,[54,55] charge associated absorption changes,[56] fluorescence quenching,[56,57] blinking characteristics,[58,59] trap states[60,61] and steady-state conductivity.[62–64] The transport characteristics at controlled conduction band occupation have been measured too. The principles of the electrochemical gating and the experimental details will be described in section 2.4.

Furthermore, we applied terahertz (THz) photoconductivity spectroscopy on PbSe honeycomb superlattices to investigate the influence of imperfections in the honeycomb superlattices on charge transport (Chapter 5). The THz experimental procedure involves detection of charges and excitons with a single-cycle THz field. In general, photoexcitation of a semiconductor leads to formation of free mobile charges that can coexist with excitons.[65–67] The THz scattering and absorption is measured, detecting excitons or free carriers, and how the latter move through the superlattice.

2.3 Light absorption by 2D systems

There are few phenomena in condensed matter physics which are defined just by a few fundamental constants and are absolutely independent of material parameters. Two of these phenomena are, for example, the resistivity quantum hc/e^2 and the magnetic flux quantum $h/2e$ (h is Plank's constant, c is the speed of light in vacuum and e is the elementary charge). Another phenomenon is the absorptivity of 2D systems solely defined by the fine structure constant $\alpha = e^2/\hbar c$ which is associated with quantum electrodynamics rather than material science.[52] Below, we explain this unique phenomenon for graphene, a semi-metal 2D system, and InAs quantum wells.

2.3.1 Absorptivity of graphene

Optical properties of the extremely thin films with vertical quantum confinement are best described in terms of their optical conductivity G. It has been predicted that the high frequency optical conductivity for Dirac fermions in graphene has the universal value of: [68–70]

$$G= e^2/4\hbar = 6.08 \times 10^{-5}\ \Omega^{-1} \qquad \text{(Eq. 2.3)}$$

The optical transmittance and reflectance of a free standing monolayer of graphene are[71]:

$$T = (1+2\pi G/C)^{-2} \text{ and } R = 0.25\pi^2\alpha^2 T \qquad \text{(Eq. 2.4)}$$

This yields the following absorptivity of graphene:

$$A = (1\text{-}T\text{-}R) \approx \pi\alpha = 0.023 \qquad \text{(Eq. 2.5)}$$

Nair *et al.* studied experimentally the absorptivity of single and multiple suspended layers of graphene. They prepared graphene crystals in a way that they cover a sub-millimeter aperture in a metal scaffold, as can be seen in Figure 2.4a, inset. An optical microscope image of one of the apertures containing a monolayer and a bilayer of suspended graphene in transmitted white light is shown in Figure 2.4a. The line scan across the image depicts the change in the light intensity. The measurement shows that the absorptivity is 2.3 ± 0.1 % for a single layer of graphene, independent of the wavelength (Figure 2.4b). Furthermore,

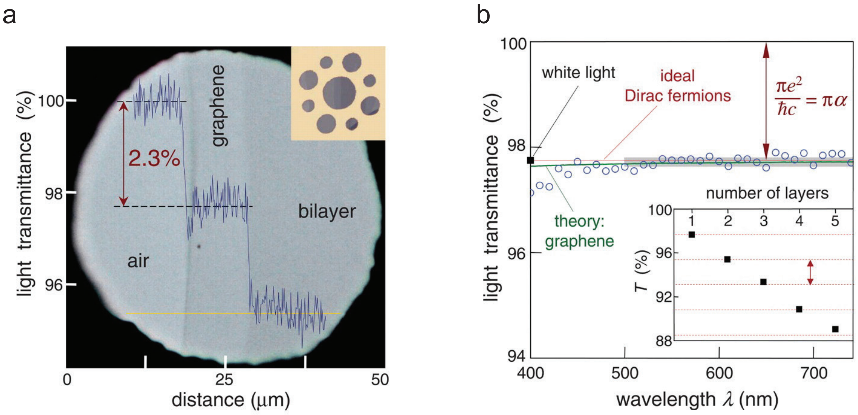

Figure 2.4. Absorptivity of graphene crystals. (a) Optical microscope image of an aperture covered partially with a monolayer and bilayer of suspended graphene in transmitted white light. The line scan across the image depicts the changes in the light intensity. The inset shows a sample holder with several apertures in a metal scaffold. (b) Transmittance spectrum of a single layer of graphene crystal (open circles). The red line shows the transmittance for two-dimensional Dirac fermions. The absorptivity of 2.3 ± 0.1 % for a single layer is observed, independent of the wavelength of the light. The inset shows the transmittance as a function of the number of stacked graphene layers. Each graphene layer adds another 2.3 % to the absorptivity. Reproduced with permission from ref (52).

the absorptivity is proportional to the number of stacked graphene layers: each graphene layer adds another 2.3 % to the total absorptivity (Figure 2.4b inset).

2.3.2 Absorptivity of InAs quantum wells

Fang *et.al.* studied InAs quantum wells (called quantum membranes in the paper) present on a substrate as a 2D semiconductor model system.[53] Figure 2.5a shows the optical microscope image of a periodic array of InAs stripes, 3 nm in thickness, on a CaF_2 substrate being optically transparent in the wavelength range of interest. The ultrathin InAs quantum wells can be recognized by their optical contrast. The absorptivity spectra of the InAs layers with thickness of 3 nm, 6 nm, 9 nm, 14 nm and 19 nm are illustrated in Figure 2.5b. For each thickness, step-like features with step heights of 1.6 ± 0.2 % are observed in the absorptivity spectra, each step indicates a novel optical transition. Remarkably, the absorptivity is independent of the thickness of the quantum wells, as long as there is quantum confinement in the thin direction. The observed steps are actually smaller than $\pi\alpha = 2.3\%$, as observed for a monolayer of graphene. This is due to the reduced local optical electric field at the quantum well mounted on a substrate with a refractive index n. The quantum well experiences both the incident electric field E_0 and the Fresnel reflected electric field $E_0(1-n)/(1+n)$. Therefore, the local optical electric field gets weaker by $2E_0/(1+n)$ and as a result the optical absorption is reduced by $(2/(1+n))^2$:

$$A = \pi\alpha\,(2/(1+n))^2 \qquad \text{(Eq. 2.6)}$$

The refractive index of CaF_2 used as substrate is 1.43, reducing the absorptivity of a single quantum well from 2.3 % to 1.58 %, in close agreement with the experimental results.

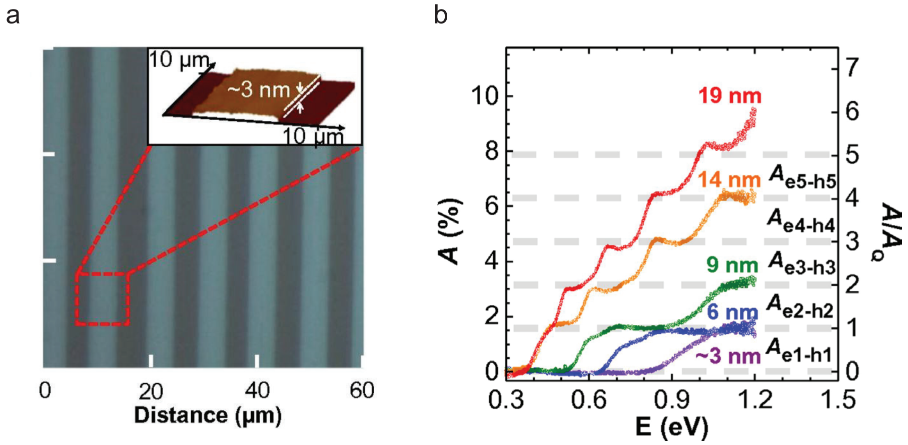

Figure 2.5. Absorptivity of InAs quantum wells. (a) Optical microscope image of InAs stripes with thickness of 3 nm on CaF_2 substrate. The inset shows an Atomic Force Microscope image of a single stripe. (b) Absorptivity spectra of a series of InAs quantum wells, with thickness of 3 nm, 6 nm, 9 nm, 14 nm and 19 nm, showing universal absorptivity steps of 1.6 %. Reproduced with permission from ref (53).

2.4 Electrochemical gating in a three-electrode electrochemical cell

Electrochemistry is a branch of physical chemistry dealing with the interaction between electrical energy and chemical change. Here, we use a transistor-type device based on the classic three-electrode electrochemical cell. The superlattices that we make are not electronically doped. By incorporating the superlattice as a working electrode in such a three-electrode electrochemical cell, electrons (occupying the conduction bands) or holes (occupying the valence bands) can be injected in a controlled way, the countercharge being provided by ions from the contacting electrolyte; this is called electrochemical gating, or electrolyte gating. Hence, such a three-electrode electrochemical cell provides a powerful tool to control the number of charge carriers (the position of the Fermi level) in a superlattice, and to study its transport properties and band occupation. This section describes the general principles of electrochemical gating and provides experimental details.

2.4.1 Principle of electrochemistry

A three-electrode electrochemical cell consists of a working electrode (the electrode of interest), a counter electrode (CE) and a reference electrode (RE). The potential of the working electrode (WE) is measured with respect to a RE made up of phases with constant composition. No current flows through the RE, ensuring it has a constant makeup with a constant potential. Therefore, changing the potential difference between the working and reference electrode only changes the potential (*i.e.* the electrochemical potential or the Fermi level) of the working electrode. The potential of the working electrode is changed by polarizing it against a counter electrode. Thus, the electrochemical current flows in the working electrode - counter electrode circuit, while the potential of the working electrode is measured independently versus a reference electrode. The capacitance of the CE is much larger than that of the WE. This is ensured by using a metal with a high DOS at the Fermi level and additionally by ensuring a large enough surface area. A scheme of a three-electrode electrochemical cell with an electrolyte, WE, RE and CE is depicted in Figure 2.6a.

At a given potential, either positive or negative charges accumulate on the surface of the solid phase (working electrode) and form a thin layer of charge carriers. Oppositely charged ions in the liquid phase (electrolyte) will be attracted to the surface charges due to the Coulomb force, electrically screening the first layer of charges on the electrode surface (Figure 2.6b). The whole array of the charge species at the solid-liquid interface is called the electrical double layer (EDL).[72]

Since the charge in the working electrode (the superlattice) is electronic and the countercharge consists of ions, charges cannot cross the interface when the potential across it is altered. Hence, the behavior of the working electrode-electrolyte interface is similar to that of a capacitor. Therefore, the electrode-electrolyte interface can be described by a series connection of two capacitors with capacitances of C_{solid} and C_{dl}:[73]

$$1/C = 1/C_{solid} + 1/C_{dl} \qquad \text{(Eq. 2.7)}$$

However, unlike the parallel-plate capacitors that have a capacitance independent of

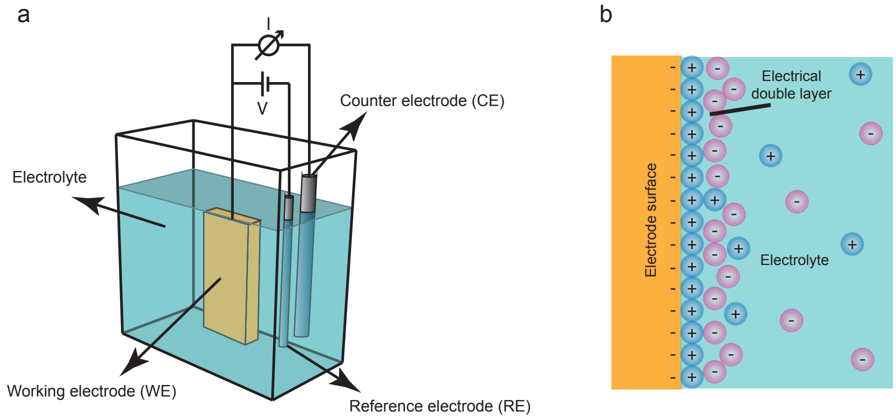

Figure 2.6. schematic diagram of a three-electrode electrochemical cell and an electrical double layer. (a) Typical three-electrode electrochemical cell with a working electrode (WE) a reference electrode (RE) and a counter electrode (CE). (b) Schematic of electrical double layer in an electrolyte at contact with a negatively-charged electrode.

potential, the C is often a function of potential.

The potential drop over the interfacial part of the electrode is given by:

$$(\partial \Delta V_{solid)} / \partial V = C_{dl} / (C_{dl} + C_{solid}) \qquad \text{(Eq. 2.8)}$$

For the case in which $C_{solid} >> C_{dl}$, *e. g.* a metal electrode, $(\partial \Delta V_{solid}) / \partial V = C_{dl} / C_{solid} << 1$, a change of the electrode potential leads mainly to a change of the potential drop across the double layer. This means that the charge carrier concentration in the electrode remains unchanged.

If the solid phase is a semiconductor with a low intrinsic electron concentration, $C_{solid} << C_{dl}$, so $(\partial \Delta V_{solid}) / \partial V = C_{dl} / C_{dl} \approx 1$. By increasing the electrochemical potential, the Fermi level in the interfacial layer rises which means that the electron concentration in the interfacial layer strongly increases. Hence, it is possible to change the carrier concentration from almost zero (insulator) to high values (conductor) by electrochemical polarization. The excess of the charge carriers leads to a strong increase in the conductivity of the material, therefore the method is called electrochemical or electrolyte gating. Electrochemical gating has been used by several research groups to study the electrical properties of diverse semiconductor materials since the first study of carrier injection into an n-type semiconductor of $MoSe_2$ in 1982 by Gerischer and co-workers.[74]

2.4.2 Design of an electrochemically gated transistor

We use two different transistor-type designs for the electrochemical gating measurements described in this thesis. They are both based on gold patterns deposited on a $Si\text{-}SiO_2$ wafer by optical or e-beam lithography. First, for the differential capacitance and conductance measurements on superlattices (which will be explained in the following section), the working electrode on itself is made of two interdigitated gold-pattern electrodes (source and drain) separated by a gap (Figure 2.7a). On a given substrate, several transistors with different length and width of the gaps are present, in order to be able to provide varying "sensitivity" in the experiments.

Second, we also measure *in-situ* the changes in the band-to-band optical absorption emerging from electron occupation of the conduction band (absorption quenching). The appropriate device for this is shown in Figure 2.7b; the design is characterized by a large grating of gold electrodes on top of a thin layer of Al, which is topped by an Al_2O_3 layer to be electrically isolated from the gold-electrode system. The Al layer results in good reflectivity of the light, enabling us to perform precise absorption quenching measurements in reflectivity mode.

The superlattice is incorporated in the transistor as follows: the surface of the device makes contact with the prepared superlattice that floats on the ethylene glycol, the superlattice adheres to the substrate surface, and then the device is retracted upwards.

2.4.3 Differential capacitance and conductance measurements

To quantify the charge injection into the superlattices, differential capacitance measurements are performed by changing the Fermi-level of the superlattice and measuring the charging

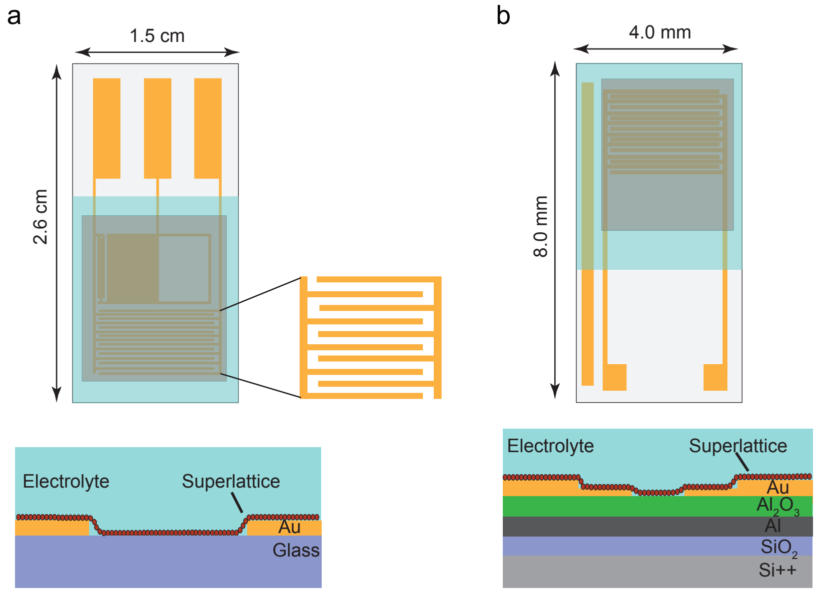

Figure 2.7. Electrode designs in electrochemical gating measurements. (a) For differential capacitance and conductance measurements, the working electrode consists of two interdigitated gold fingers with a gap of varying length and width. (b) The design for optical bleach measurement is characterized by a large grating of gold electrodes on top of an Al layer. The Al layer results in good reflectivity of the light. In such a way, absorption measurements can be performed in reflectivity mode, under conditions of electrochemical gating.

current. This is done by sequentially changing the potential of the working electrode in small steps (25 to 50 mV) as depicted in Figure 2.8a, and monitoring the transient charging current (between the working electrode and the counter electrode) in an interval time of 2 to 5s. The initial peak current decays quickly (in about 1s) to a constant current attributed to a background current. This background current is subtracted to obtain the charging current of the superlattice. The integrated current provides the total injected charge, and thus the number of charge carriers introduced into the superlattice after each potential step (Figure 2.8b). To obtain the differential capacitance of the superlattice (in C/V), the charge carrier is divided by the potential step:

$$C(V) = \Delta Q/\Delta V \tag{Eq. 2.9}$$

Figure 2.8c shows the differential capacitance as a function of the electrochemical potential of the working electrode for electron injection into a PbSe square superlattice in the forward (blue) and backward scan (red) as an example. Negative of the onset, electrons are injected into the superlattice. The symmetry in the C versus V graph can give the information about the chemical stability of the system. If C versus V is symmetric, the system is electrochemically stable: the charges inserted can be also extracted. On the other hand, asymmetry in the C versus V curve indicates the loss of charge carriers by (undesired) irreversible electrochemical processes, *i.e.* reduction of impurities in the

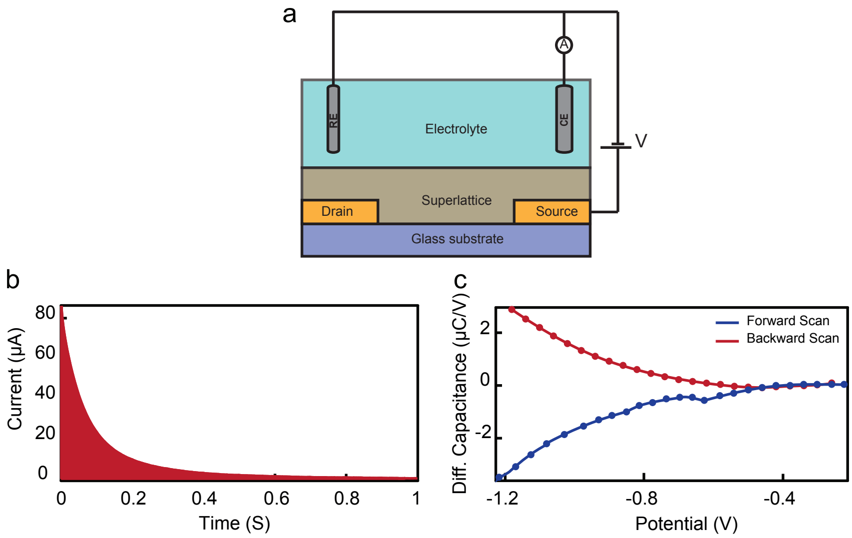

Figure 2.8. Differential capacitance measurement. (a) Differential capacitance measurements are performed by applying a small step in the potential of the (source-drain) working electrode and monitoring the transient charging current. (b) The initial peak current decays quickly (in about 1s) to a constant background. This background current is subtracted to obtain the charging current into the superlattice. The integrated charging current provides the number of charge carriers introduced into the superlattices after each potential step. (c) The differential capacitance of the superlattice, which is obtained by division of the charging current by the potential step, displayed as a function of the potential of the working electrode in the forward and backward scan.

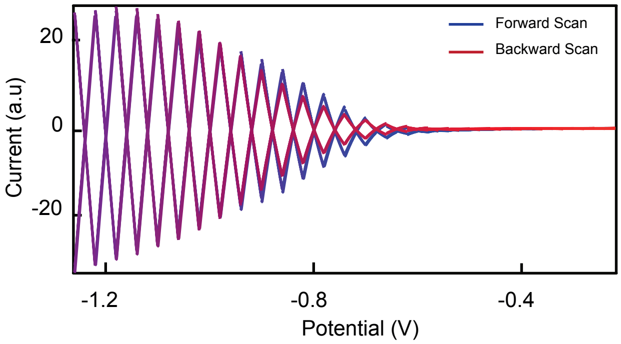

Figure 2.9. Measurement of the conductance of the superlattice. A small potential difference is applied between the source and drain of the working electrode and the ohmic response is measured. The figure displays this current response as a function of the overall potential of the working electrode.

electrolyte solution or in the superlattice itself.
It is possible to estimate the number of NCs in the gated area of the electrode from the number of NCs presented in an HAADF-STEM image and the total area of the superlattice. This allows us to calculate the average number of charge carriers per NC as a function of the electrochemical potential. Alternatively, the number of charge carriers per NC that occupy the conduction band can be extracted from the quenching of the inter-band absorption upon electrochemical gating. This method will be described in Section 2.4.4.

In order to investigate the conductivity of the superlattices, a working electrode is used that consist of the interdigitated source-drain gold fingers. The potential of the source finger is varied around the fixed potential of the drain and the source-drain current is measured (Figure 2.9). These measurements are performed in each potential step of the differential capacitance measurements after the equilibrium is reached. The relation between the source-drain current and source-drain potential difference is Ohmic, and directly provides the conductance of the superlattice (at given position of the Fermi level). From this conductance and the geometry of the interdigitated gap, the conductivity of the superlattice can be obtained:

$$\sigma = (G.w)/(l.h) \qquad \text{(Eq. 2.10)}$$

G is the conductance, w and l are the width and length of the fingers and h is the thickness of the superlattice.

From the charge per NC and the conductivity, the mobility of the superlattice can be calculated:

$$\mu = (\sigma .V)/(e.N) \qquad \text{(Eq. 2.11)}$$

e is elementary charge, N charge per NC and V is the volume of the NC.

2.4.4 Optical absorption bleach measurements

Optical absorption spectroscopy that measures the quenching of the valence-to-conduction band optical transition is a precise way to directly monitor the conduction band occupation of a superlattice at a given position of the Fermi level. For this purpose, the sample is illuminated by white light. After passing through the electrolyte and the superlattice, the light reflected by the Al layer is collected (Figure 2.10a). While changing the potential of source-drain working electrode in small steps, the absorption spectrum after each potential step is taken. As soon as electrons (holes) occupy the conduction band (valence band), a negative change in the superlattice light absorption is observed reflecting the occupation of the delocalized orbitals by injected electrons (holes). The quenching of the absorption, referenced to the maximum quenching, provides the orbital occupation factor in a quantitative way.

The number of charges injected into a superlattice energy level can be determined from: [63,75,76]

$$\langle n_i(V)\rangle = g_i \int_0^{\infty} \frac{A_i(V) - A_i(V_{oc})}{A_i(V_{oc})} dE \qquad \text{(Eq. 2.12)}$$

with $<n_i(V)>$ the average number of electrons per NC in level i at an electrochemical

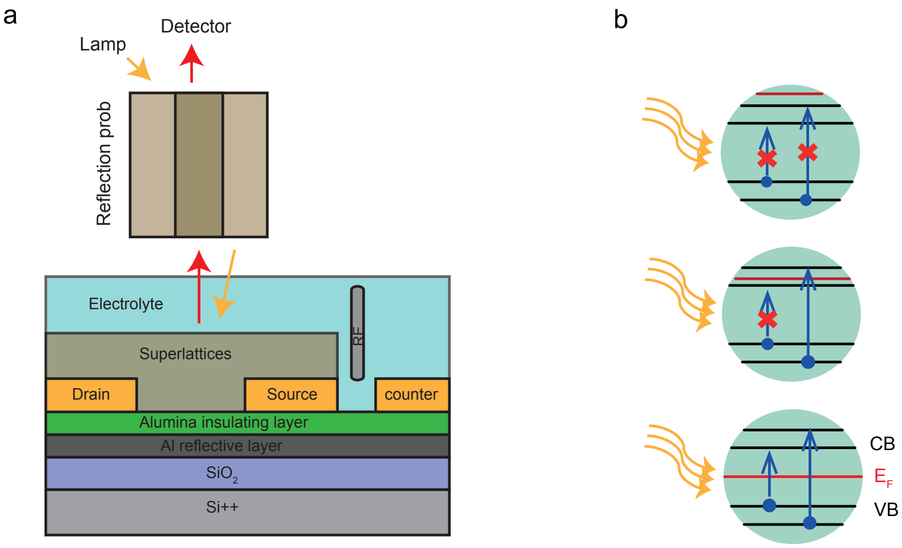

Figure 2.10. Schematic of optical bleach measurement. (a) The sample is illuminated by white light via an optical reflection probe. After passing through the electrolyte and the superlattice, the light reflected by the Al layer is collected. While changing the potential of the source - drain working electrode in small steps, the absorption quenching can be measured as a function of the Fermi-level in the superlattice. (b) Schematic of the electron injection process: raising the Fermi level of the superlattice from within the band gap to above the lowest conduction band results in band occupation. This blocks valence-to-conduction band transitions, *i.e.* quenching of the light absorption.

potential of V, g_i the degeneracy of the energy level i, $A_i(V)$ the absorption from the all transitions to level i and $A_i(V_{oc})$ the open circuit potential. This method assumes negligible structural reorganization upon charge injection as well as a negligible effect of the injected charges on the bandgap energy and oscillator strength of the band edge transition. These assumptions are usually found to be justified.[63,77]

References

1. Rossetti, R. & Brus, L. Electron-hole recombination emission as a probe of surface chemistry in aqueous cadmium sulfide colloids. *J. Phys. Chem.* **86**, 4470–4472 (1982).
2. De Mello Donegá, C. Synthesis and properties of colloidal heteronanocrystals. *Chem. Soc. Rev.* **40**, 1512–1546 (2011).
3. Roduner, E. Size matters: Why nanomaterials are different. *Chem. Soc. Rev.* **35**, 583–592 (2006).
4. Bae, W. K. *et al.* Highly effective surface passivation of PbSe quantum dots through reaction with molecular chlorine Highly effective surface passivation of PbSe quantum dots through reaction with molecular chlorine. *J. Am. Chem. Soc.* **134**, 20160–20168 (2012).
5. Ning, Z. *et al.* All-inorganic colloidal quantum dot photovoltaics employing solution-phase halide passivation. *Adv. Mater.* **24**, 6295–6299 (2012).
6. Tang, J. *et al.* Colloidal-quantum-dot photovoltaics using atomic-ligand passivation. *Nat. Mater.* **10**, 765–771 (2011).
7. Chaves, R. *et al.* Colloidal Nanocrystals with Molecular Metal Chalcogenide Surface Ligands. *Science* **324**, 1417–1420 (2009).
8. Tangirala, R., Baker, J. L., Alivisatos, A. & Milliron, D. J. Modular inorganic nanocomposites by conversion of nanocrystal superlattices. *Angew. Chemie - Int. Ed.* **49**, 2878–2882 (2010).
9. Kovalenko, M. V., Bodnarchuk, M. I., Zaumseil, J., Lee, J. S. & Talapin, D. V. Expanding the chemical versatility of colloidal nanocrystals capped with molecular metal chalcogenide ligands. *J. Am. Chem. Soc.* **132**, 10085–10092 (2010).
10. Nag, A. *et al.* Metal-free inorganic ligands for colloidal nanocrystals: S^{2-}, HS^-, Se^{2-}, HSe^-, Te^{2-}, HTe^-, TeS_3^{2-}, OH^-, and NH_2^- as surface ligands. *J. Am. Chem. Soc.* **133**, 10612–10620 (2011).
11. Evers, W. H. *et al.* Low-dimensional semiconductor superlattices formed by geometric control over nanocrystal attachment. *Nano Lett.* **13**, 2317–2323 (2013).
12. Boneschanscher, M. P. *et al.* Long-range orientation and atomic attachment of nanocrystals in 2D honeycomb superlattices. *Science* , **344**, 1377–1380 (2014).
13. Kalesaki, E., Evers, W. H., Allan, G., Vanmaekelbergh, D. & Delerue, C. Electronic structure of atomically coherent square semiconductor superlattices with dimensionality below two. *Phys. Rev. B.* **88**, 1–9 (2013).
14. Delerue, C. & Vanmaekelbergh, D. Electronic band structure of zinc blende CdSe and rock salt PbSe semiconductors with silicene-type honeycomb geometry. *2D Mater.* **2**, 34008 (2015).
15. Kalesaki, E. *et al.* Dirac cones, topological edge states, and nontrivial flat bands in two-dimensional semiconductors with a honeycomb nanogeometry. *Phys. Rev. X*

4, 1–12 (2014).

16. Murray, C. B., Kagan, C. R. & Bawendi, M. G. Self-Organization of CdSe Nanocrystallites into Three-Dimensional Quantum Dot Superlattices. *Science* **270**, 1335-1338 (1995).
17. Eldridge, M. D., Madden, P. A. & Frenkel, D. Entropy-driven formation of a superlattice in a hard-sphere binary mixture. *Nature* **365**, 35–37 (1993).
18. Bodnarchuk, M. I., Kovalenko, M. V., Heiss, W. & Talapin, D. V. Energetic and entropic contributions to self-assembly of binary nanocrystal superlattices: Temperature as the structure-directing factor. *J. Am. Chem. Soc.* **132**, 11967–11977 (2010).
19. Shevchenko, E. V. *et al.* Organization of Matter on Different Size Scales : Monodisperse Nanocrystals and Their Superstructures Organization of Matter on Different Size Scales : Monodisperse Nanocrystals and Their Superstructures. *Adv. Funct. Mater.* **12**, 653–664 (2002).
20. Evers, W. H. *et al.* Entropy-driven formation of binary semiconductor-nanocrystal superlattices. *Nano Lett.* **10**, 4235–4241 (2010).
21. Rupich, S. M., Shevchenko, E. V., Bodnarchuk, M. I., Lee, B. & Talapin, D. V. Size-dependent multiple twinning in nanocrystal superlattices. *J. Am. Chem. Soc.* **132**, 289–296 (2010).
22. Lowman, G. M., Nelson, S. L., Graves, S. M., Strouse, G. F. & Buratto, S. K. Polyelectrolyte-Quantum Dot Multilayer Films Fabricated by Combined Layer-by-Layer Assembly and Langmuir-Schaefer Deposition. *Langmuir* **20**, 2057–2059 (2004).
23. Jiang, C., Markutsya, S. & Tsukruk, V. V. Collective and individual plasmon resonances in nanoparticle films obtained by spin-assisted layer-by-layer assembly. *Langmuir* **20**, 882–890 (2004).
24. Dabbousi, B. O., Murray, C. B., Rubner, M. F. & Bawendi, M. G. Langmuir-Blodgett Manipulation of Size-Selected CdSe Nanocrystallites. *Chem. Mater.* **6**, 216–219 (1994).
25. Tian, Y. & Fendler, J. H. Langmuir-Blodgett film formation from fluorescence-activated, surfactant-capped, size-selected CdS nanoparticles spread on water surfaces. *Chem. Mater.* **8**, 969–974 (1996).
26. Iakovenko, B. S. A. *et al.* One- and Two-Dimensional Arrays of Magnetic Nanoparticles by the Langmuir - Blodgett Technique. *Adv. Mater.* **11**, 388–392 (1999).
27. Achermann, M., Petruska, M. A., Crooker, S. A. & Klimov, V. I. Picosecond Energy Transfer in Quantum Dot Langmuir - Blodgett Nanoassemblies. *J. Phys. Chem. B* **107**, 13782–13787 (2003).
28. Sastry, M., Gole, A. & Patil, V. Lamellar Langmuir-Blodgett films of hydrophobized colloidal gold nanoparticles by organization at the air-water interface. *Thin Solid Films* **384**, 125–131 (2001).
29. Henrichs, S., Collier, C. P., Saykally, R. J., Shen, Y. R. & Heath, J. R. The dielectric function of silver nanoparticle Langmuir monolayers compressed through the metal insulator transition. *J. Am. Chem. Soc.* **122**, 4077–4083 (2000).
30. Pichler, S. *et al.* Evaluation of ordering in single-component and binary nanocrystal superlattices by analysis of their autocorrelation functions. *ACS*

Nano **5**, 1703–1712 (2011).

31. Redl, F. X., Cho, K. S., Murray, C. B. & O'Brien, S. Three-dimensional binary superlattices of magnetic nanocrystals and semiconductor quantum dots. *Nature* **423**, 968–971 (2003).
32. Shevchenko, E. V., Talapin, D. V., Kotov, N. A., O'Brien, S. & Murray, C. B. Structural diversity in binary nanoparticle superlattices. *Nature* **439**, 55–59 (2006).
33. Chen, Z., Moore, J., Radtke, G., Sirringhaus, H. & O'Brien, S. Binary nanoparticle superlattices in the semiconductor-semiconductor system: CdTe and CdSe. *J. Am. Chem. Soc.* **129**, 15702–15709 (2007).
34. Talapin, D. V. *et al.* Quasicrystalline order in self-assembled binary nanoparticle superlattices. *Nature* **461**, 964–967 (2009).
35. Evers, W. H., Friedrich, H., Filion, L., Dijkstra, M. & Vanmaekelbergh, D. Observation of a ternary nanocrystal superlattice and its structural characterization by electron tomography. *Angew. Chem. Int. Ed.* **48**, 9655–9657 (2009).
36. Friedrich, H. *et al.* Quantitative Structural Analysis of Binary Nanocrystal Superlattices by Electron Tomography. *Nano. Lett.* **9**, 2719–2724 (2009).
37. Kiely, C. J., Fink, J., Brust, M., Bethell, D. & Schiffrin, D. J. Spontaneous ordering of bimodal ensembles of nanoscopic gold clusters. *Nature* **396**, 444–446 (1998).
38. Puntes, V. F., Gorostiza, P., Aruguete, D. M., Bastus, N. G. & Alivisatos, A. P. Collective behaviour in two-dimensional cobalt nanoparticle assemblies observed by magnetic force microscopy. *Nat. Mater.* **3**, 263–268 (2004).
39. Connolly, S., Fullam, S., Korgel, B. & Fitzmaurice, D. Time-resolved small-angle X-ray scattering studies of nanocrystal superlattice self-assembly. *J. Am. Chem. Soc.* **120**, 2969–2970 (1998).
40. Bigioni, T. P. *et al.* Kinetically driven self assembly of highly ordered nanoparticle monolayers. *Nat. Mater.* **5**, 265–270 (2006).
41. Dong, A., Chen, J., Vora, P. M., Kikkawa, J. M. & Murray, C. B. Binary nanocrystal superlattice membranes self-assembled at the liquid-air interface. *Nature* **466**, 474–477 (2010).
42. Chen, J. *et al.* Collective dipolar interactions in self-assembled magnetic binary nanocrystal superlattice membranes. *Nano Lett.* **10**, 5103–5108 (2010).
43. Narayanan, S., Wang, J. & Lin, X. M. Dynamical self-assembly of nanocrystal superlattices during colloidal droplet evaporation by *in situ* small angle X-ray scattering. *Phys. Rev. Lett.* **93**, 1–4 (2004).
44. Geuchies, J. J. *et al. In situ* study of the formation mechanism of two-dimensional superlattices from PbSe nanocrystals. *Nat. Mater.* **15**, 1248–1254 (2016).
45. Van der Stam, W. *et al.* Self-assembly of colloidal hexagonal bipyramid- and bifrustum-shaped ZnS nanocrystals into two-dimensional superstructures. *Nano Lett.* **14**, 1032–1037 (2014).
46. Peters, J. L. *et al.* Mono- and Multilayer Silicene-Type Honeycomb Lattices by Oriented Attachment of PbSe Nanocrystals: Synthesis, Structural Characterization, and Analysis of the Disorder. *Chem. Mater.* **30**, 4831–4837 (2018).
47. Van Overbeek, C. *et al.* Interfacial Self-Assembly and Oriented Attachment in the Family of PbX (X = S, Se, Te) Nanocrystals. *J. Phys. Chem. C* **122**, 12464–12473

(2018).

48. Whitham, K., Smilgies, D. M. & Hanrath, T. Entropic, Enthalpic, and Kinetic Aspects of Interfacial Nanocrystal Superlattice Assembly and Attachment. *Chem. Mater.* **30**, 54–63 (2018).
49. Luther, J. M., Zheng, H., Sadtler, B. & Alivisatos, A. P. Synthesis of PbS nanorods and other ionic nanocrystals of complex morphology by sequential cation exchange reactions. *J. Am. Chem. Soc.* **131**, 16851–16857 (2009).
50. Beberwyck, B. J., Surendranath, Y. & Alivisatos, A. P. Cation exchange: A versatile tool for nanomaterials synthesis. *J. Phys. Chem. C* **117**, 19759–19770 (2013).
51. Sohlberg, K., Pennycook, T. J., Zhou, W. & Pennycook, S. J. Insights into the physical chemistry of materials from advances in HAADF-STEM. *Phys. Chem. Chem. Phys.* **17**, 3982–4006 (2015).
52. Nair, R. R. *et al.* Fine Structure Constant Defines Visual Transperency of Graphene. *Science* **320**, 1308 (2008).
53. Fang, H. *et al.* Quantum of optical absorption in two-dimensional semiconductors. *Proc. Natl. Acad. Sci.* **110**, 11688–11691 (2013).
54. Shim, M. & Guyot-sionnest, P. N-type collidal semiconductor nanocrystals. *Nature* **407**, 981–983 (2000).
55. Boehme, S. C., Vanmaekelbergh, D., Evers, W. H., Siebbeles, L. D. A. & Houtepen, A. J. *In Situ* Spectroelectrochemical Determination of Energy Levels and Energy Level Offsets in Quantum-Dot Heterojunctions. *J. Phys. Chem. C* **120**, 5164–5173 (2016).
56. Wang, C. Electrochromic Nanocrystal Quantum Dots. *Science* **291**, 2390–2392 (2001).
57. Jha, P. P. & Guyot-Sionnest, P. Trion decay in colloidal quantum dots. *ACS Nano* **3**, 1011–1015 (2009).
58. Galland, C. *et al.* Two types of luminescence blinking revealed by spectroelectrochemistry of single quantum dots. *Nature* **479**, 203–207 (2011).
59. Jha, P. P. & Guyot-Sionnest, P. Electrochemical switching of the photoluminescence of single quantum dots. *J. Phys. Chem. C* **114**, 21138–21141 (2010).
60. Boehme, S. C. *et al.* Density of trap states and Auger-mediated electron trapping in CdTe quantum-dot solids. *Nano Lett.* **15**, 3056–3066 (2015).
61. Boehme, S. C. *et al.* Electrochemical control over photoinduced electron transfer and trapping in CdSe-CdTe quantum-dot solids. *ACS Nano* **8**, 7067–7077 (2014).
62. Wu, Y. K. *et al.* n-Type Conducting CdSe Nanocrystal Solids. *Science* **300,** 1277–1280 (2003).
63. Houtepen, A. J., Kockmann, D. & Vanmaekelbergh, D. Reappraisal of variable-range hopping in quantum dot solids. *Nano Lett.* **8**, 3516 (2008).
64. Liu, H., Pourret, A. & Guyot-sionnest, P. Mott and Efros-Shklovskii Variable Films. *ACS Nano* **4**, 5211–5216 (2010).
65. Kaindl, R. A., Hägele, D., Carnahan, M. A. & Chemla, D. S. Transient terahertz spectroscopy of excitons and unbound carriers in quasi-two-dimensional electron-hole gases. *Phys. Rev. B* **79**, 1–13 (2009).
66. Ambigapathy, R. *et al.* Coulomb correlation and band gap renormalization at high carrier densities in quantum wires. *Phys. Rev. Lett.* **78**, 3579–3582 (1997).
67. Hangleiter, A. *et al.* Efficient formation of excitons in a dense electron-hole

plasma at room temperature. *Phys. Rev. B* **92**, 1–5 (2015).

68. Ando, T., Zheng, Y. & Suzuura, H. Dynamical Conductivity and Zero-Mode Anomaly in Honeycomb Lattices. *J. Phys. Soc. Japan* **71**, 1318–1324 (2002).
69. Falkovsky, L. A. & Varlamov, A. A. Space-time dispersion of graphene conductivity. *Eur. Phys. J. B* **56**, 281–284 (2007).
70. Gusynin, V. P., Sharapov, S. G. & Carbotte, J. P. Unusual microwave response of dirac quasiparticles in graphene. *Phys. Rev. Lett.* **96**, 1–4 (2006).
71. Kuzmenko, A. B., van Heumen, E., Carbone, F. & van der Marel, D. Universal optical conductance of graphite. *Phys. Rev. Lett.* **100**, 1–5 (2008).
72. Bard, A. J. & Faulkner, L. R. Electrochemical methods fundamentals and applications. *Molecular Biology* **8**, (2015).
73. Vanmaekelbergh, D., Houtepen, A. J. & Kelly, J. J. Electrochemical gating: A method to tune and monitor the (opto)electronic properties of functional materials. *Electrochim. Acta* **53**, 1140–1149 (2007).
74. Jaeger, C. D., Gerischer, H. & Kautek, W. Formation of an Inversion Layer in n-Type $MoSe_2$ Electrodes: Observation in the Presence of Highly Oxidizing Redox Systems. *Berichte der Bunsengesellschaft für Phys. Chemie* **86**, 20–25 (1982).
75. Boehme, S. C., Wang, H., Siebbeles, L. D. A., Vanmaekelbergh, D. & Houtepen, A. J. Electrochemical charging of CdSe quantum dot films: Dependence on void size and counterion proximity. *ACS Nano* **7**, 2500–2508 (2013).
76. Houtepen, A. J. & Vanmaekelbergh, D. Orbital occupation in electron-charged CdSe quantum-dot solids. *J. Phys. Chem. B* **109**, 19634–19642 (2005).
77. Wang, C., Wehrenberg, B. L., Woo, C. Y. & Guyot-Sionnest, P. Light emission and amplification in charged CdSe quantum dots. *J. Phys. Chem. B* **108**, 9027–9031 (2004).

Chapter 3

Investigation of the band structure of PbSe and CdSe nanocrystal superlattices with light absorption and photoconductivity spectroscopy

Abstract

2D lead-chalcogenide and cadmium-chalcogenide superlattices composed of nanocrystals (NCs), one NC monolayer in thickness, present outstanding opto-electronic properties due to their unique band structure. The honeycomb structure, with its similarity to graphene and silicene, theoretically results in a semiconductor with Dirac-type valence and conduction bands with massless holes and electrons. Here, we report on the optical absorption properties of such PbSe and CdSe superlattices. The absorption features associated with transitions between the S-type valence and conduction bands show significant broadening due to the several types of structural disorder. Interestingly, the absorptivity of a monolayer superlattice is about 1.6 ± 0.1 %, independent of the material (CdSe or PbSe) and geometry (square or honeycomb). One additional layer of superlattice adds another 1.6 % to the absorptivity. This value of the absorptivity appears to be universal in 2D systems including III-V quantum wells and graphene, as reported before. We show that the honeycomb superlattice of PbSe nanocrystals can be incorporated as a NC monolayer in a photodetector device. The responsivity spectrum closely reproduces the same features of the absorption spectrum of the PbSe honeycomb superlattices, but shows a better signal to noise ratio, as it counts electrons (instead of photons). The photoconductivity spectrum measured at cryogenic temperatures might become an appropriate method to study in more detail the band structure of 2D semiconductors.

3.1 Introduction

Two dimensional (2D) semiconductors have been extensively investigated during the last decade for their unique opto-electronic properties.[1–8] Lately, the interest in 2D systems has experienced a considerable rise, owing to the emergence of graphene[9] and topological insulators.[10,11] One of the remarkable optical properties of such 2D systems is the universal value of light absorptivity by these materials. A single layer of graphene is found to absorb a significant amount of light, $\pi\alpha = 2.3$ % ($\alpha = e^2/\hbar c$ being the fine structure constant), related to its two dimensional nature.[12] It has also been shown experimentally and theoretically that light absorption in 2D semiconductors is independent of specific material parameters, such as the band gap, effective mass, and thickness. Fang *et al.* indicated that the magnitude of the light absorption in InAs quantum membranes (QMs) is an integer product of a "quantum of absorptance", *i.e.* $\pi\alpha/nc = 1.6$ %, where α is a fine structure constant and nc is the optical local field correction factor.[13] Such strong absorption is a promising feature for the use of 2D semiconductors in optoelectronic devices, *e.g.* photovoltaic cells and photodetectors. Therefore, further experimental investigation on other 2D semiconductors is of great fundamental and applied interest.

Here, we focus on the optical absorption properties of 2D PbSe and CdSe NC superlattices, one NC monolayer in thickness, which have been prepared by interfacial nanocrystal assembly and attachment.[14–16] These 2D networks have a square or honeycomb nanogeometry; the nanocrystals are epitaxially connected in the lateral directions *via* their {100} facets, and thus strongly electronically coupled. Theoretical studies have shown that the nanostructuring can result in interesting band structures different from that of a quantum well.[17] It has been calculated that two-dimensional NC superstructures with a honeycomb geometry show Dirac-type valence and conduction bands, separated by the semiconductor band gap, thus combining valuable semiconductor properties with those of graphene.[18]

We demonstrate that the magnitude of the light absorption by a single nanostructured sheet of PbSe and CdSe present on quartz has a specified value of 1.6 ± 0.1 %, regardless of the superlattice geometry. Our measurements on a double NC layer of PbSe square and honeycomb superlattices show that the addition of one more layer adds another 1.6 % to the absorptivity. Furthermore, since the responsivity of a photodetector should reflect the absorption features of the active absorber in the device, we performed photoconductivity (PC) measurements on a PbSe honeycomb superlattice. We show that a honeycomb sheet of PbSe, one NC monolayer in thickness, can be incorporated in a photodetector device. The responsivity spectrum closely reproduces the same features of the absorption spectrum of the PbSe honeycomb superlattices, however with a better signal-to-noise ratio.

3.2 Light absorption by a superlattice consisting of a monolayer of unattached PbSe NCs

A superlattice, consisting of a monolayer of unattached PbSe NCs, is formed following the self-assembly method depicted in Figure 3.1a. We use an immiscible liquid, ethylene glycol (EG), as substrate. At first, we add 8 μl of 0.01 M oleic acid in EG to the liquid substrate (6.5 ml) to suppress attachment of the NCs. This additional oleic acid not only

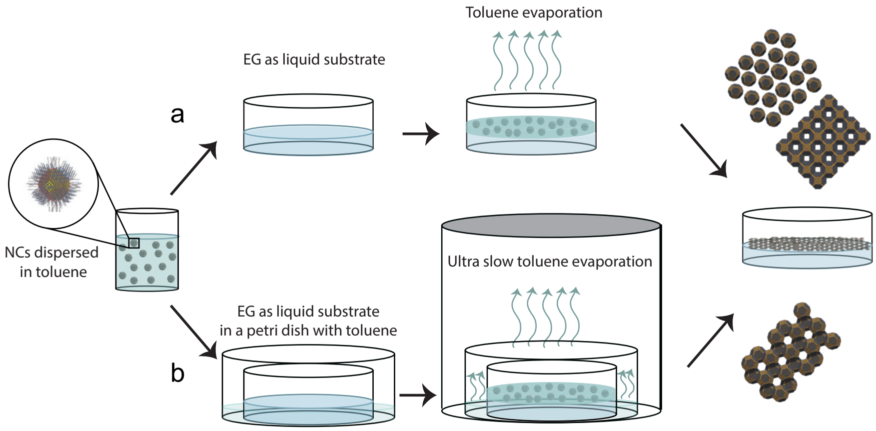

Figure 3.1. Schematic representation of the experimental setup for self-assembly and oriented attachment of PbSe NCs. A dispersion of PbSe NCs in toluene is prepared. (a) The NCs dispersion is drop casted on top of the EG substrate, after which the toluene evaporates in about an hour. The PbSe square superlattices are formed by assembling PbSe NCs at the toluene/air interface after which the NCs attach *via* their four vertical {100} facets. To form a self-assembled monolayer of NCs without attachment a certain amount of oleic acid diluted in EG is added to the EG substrate prior to the NCs drop casting. This additional oleic acid prevents oriented attachment of NCs and increases the wettability of the toluene droplet (with the NCs) on EG. (b) To form honeycomb superlattices, the EG substrate is put inside another petri dish containing extra toluene. After drop casting the dispersion of PbSe NCs on top of the EG, a beaker was placed on top of the petri dishes to slow down the toluene evaporation. After about 16 hours honeycomb superlattices are formed.

prevents oriented attachment of NCs[14] but also increases the wettability of the toluene droplet (with the NCs) on EG. Then, a dispersion of PbSe NCs (with the size of 6.15 ± 0.4 nm) in toluene was drop casted on top of the substrate. After about an hour, the solvent was evaporated and the NCs are self-assembled on the liquid-air interface.

A part of the large scale monolayer sheet is shown in Figure 3.2a. The zoomed-in TEM image in the right inset shows the hexagonal ordering of the NCs. We remark that such hexagonal ordering has also been observed before for a PbS self-assembled monolayer prepared by spreading a PbS QD dispersion on a Langmuir trough.[19] Choi *et al.* showed that the self-assembly of the NCs depends strongly on the shape and surface energies of the NCs.[20] It has been shown that for PbSe NCs with $Pb(oleate)_2$ ligands, ligand chemisorption and surface reconfiguration leads to a transformation of the nanocrystal shape from a truncated nanocube with rather rough surface facets to a truncated octahedron with larger and smoother {111} facets.[21] In addition, Soligno *et al.* demonstrated that the adsorption of cube-like NCs at a liquid-liquid interface is thermodynamically favorable, and induces a capillary deformation of the solvent surface forcing the NCs into a hexagonal geometry.[22] The electron diffraction (ED) pattern in the left is exceptional as it shows that the nanocrystals are also atomically aligned in plane, as well as perpendicular to the plane. This NC alignment without bonding is very remarkable, but beyond the scope of the present work.

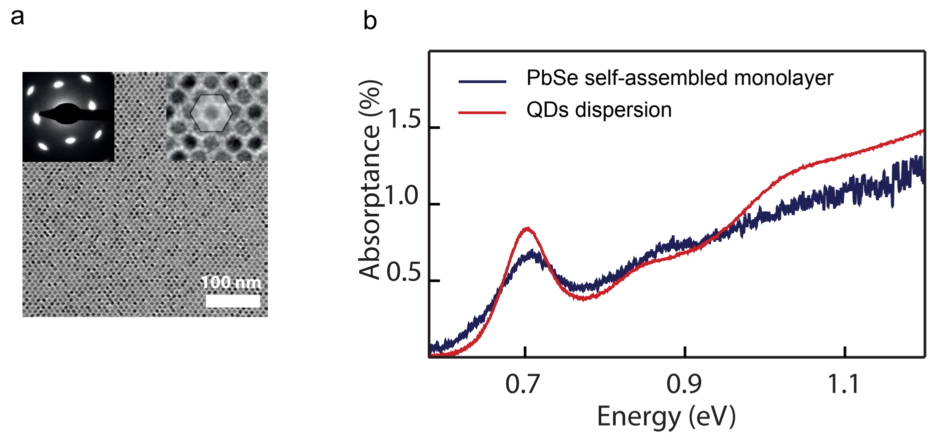

Figure 3.2. TEM image and absorption spectrum of a self-assembled monolayer of PbSe NCs. (a) TEM image of a part of a PbSe monolayer sheet prepared by self-assembly. Right inset: Zoomed-in TEM image showing the individual quantum dots in a hexagonal ordering. Left inset: Electron diffraction pattern showing the high degree of hexagonal ordering in the monolayer, with atomic alignment of the nanocrystals in plane and perpendicular to the plane. (b) Absorption spectrum of a self-assembled monolayer of PbSe NCs. The red curve shows the absorption of PbSe QDs suspended in tetrachloroethylene as a reference.

The absorption spectrum of such a single NC monolayer deposited on a quartz substrate is depicted in Figure 3.2b. The first excitonic peak related to the S_eS_h transition is slightly blue-shifted compared to that of the NCs in dispersion. Besides this, the first and also the higher-energy peaks in the absorption spectrum of the monolayer are slightly broadened; this may be due to a dipolar or weak electronic coupling between the NCs. This monolayer of PbSe NCs has an absorptivity of 0.7 %, thus considerably smaller than $\pi\alpha/nc = 1.6$ % (see above and below). Measurement on several samples of monolayers of NCs separated from each other by the capping (as in Figure 3.2a) resulted in an averaged absorptivity of 0.7 ± 0.1 % (Figure A3.1 presents two examples).

It is interesting to calculate the absorption enhancement of this close packed monolayer of NCs. For this purpose, we can define a thickness-independent absorption coefficient α as:[23]

$$\alpha = \frac{4\pi k}{\lambda}, \lambda = \frac{hc}{E} \qquad \text{(Eq. 3.1)}$$

λ is the wavelength of the incident light, and k is the wavelength-dependent imaginary part of refractive index ñ = n+ik.

The absorption coefficient μ for a dispersion of QDs is:

$$\mu = \frac{n}{n_s}|f_{LF}|^2 f\alpha = \frac{n}{n_s}|f_{LF}|^2\, f\,\frac{4\pi k}{\lambda} \qquad \text{(Eq. 3.2a)}$$

$$|f_{LF}|^2 = \frac{9n_s^4}{(n^2 - k^2 + 2n_s^2)^2 + 4(nk)^2} \qquad \text{(Eq. 3.2a)}$$

n_s is the refractive index of the solvent, n is the wavelength-dependent real part of the refractive index (of the particle) and f is the volume fraction of the particles. f_{LF} denotes a local field correction that accounts for the difference in dielectric polarizability between the particles and the dielectric medium.

Since μ increases proportionally to f, we can define an intrinsic absorption coefficient μ_i as:[23]

$$\mu_i = \frac{\mu}{f} = \frac{n}{n_s} |f_{LF}|^2 \frac{4\pi k}{\lambda} \qquad \text{(Eq. 3.3)}$$

Therefore the absorption cross section σ of a single QD will be:

$$\sigma = \mu_i V_{QD} = \frac{n}{n_s} |f_{LF}|^2 \frac{4\pi k}{\lambda} \left(\frac{\pi d^3}{6}\right) \qquad \text{(Eq. 3.4)}$$

And the molar extinction coefficient ε:

$$\varepsilon = \frac{N_A \sigma}{\ln(10)} \qquad \text{(Eq. 3.5)}$$

According to Beer–Lambert law, the absorbance of the QDs is:

$$A = \varepsilon c L \qquad \text{(Eq. 3.6)}$$

where L is the thickness of the sample (the path length) and c is the molar concentration of the particles. The molar concentration of the PbSe monolayer sample is equal to 7.03×10^{-13} molcm^{-2} (see for details A3.2).

At energies far above the band edge, the QDs can be considered as bulk material.[23–25] At energy of 1.2 eV, we considered n and k equal to 5.24 and 0.916, respectively.[26] We considered n_s = 1.46 for quartz on which the monolayer is stamped. However, this value might be slightly higher due to some effective medium refractive index determined by the QDs, quartz, ligands and vacuum. The calculated absorbance with the above parameters is equal to 3.62×10^{-4} (at 1.2 eV). The measurement absorbance for the sample is equal to 1.39×10^{-3}. This means that we have 3.85 absorption enhancement for a self-assembled monolayer of PbSe monolayer above the band edge. Geiregat *et al.* also demonstrated 4 and 5 times absorption enhancement for self-assembled CdSe and PbS QDs, respectively, at energies above the band edge.[19]

For the absorbance in the band edge, we considered $\varepsilon_{(gap,eV)}$ as:[25]

$$\varepsilon_{gap,eV} = 3.1\, d^{0.9}\ (\text{cm}^{-1}\mu\text{M}^{-1}\text{meV}) \qquad \text{(Eq. 3.7)}$$

Therefore, the integrated absorbance of the first half of the excitonic peak calculated from this formula is equal to 0.56×10^{-2}. From the absorbtion measurement, the integrated absorbance of the first half of the excitonic peak is equal to 1.44×10^{-1}, which means that we have 25 times absorption enhancement in the band edge. However, this value is much higher than the values reported by Geiregat *et al.* for self-assembled CdSe and PbS QDs.[19]

3.3 Light absorption by PbSe square and honeycomb superlattices, one NC monolayer thick

PbSe square superlattices were prepared by drop casting of a PbSe QDs (with a diameter of 5.8 ± 0.4 nm) dispersion in toluene on the EG substrate (Figure 3.1a). The system is left for 45 minutes at 25 °C. The toluene evaporates and the PbSe square superlattices are formed by assembling PbSe NCs at the toluene/air interface after which the NCs attach *via* their four vertical {100} facets. Heating the system at 55 °C for 20 minutes leads to the formation of a square structure network with stronger atomic connections between the NCs.

Honeycomb superlattices were obtained by an ultra-slow oriented attachment procedure illustrated in Figure 3.1b.[16] A small petri dish was filled with EG as a liquid substrate and placed in a bigger petri dish that contained toluene. A dispersion of PbSe NC in toluene was drop casted on the EG. A beaker was placed on top of the petri dishes to slow down the toluene evaporation. Under these conditions, the evaporation of the toluene solvent and the superlattice formation took around 16 hours. An atomically coherent buckled silicene-type honeycomb structure is formed by epitaxial attachment of the PbSe NCs *via* three of their 6 {100} facets.

A part of the square and honeycomb structures is shown in Figure 3.3a and b. The HAADF-STEM images of the lattices (in the right insets) show the atomic connection of nanocrystals *via* their {100}-type facets. The ED patterns (in the left insets) reveal that the structures have a high degree of crystallinity, as observed with the occurrence of four and six sharp spots in ED patterns recorded on a selected area for the square and honeycomb structures, respectively.

The absorption spectra of a single and double layer of the both superlattices are presented in Figure 3.3c and d. It can be seen that the absorption peaks show a red shift and broadening compared to PbSe NCs in suspension, due to the quantum mechanical coupling between the NCs in the superlattice.[27] For a better view of the first absorption feature of the monolayer superlattices, zoomed-in graphs in the energy range of 0.5 to 0.9 eV are presented in the insets.

Figure 3.3e and f show the band structure obtained from a tight-binding (TB) calculation for both square and honeycomb superlattices. The TB parameters are those for PbSe, taken from ref.[28] (for more details see A3.3). There is clear mirror symmetry between the conduction and the valence bands similar to the symmetry of the bands in bulk PbSe.[28,29] There is a manifold of four bands (eight bands including the spins) in the lowest conduction band.[17] In the silicene-type honeycomb lattices, the lower manifold of the 8 conduction bands is derived from the 1S state and the higher bands are composed of 1P states.[30] The first feature in the absorption is due to a transition from the multitude of higher valence bands to the lower conduction bands over the entire Brillouin zone. It is clear that the calculated energy of the gap corresponds reasonably well with that of the first absorption feature. We remark that many-body interactions (e, h) are not taken into account in the theory.

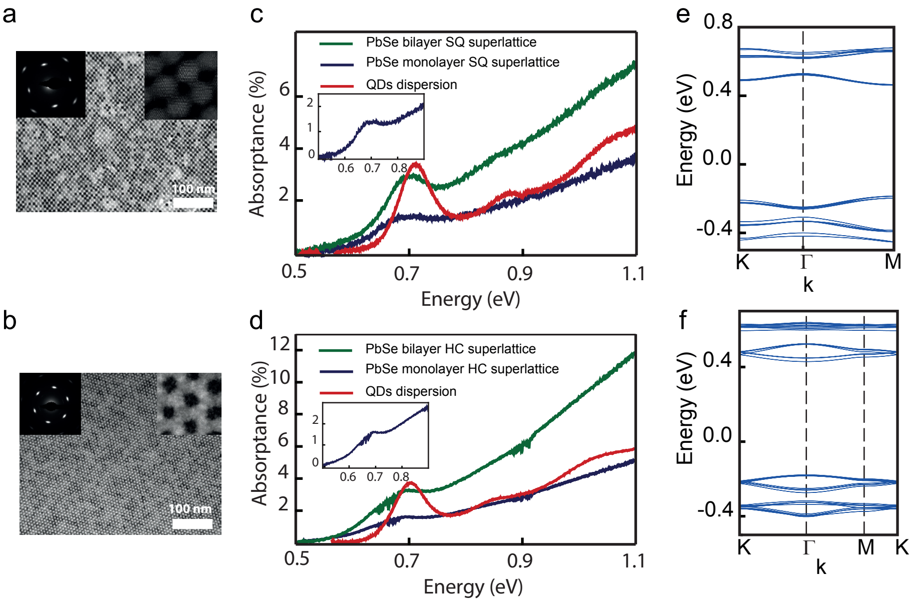

Figure 3.3. TEM analysis, absorption spectra and band structure of PbSe square and honeycomb superlattices. (a, b) TEM images of a part of a PbSe square and honeycomb lattices (monolayer) prepared by self-assembly and oriented attachment. Right inset: HAADF-STEM images of the superlattices showing the connection of the NCs by their {100}-type facets. Left inset: Electron diffraction patterns (ED) showing that the structures have a high degree of crystallinity, as observed with the occurrence of sharp spots in ED patterns recorded on a selected area. (c, d) Absorption spectra of a mono and double layer of PbSe superlattices. The first excitonic absorption features show a red shift and broadening, compared to the NCs in suspension (red curve). For the superlattices, a NC monolayer in thickness on a quartz substrate, the absorption is 1.5 % at photon energy of 0.69 eV. The addition of one more layer adds another 1.5 % to the light absorptance. (e, f) Tight-binding (TB) band structure for a square superlattice. The nanocrystals are modeled as spheres with a diameter of 5.5 nm connected by cylinders of 2.2 nm in length. The bands below zero energy are valence bands, the conduction bands are above zero energy.

The absorptivity of both the square and honeycomb monolayers is about 1.5 % of the incident light at the S_eS_h transition energies. The value observed here is actually smaller than the $\pi\alpha = 2.3$ % observed for a suspended monolayer of graphene.[12] It was reported by Fang *et al.* that the absorptance of InAs quantum membranes (QMs) reduced by the factor of $(2/(1+n))^2$, known as local optical electric field correction factor, when the quantum membrane film was mounted on a substrate of refractive index n.[13] We measured the absorption of the superlattices on a quartz substrate with the refractive index of 1.46. Therefore, the absorptance of the superlattice, theoretically, should be equal to 1.52 % which is in good agreement with our experimental results. We have measured several samples; the averaged value for the absorptance was 1.6 ± 0.1 % for a single NC layer of PbSe superlattice. The absorption measurement on a stacking of two layers of PbSe superlattice, placed on top of each other, showed 3.2 ± 0.1 % absorptivity for both square and honeycomb geometries (see Figure 3.3c and d); hence, the addition of one more layer adds another 1.5 % to the absorptivity. The noise observed in the absorption spectra is related to the experimental conditions and the apparatus.

3.4 Light absorption by CdSe superlattices

We transformed PbSe square and honeycomb lattices into CdSe *via* a $Cd^{2+}$for Pb^{2+} cation exchange reaction.[31,32] The SiN TEM grids and quartz substrates with superlattices on top were kept in a 0.1 M cadmium oleate solution for 1h at 150 °C and then 175 °C for 10 minutes. Afterwards, we cleaned the samples by immersing them in toluene, butanol/methanol (1:1) and methanol, respectively. We performed Energy Dispersive X-ray (EDX) Spectroscopy to confirm the complete transformation of PbSe superstructure to CdSe, as shown in Figure A3.2.

3.4.1 Light absorption by a CdSe square superlattice

Since the atomic structure of the CdSe superstructure (zinc blend) is different from PbSe (rock salt), we expect a different band structure for CdSe superlattices compared to the PbSe. We have performed tight-binding (TB) calculations of the band structure for CdSe square superlattices, shown in Figure 3.4a. In the calculations, we considered the NCs as spheres with the size of 6.1 nm attached by cylinders with the length of 2.5 nm. The valence bands show a complicated energy dispersion due to the presence of coupled heavy-hole and light-hole bands.[33] The lowest conduction band is two-fold degenerate including the spins. The next three bands consist of dispersive and flat bands.

In Figure 3.4b the calculated absorption spectrum of a CdSe square superstructure is presented; it consists of four main transitions from valence bands to S-type, dispersive P-type, flat P-type and higher energy states of the conduction band. S_eS_h and P_eP_h transitions appear at 2.03 and 2.25 eV, respectively. The third feature at higher energy mainly consists of transitions to the S-type and P-type flat bands. We should mention

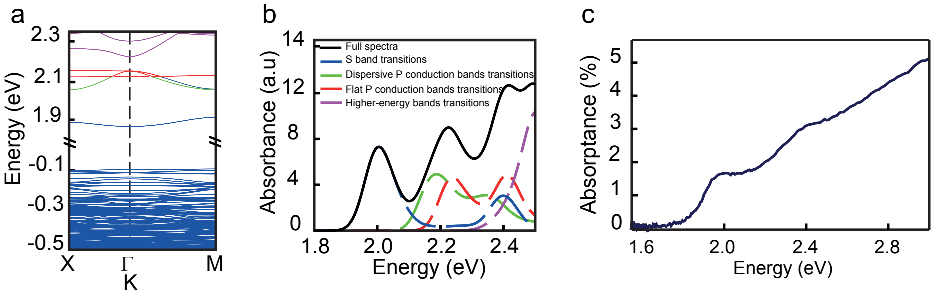

Figure 3.4. Band structure and absorption spectra of a CdSe square superlattice. (a) TB calculations of highest valence and lowest conduction bands for a 2D CdSe superlattice with square geometry. The lowest conduction band is two-fold degenerate including the spins. The next three bands consist of dispersive and flat bands. (b) The calculated absorption spectrum of a square superstructure consists of four main transitions from valence bands to S-type, dispersive P-type, flat P-type and higher energy states of the conduction band. (c) Absorption spectrum of a monolayer of CdSe square superlattice. The first feature is related to the S_eS_h transitions. The second feature consists of the transitions to the P-type bands. The absorptivity of this monolayer is also about 1.65 % of the incident light at the S_eS_h transitions energies. We remark that the experimental features are more step-shaped than peak-like, unlike the predictions by single-particle tight binding theory.

here that this calculation does not account for excitonic effects; we expect that the (e, h) binding energy is about 50-100 meV.[2]

The absorption spectrum of a single layer of CdSe square superlattice (with the original PbSe size of 5.8 ± 0.4 nm) is presented in Figure 3.4c. The first exciton feature related to the S_eS_h transition is observed at 1.97 eV which is in a good agreement with the TB calculation. The second feature at higher energy of 2.38 eV can be related to transitions to dispersive or flat P-type bands, as predicted in the TB calculations. The absorptivity of this monolayer is also about 1.65 % of the incident light at the S_eS_h transition. This is an agreement with the previous measurements on the PbSe superlattices and with the results of other 2D systems present on a quartz substrate.

3.4.1 Light absorption by a CdSe honeycomb superlattice

We performed TB calculations for the band structure of CdSe silicene-type honeycomb superlattices shown in Figure 3.5a. The two lowest conduction bands form a Dirac cone at K-points. The next bands consist of a flat band and a second Dirac cone, due to coupling and interference of the in-plane P_x, P_y orbitals.[18] The two highest valence bands form a Dirac Cone, with a non-trivial band opening at the K-points. The calculated absorption spectrum is shown in figures 3.5b and c for different values of artificial broadening. The optical transitions between the valence and conduction Dirac cones may result in a double-peak absorption feature (Figure 3.5b). However, the slightest disorder, or simply the temperature broadening may cloud this; this is shown in figure 3.5c, where a broadening of 35 meV is assumed.

The experimental absorption spectrum in Figure 3.5d shows a very broad feature (peak) at 1.96 eV. This peak can be attributed to the S-type valence to S-type conduction band transitions. The single NC layer of CdSe honeycomb superlattice absorbs 1.65 % of the light at the energy of the first absorption feature (Figure 3.5d); in agreement with the results obtained with the PbSe and CdSe square superlattices.

The broad peak without any sign of the predicted Dirac features (Fig. 3.5b) indicates, in our opinion, that several origins of broadening must be present. Tentative explanations are: the small bandwidth of the S-type conduction band (≈ 40 meV) compared to the temperature broadening, broadening effects due to several types of structural disorder, and possibly (e, h) Coulomb effects. Therefore, applying cryogenic techniques to investigate the absorption spectrum of the honeycomb superlattices seems to be essential. One of the techniques which can be used to study the band structure of the honeycomb superlattices is photoconductivity. In the next section, we present our first photoconductivity measurements on PbSe honeycomb superlattice.

3.5 Photoconductivity measurements with a PbSe honeycomb superlattice

Photoconductivity is defined as increase in the conductivity of a material resulting from the absorption of photons. A variety of experimental techniques based on photoconductivity have been developed. We performed a simple photoconductivity experiment using a constant monochromatic light source for excitation of the sample. The light intensity was

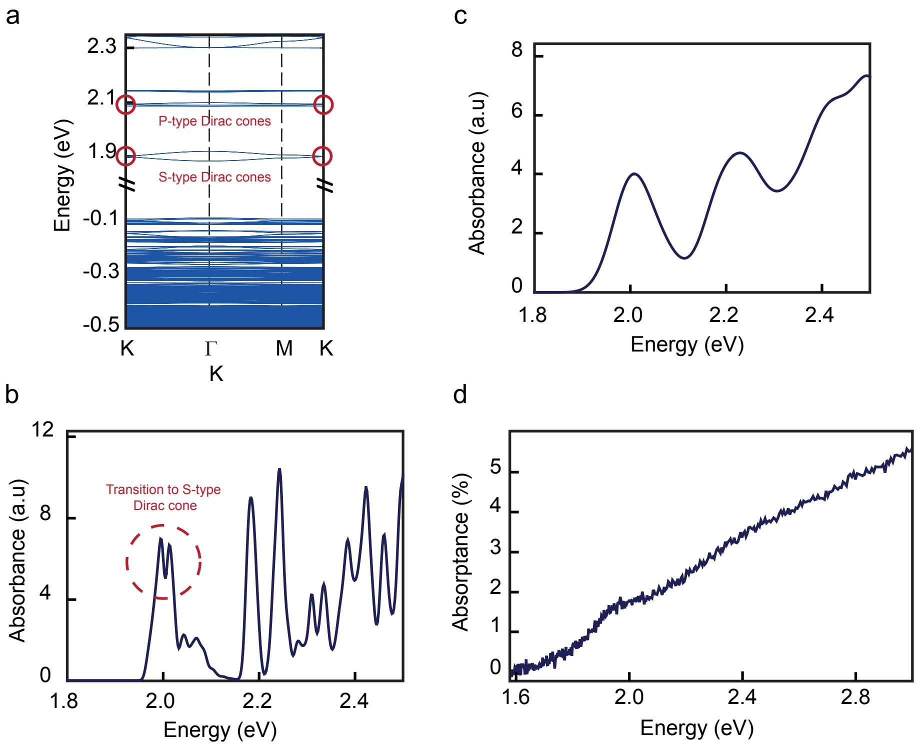

Figure 3.5. Band structure and calculated and experimental absorption spectra of a CdSe honeycomb superlattice. (a) TB calculations of the highest valence and lowest conduction bands for a 2D CdSe silicene-type honeycomb superlattice. The two lowest conduction bands form a Dirac Cone at the K-points. The next bands consist of a flat band and a second Dirac cone. The two highest valence bands form a Dirac cone, with a non-trivial band opening at the K-points. (b) The TB absorption spectrum of a CdSe honeycomb superlattice with the line broadening of 5 meV. The S_eS_h transition peak splits in two small narrow peaks due to the vanishing density of states at the K-points. (c) The TB absorption spectrum of a CdSe honeycomb superlattice with the line broadening of 35 meV showing the same features as CdSe square superlattice. (d) Experimental absorption spectrum of a monolayer of CdSe honeycomb superlattice. This single layer of CdSe honeycomb superlattice absorbs 1.65 % of the white light. Special features due to the transitions between two Dirac cones cannot be observed.

modulated by a mechanical chopper within a frequency range from 2 to 120 Hz, and the resulting modulated photocurrent across the sample was measured, with a device described below. The basic experimental arrangement is illustrated in Figure 3.6a. The PbSe honeycomb superlattices were stamped onto the interdigitated electrodes on the glass substrate (with 34 cm electrodes length and 25 µm gap between the electrodes). All the measurements and device characterization were conducted with the sample being loaded in an air-tight cell, prepared inside the glovebox to avoid oxidation of the sample.

The inset of Figure 3.6b presents the I-V curves in the dark and under illumination. The dark conductivity is 65×10^{-6} S/cm and it increases by an order of magnitude under illumination. The responsivity is defined as the ratio between the photocurrent and the power of incident radiation (photon flux) for each wavelength (energy). In the simplest model, the responsivity spectrum should be equal to the light absorption spectrum. We see that the responsivity spectrum in Figure 3.6b, measured at a frequency modulation of 10 Hz, closely reproduces the features of the absorption spectrum observed for the PbSe honeycomb sample. In addition to the first excitonic peak related to the S_eS_h transition, we can also observe the P_eP_h transition peak at higher energy, and even the signature of a third transition. We performed photoconductivity measurements on several other PbSe honeycomb samples and observed the same features in the responsivity curves.

Comparison of the responsivity (red line) and absorption (blue line) spectra in Figure 3.6b shows that the signal-to-noise in the responsivity spectra is considerably better than in the absorption spectra. This might allow us to observe more details of the band structure, once the photoconductivity measurements can be performed at cryogenic temperatures.

3.6 Conclusion and outlook

We studied the absorption properties of PbSe and CdSe superlattices with square and honeycomb geometries. The absorption peaks associated with transitions between the S-type envelope functions show significant broadening due to the quantum mechanical coupling between the NCs in the superlattice. We observed that a monolayer of superlattice, regardless of material and geometry, absorbs 1.6 ± 0.1 % of incident white light. The origin of this value lies in the two dimensionality nature of the superstructure.[12,13] We showed that one additional layer of superlattice adds another 1.6 % to the absorptance of PbSe superlattices, demonstrating that there is little interaction between the layers and the absorption is simply the sum of the absorption two 2D layers.

We have successfully incorporated a monolayer of PbSe honeycomb superlattices in a photodetector device. The spectral responsivity reproduces the features of the absorption

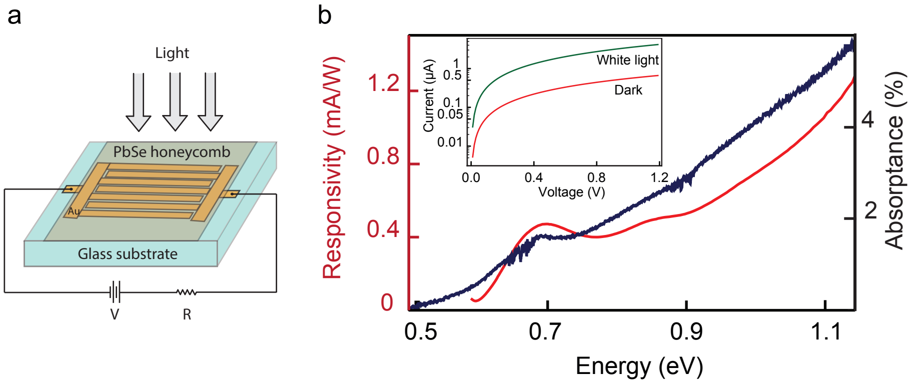

Figure 3.6. Photoconductivity measurements on PbSe honeycomb superlattices. (a) A sketch of experimental arrangement for photoconductivity measurement on honeycomb superlattice. (b) Responsivity spectrum for a NC monolayer PbSe honeycomb superlattice (red line) reproducing the same features of the absorption spectrum (blue line) but with more detail. The inset shows the I-V characteristics of the same sample.

spectrum observed for the PbSe honeycomb superlattices, but with a better signal to noise ratio, persuading us to use photoconductivity techniques to investigate the band structure of the honeycomb superlattices.

3.7 Methods

PbSe nanocrystal synthesis

PbSe QDs were synthesized based on the methodology of Steckel *et al.* method.[34] For the lead precursor, a mixture of 4.77 g lead acetate (99.99 %, Sigma-Aldrich), 10.35 g oleic acid (90 %, Sigma-Aldrich) and 39.75 g 1-octadecene (90 %, Sigma-Aldrich) was heated at 120°C under vacuum for 5 hours. For the selenium precursor, a mixture of 3.52 g selenium powder (99.99 %, Alfa Aesar), 46.59 mL trioctylphosphine (90 %, Sigma-Aldrich) and 0.41 mL diphenylphospine (98 %, Sigma-Aldrich) were prepared by dissolving selenium. Subsequently, 10.25 mL of the lead containing solution was heated upto 180 °C and 7.5 mL of the selenium precursor was injected. The mixture was kept at 150°C for 70 second and the NC growth was quenched with 30 mL of a methanol/butanol mixture (1:2). The NC product solution was centrifuged and the NCs were dissolved in toluene. This concentrated suspension of PbSe nanocrystals was washed twice more with methanol and the NCs were dissolved in toluene.

PbSe double layer superlattices

To prepare double layer of PbSe superlattices, we stamped the first monolayer of superlattices on the quartz substrates from ethylene glycol. We dried the samples under vacuum for an hour and stamped the second layer of the superlattices on top of the first layer and dried again under vacuum.

Electron microscopy and electron diffraction

Electron micrographs and selected area electron diffraction were recorded on a FEI Technai 20 operated at 200 kV. The HAADF-STEM measurements were performed using a double aberration corrected FEI TITAN operated at 300 kV.

Optical absorption characterization

For the optical absorption measurements, the superlattices on the quartz substrates were loaded in a custom-made sample holder inside an oxygen and water free glovebox. Optical absorption spectra of QDs in toluene dispersion and 2D superlattices of CdSe networks were obtained with a PerkinElmer Lambda 950 spectrometer. The absorption measurement of the unattached PbSe NCs and 2D PbSe superlattices were performed on a Bruker Vertex FT VIS-IR spectrometer.

Photoconductivity characterization

Photoconductivity measurements were performed by illumination with a halogen lamp, monochromatized by a SP-2150i Acton monochromator using a grating with 600 groves/mm and a blaze wavelength of 1µm. A silicon filter was placed directly after the monochromator exit. The light was modulated by a mechanical chopper within a frequency range from 1 to 500 Hz placed at the entry to the monochromator. The voltage applied across the sample was supplied by a Keithley 2614B. Spectral photoconductivity experiments were controlled by a home-written software in LabView. IV characteristics were measured using the Keithley 2614B SMU with and without illumination via a white light LED and controlled by a home-written software in Python.

References

1. Schliehe, C. *et al.* Ultrathin PbS sheets by two-dimensional oriented attachment. *Science* **329**, 550–553 (2010).
2. Ithurria, S. *et al.* Colloidal nanoplatelets with two-dimensional electronic structure. *Nat. Mater.* **10**, 936–941 (2011).
3. Rao, C. N. R., Ramakrishna Matte, H. S. S. & Maitra, U. Graphene analogues of inorganic layered materials. *Angew. Chem. Int. Ed.* **52**, 13162–13185 (2013).
4. Wang, Q. H., Kalantar-Zadeh, K., Kis, A., Coleman, J. N. & Strano, M. S. Electronics and optoelectronics of two-dimensional transition metal dichalcogenides. *Nat.*

Nanotechnol. **7**, 699–712 (2012).
5. Van der Stam, W. *et al.* Solution-processable ultrathin size- and shape-controlled colloidal $Cu_{2-x}S$ nanosheets. *Chem. Mater.* **27**, 283–291 (2015).
6. Novoselov, K. S. *et al.* A roadmap for graphene. *Nature* **490**, 192–200 (2012).
7. Du, Y. *et al.* A general method for the large-scale synthesis of uniform ultrathin metal sulphide nanocrystals. *Nat. Commun.* **3**, 1177 (2012).
8. Berends, A. C. & de Mello Donega, C. Ultrathin One- and Two-Dimensional Colloidal Semiconductor Nanocrystals: Pushing Quantum Confinement to the Limit. *J. Phys. Chem. Lett.* **8**, 4077–4090 (2017).
9. Novoselov, K. S. *et al.* Electric Field Effect in Atomically Thin Carbon Films. *Science* **306**, 666–669 (2004).
10. Yan, B. & Zhang, S. C. Topological materials. *Reports Prog. Phys.* **75**, (2012).
11. Hasan, M. Z. & Kane, C. L. Colloquium: Topological insulators. *Rev. Mod. Phys.* **82**, 3045–3067 (2010).
12. Nair, R. R. *et al.* Fine Structure Constant Defines Visual Transperency of Graphene. *Science* **320**, 1308 (2008).
13. Fang, H. *et al.* Quantum of optical absorption in two-dimensional semiconductors. *Proc. Natl. Acad. Sci.* **110**, 11688–11691 (2013).
14. Evers, W. H. *et al.* Low-dimensional semiconductor superlattices formed by geometric control over nanocrystal attachment. *Nano Lett.* **13**, 2317–2323 (2013).
15. Boneschanscher, M. P. *et al.* Long-range orientation and atomic attachment of nanocrystals in 2D honeycomb superlattices. *Science* **344**, 1377–1380 (2014).
16. Peters, J. L. *et al.* Mono- and Multilayer Silicene-Type Honeycomb Lattices by Oriented Attachment of PbSe Nanocrystals: Synthesis, Structural Characterization, and Analysis of the Disorder. *Chem. Mater.* **30**, 4831–4837 (2018).
17. Kalesaki, E., Evers, W. H., Allan, G., Vanmaekelbergh, D. & Delerue, C. Electronic structure of atomically coherent square semiconductor superlattices with dimensionality below two. *Phys. Rev. B.* **88**, 1–9 (2013).
18. Kalesaki, E. *et al.* Dirac cones, topological edge states, and nontrivial flat bands in two-dimensional semiconductors with a honeycomb nanogeometry. *Phys. Rev. X* **4**, 1–12 (2014).
19. Geiregat, P., Justo, Y., Abe, S., Flamee, S. & Hens, Z. Giant and Broad-Band Absorption Enhancement in Colloidal Quantum Dot Monolayers through Dipolar Coupling. *ACS Nano* **7**, 987–993 (2013).
20. Choi, J. J., Bian, K., Baumgardner, W. J., Smilgies, D. M. & Hanrath, T. Interface-induced nucleation, orientational alignment and symmetry transformations in nanocube superlattices. *Nano Lett.* **12**, 4791–4798 (2012).
21. Peters, J. L. *et al.* Ligand-Induced Shape Transformation of PbSe Nanocrystals. *Chem. Mater.* **29**, 4122–4128 (2017).
22. Soligno, G., Dijkstra, M. & van Roij, R. Self-Assembly of Cubes into 2D Hexagonal and Honeycomb Lattices by Hexapolar Capillary Interactions. *Phys. Rev. Lett.* **116**, 1–6 (2016).
23. Hens, Z. & Moreels, I. Light absorption by colloidal semiconductor quantum dots. *J. Mater. Chem.* **22**, 10406–10415 (2012).
24. Jasieniak, J., Smith, L., van Embden, J., Mulvaney, P. & Califano, M. Re-examination of the size-dependent absorption properties of CdSe quantum dots. *J. Phys. Chem.*

C **113**, 19468–19474 (2009).

25. Moreels, I. *et al.* Composition and Size-Dependent Extinction Coefficient of Colloidal PbSe Quantum Dots. *Chem. Mater.* **19**, 6101–6106 (2007).
26. Suzuki, N., Sawai, K., and Adachi, S. Optical properties of PbSe. *J. Appl. Phys.* **77**, 1249–1255 (1955).
27. Sandeep, C. S. S. *et al.* Epitaxially connected PbSe quantum-dot films: Controlled neck formation and optoelectronic properties. *ACS Nano* **8**, 11499–11511 (2014).
28. Kang, I. & Wise, F. W. Electronic structure and optical properties of PbS and PbSe quantum dots. *J. Opt. Soc. Am. B* **14**, 1632 (1997).
29. Allan, G. & Delerue, C. Confinement effects in PbSe quantum wells and nanocrystals. *Phys. Rev. B* **70**, 1–9 (2004).
30. Delerue, C. & Vanmaekelbergh, D. Electronic band structure of zinc blende CdSe and rock salt PbSe semiconductors with silicene-type honeycomb geometry. *2D Mater.* **2**, 34008 (2015).
31. Beberwyck, B. J., Surendranath, Y. & Alivisatos, A. P. Cation exchange: A versatile tool for nanomaterials synthesis. *J. Phys. Chem. C* **117**, 19759–19770 (2013).
32. Luther, J. M., Zheng, H., Sadtler, B. & Alivisatos, A. P. Synthesis of PbS nanorods and other ionic nanocrystals of complex morphology by sequential cation exchange reactions. *J. Am. Chem. Soc.* **131**, 16851–16857 (2009).
33. Tadjine, A. & Delerue, C. Colloidal nanocrystals as LEGO® bricks for building electronic band structure models. *Phys. Chem. Chem. Phys.* **20**, 8177–8184 (2018).
34. Steckel, J. S., Yen, B. K. H., Oertel, D. C. & Bawendi, M. G. On the mechanism of lead chalcogenide nanocrystal formation. *J. Am. Chem. Soc.* **128**, 13032–13033 (2006).

Appendix

A3.1 Light absorption by superlattices consisting of a monolayer of unattached PbSe NCs

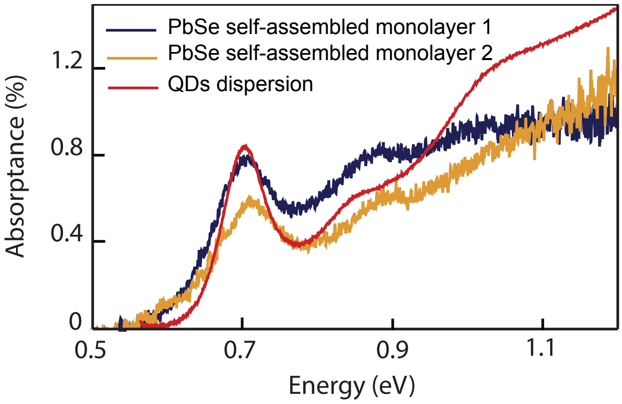

Figure A3.1. Absorption spectrum of two samples with self-assembled monolayer of PbSe NCs. These monolayers of PbSe NCs has an absorptivity of 0.7 ± 0.1 %, thus considerably smaller than $\pi\alpha/nc = 1.6$ %. The red curve shows the absorption of PbSe QDs suspended in tetrachloroethylene as a reference.

A3.2 The molar concentration of the PbSe monolayer

To calculate the molar concentration of the PbSe self-assembled monolayer, we took the TEM image of the monolayer and count the number of QDs in the image (765) and divided by the area of the image (1.8×10^{-9} cm^2). Division of this value by N_A gives the molar concentration of the monolayer equal to 7.03×10^{-13} molcm^{-2}.

A3.3 Tight-binding (TB) calculations of PbSe square superlattice

The band structure of two-dimensional PbSe square superlattices of PbSe NCs is calculated by Christoph Delerue using a tight-binding (TB) approach. Here, we describe the TB calculation details for better understanding. Each 4 atoms in the superlattice is described by a double set of $sp^3d^5s^*$ atomic orbitals, including the spin degree of freedom. The orbitals are assumed to be orthogonal and the matrix elements between two orbitals are restricted to the nearest-neighbor interactions. The spin-orbit coupling is included. We consider square lattices of spherical NCs of diameter D. All NCs are equivalent by translations in the [001] crystallographic plane. We set the center-to-center distance a (the lattice parameter) between nearest-neighbor NCs equal to D, *i.e.*, the spheres are tangential. Between each pair of neighboring NCs, we add a cylinder of atoms that serves as a bond. The cylinders are oriented along [100] and [010] crystallographic directions. The diameter d ofthe cylinders determines the strength of the coupling between NCs. In the present work, we used D = 5.5 nm and d = 2.2 nm. A lattice parameter of 5.5 nm is consistent with the TEM images. A cylinder diameter of 2.2 nm seems to be a reasonable value, also from TEM measurements.

In the case where the superlattice of PbSe is occupied by N electrons per NC, we calculate the Fermi energy by integration of the density-of-states, assuming a Fermi-Dirac distribution at 300 K. We compute the imaginary part of the dielectric function in the independent particle approximation as:

$$\epsilon_i(\omega) \propto \frac{1}{N_k} Im \sum_{i,j,k} [f_i(k) - f_j(k)] \frac{| \langle i,k \mid e.\nabla | \, j,k \rangle |^2}{\hbar\omega - E_{ij}(k) + i\eta} \qquad \text{(Eq. A3.1)}$$

Where |j,k> is the electronic state in band j and wave vector k, f_j (k) its thermal population, E_{ji} (k) is the difference between energies of states|j,k> and |i,k>, η is small imaginary part (30 meV), and e is the polarization of the light (here, in-plane). We consider N_k vectors k defined on a regular grid in the Brillouin zone. We have checked that, with $N_k = 10^4$, the result is fully converged. The matrix element is rewritten as:

$$\langle i,k \mid e.\nabla | \, j,k \rangle = i \frac{m_0}{\hbar^2} \langle i,k \mid e.\nabla_k H(k) \mid j,k \rangle \qquad \text{(Eq. A3.2)}$$

Where H(k) is the tight-binding Hamiltonian matrix defined in the basis of Bloch states. This equation assumes that all intra-atomic matrix elements of the momentum can be neglected. This approximation, validated in many situations, leads to a gauge invariant representation.

In the calculations, we neglect local field effects, which are justified since we are not interested in the absolute value of the absorption coefficient but in the relative variations with respect to the electronic population of the bands. Excitonic effects are also neglected. This is a good approximation in PbSe because of the high dielectric constant of this material ($\varepsilon_r \approx 23$). The independent-particle approximation is reasonable when the number N of electrons per NC is small (*e.g.*, N = 0, 1, 2). For example, it explains very well the intra-band optical transitions in charged CdSe NCs and the polarizability of charged InAs NCs.

A3.4 Energy Dispersive X-ray Spectroscopy mapping of PbSe honeycomb superlattice

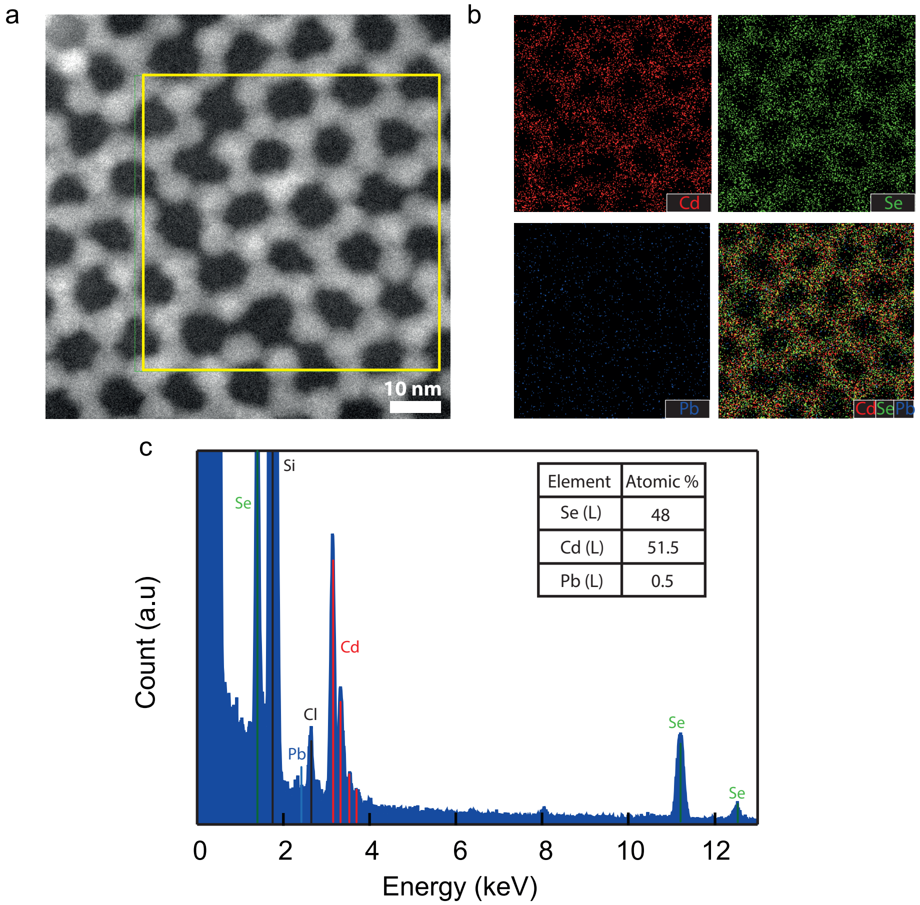

Element	Atomic %
Se (L)	48
Cd (L)	51.5
Pb (L)	0.5

Figure A3.2. (a) Scanning Transmission Electron Microscopy (STEM) image of a honeycomb superlattice. (b) Energy Dispersive X-ray (EDX) spectroscopy elemental maps of the superlattice showing the complete replacement of Pb by Cd. (c) EDX spectrum for the fully ion exchanged sample, showing a very small value of 0.5 % Pb, 48 % Se and 51.5 % Cd.

Chapter 4

Transport properties of a two-dimensional PbSe square superstructure in an electrolyte-gated transistor

Abstract

Self-assembled nanocrystal solids show promise as a versatile platform for novel optoelectronic materials. Superlattices composed of a single layer of lead-chalcogenide and cadmium-chalcogenide nanocrystals with, epitaxial connections between the nanocrystals, present intriguing questions to the community regarding their predicted band structure and electronic transport properties. However, the as prepared materials are intrinsic semiconductors; to occupy the bands in a controlled way, chemical doping or external gating is required. Here, we show that square superlattices of PbSe nanocrystals can be incorporated as a nanocrystal monolayer in a transistor setup with an electrolyte gate. The electron (and hole) density can be controlled by the gate potential, up to 8 electrons per nanocrystal site. The electron mobility at room temperature is 18 $cm^2V^{-1}s^{-1}$. Our work forms a first step in the investigation of the band structure and electronic transport properties of two-dimensional nanocrystal superlattices with controlled geometry, chemical composition, and carrier density.

4.1 Introduction

The optoelectronic properties of nanocrystal (NC) solids have been extensively investigated in the past decade. These systems are generally prepared by the assembly of NCs from a nearly monodisperse suspension. Once assembled in the solid phase, the individual NC building blocks are separated by (in)organic capping molecules, forming a tunnel barrier for the charge carriers.[1–11] The nature and length of the capping determines the width and height of the tunneling barriers and hence the dot-to-dot tunneling rates and carrier mobility.[12–15] By advanced engineering, reasonable carrier mobilities (0.1-20 $cm^2V^{-1}s^{-1}$) have been reached in NC solids.[5,16–24] These three-dimensional (3D) films consist of NC quantum dots that are coupled via ligands in three dimensions. They are important for understanding (hopping-controlled) electron transport and for applications in 3D optoelectronic devices such as solar cells and LEDs. Here, we present an optoelectronic study of a genuine 2D superlattice, a PbSe NC monolayer sheet of (truncated) cubic nanocrystals that are epitaxially connected and thus electronically coupled in the lateral directions only *via* their {100} facets. Quantum confinement prevails in the direction perpendicular to the sheet. It is important to realize that the effect of the lateral nanogeometry on the band structure is very strong in such systems. We remark that a study of a similar superlattice, however consisting of several NC monolayers has been presented in ref. [29]. The evolution of the band structure in a bi- and multilayer superlattice is presented in the Appendices (Figure A4.4).

Recently, two-dimensional Pb-chalcogenide (PbS, PbSe, PbTe) systems have been prepared by interfacial nanocrystal assembly and attachment.[25,26] These systems consist of nanocrystals that are epitaxially connected *via* specific facets; this results in quantum wells[27] or 2D systems with a square or honeycomb arrangement of the nanocrystals.[25] In square 2D lattices, the nanocrystals are epitaxially connected *via* the {100} facets as shown in Figure 2.3c in Chapter 2. This oriented attachment process results in a square superstructure in which the voids are due to the truncated cubic shape of the NC building blocks. The electronic coupling in these systems is determined by the size of the PbSe crystalline neck, and a substantially larger electronic coupling is expected compared to NC solids in which the crystals are connected by ligands.[28,29] Calculations show that, provided that the coupling between the crystals is strong enough, a novel material is developed with a geometry-specific band-structure.[28] In that respect, it has recently been calculated that two-dimensional superstructures with a honeycomb geometry show Dirac-type valence- and conduction bands, combining semiconductor properties with those of graphene.[30] However, from an electronic viewpoint the as-prepared 2D superlattices are intrinsic semiconductors. To populate the conduction (valence) bands with electrons (holes) in a controlled way, chemical doping or external gating is required. Here, we show that square superlattices of PbSe nanocrystals, which were self-assembled on top of a liquid substrate, can be transferred and incorporated as a nanocrystal monolayer in a transistor setup with an electrolyte gate.

We studied the injection of carriers by using three types of liquid electrolyte gating. We found that provided the PbSe surface is protected from oxygen and water electrons can be reversibly injected and extracted up to about eight electrons / NC site. Thus, the lowest conduction bands of the superstructure become occupied. In two-probe measurements, we find a rapid rise of the electron mobility up to 5 cm^{2}V^{-1}s^{-1}. A four-probe geometry eliminates the contact resistance and enables measurements on small, more homogeneous sheets. In a monolayer of the superstructure, we then measure an electron mobility as high as 18 cm^{2}V^{-1}s^{-1}.

4.2 Formation of a 2D square superlattice

PbSe superlattices are formed by assembling PbSe nanocrystals in a monolayer at the toluene suspension/nitrogen interface after which the nanocrystals attach *via* their four vertical {100} facets. The mechanism has been reported recently[31] (see details in Appendix A4.1). After the oriented attachment, the superlattice was annealed at 80 °C for 20 min for the differential capacitance measurements and annealed stepwise at 30°, 50°, and 80° for each 15 min for the optical bleach and four-probe measurements. A part of a monolayer sheet is shown in the inset of Figure 4.1a. The absorption spectrum of such a single layer is presented in Figure 4.1a. It can be seen that the absorption peak shows a red shift and a broadening compared to PbSe NCs in suspension. The red shift is due to polarization effects.[32] The peak broadening is caused by the quantum mechanical coupling between the NCs in the superlattice.[18] The absorptivity of the monolayer is about 1.5 % as presented for similar sample in Chapter 3; this is in good agreement with optical transitions in a quantum membrane as reported recently.[33]

Figure 4.1b shows the band structure obtained from a tight binding (TB) calculation. The calculated absorption spectrum, depicted in Figure 4.1c, shows a first peak related to the transitions between the S-type envelope functions and a second peak corresponding to the transitions between the P-type envelope functions. The experimental absorption spectrum shows a similar peak at 0.7 eV. This peak can now be related to the valence-to-conduction band transitions involving the band resulting from coupling of the S-type envelope functions. It is important to note that the S-bands in Figure 4.1b are 8-fold degenerate.

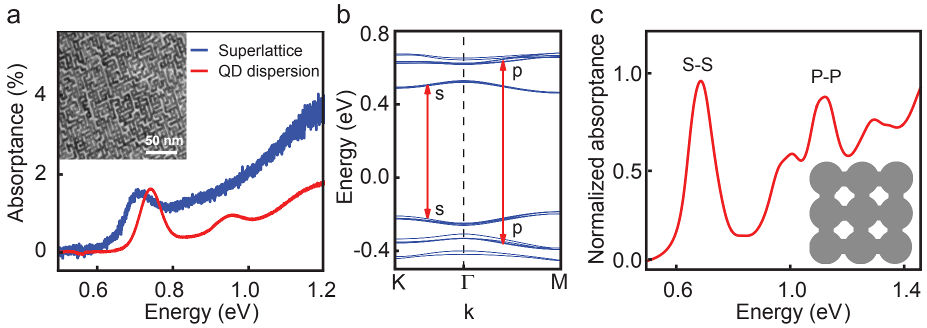

Figure 4.1. (a) Absorption spectrum of a monolayer of a square PbSe superlattice annealed at 80 °C. The red curve shows the absorption of a suspension of nanocrystals as a reference. Inset: Transmission electron microscope image of a part of a PbSe square lattice (monolayer) prepared by self-assembly and oriented attachment at 80 °C; the scale bar indicates 50 nm. (b) Tight-binding band structure for a square superlattice. The S–S and P–P valence-to-conduction band optical transitions are indicated with arrows and these lead to the first two absorption features in panel c. (c) Calculated tight-binding absorption spectrum for a square PbSe superlattice. Inset: geometry used for the calculation. The nanocrystals are modeled as spheres with a diameter of 5.5 nm. The spheres are connected by cylinders of 2.2 nm in length.

The 2D PbSe NC monolayer superstructure (see Figure 4.1a, inset) is scooped from the ethylene glycol substrate and is put on top of the transistor electrodes by horizontal contact approaching with the device from above. The quality and uniformity of the superlattice sheet is checked by visual inspection. To enable a relation between the electrical transport properties and the atomic structure of the superlattice, a part of the NC superstructure was put on a TEM grid for structural characterization (see Figure A4.2).

4.3 Optical and electrical characterization of the superlattice in a transistor

To investigate the behavior of the quantum-dot superlattice with a liquid gate, three independent experiments were performed. By means of an optical bleaching experiment and a differential capacitance measurement the carrier density has been quantified. The sheet conductance was determined by two- and four-probe conductance measurements in a Hall-bar geometry. These three different experiments require different chip designs; Figure A4.3 shows their schematic representations. All three designs are gold structures patterned on a Si–SiO_2 wafer by optical or e-beam lithography. The three different experiments use a different electrolyte and a different gating setup.

In all devices, the material is contacted by a source and drain electrode; the area in between the source and drain is the active channel of the device. An applied potential difference between the channel and the gate causes ions of opposing polarities to migrate to the surface of the gate and to the surface of the sample. Near the sample, the ions form an electrical double layer. This electrical double layer can induce carrier densities that outperform a conventional back gate by an order of magnitude, due to the close proximity of the ions to the material.

The first device type is used for the optical measurements and this design is characterized by a large grating of gold electrodes on top of a thin layer of Al, which serves as an optical reflector. The Al layer is covered with a 90 nm thick layer of Al_2O_3 and is thus electrically isolated from the gold-electrode system. In these measurements, we used an ion-containing gel that is, polyethylene glycol (PEG) with a Li^+ salt; a Pt/Ag wire was inserted to act as counter and reference electrode, respectively. This gel has the additional advantage that it forms a partial blocking layer for atmospheric oxygen and water. The gate potential was set by applying a potential to the counter electrode with respect to the reference electrode using a potentiostat.

The second device is dedicated to differential capacitance and conductivity measurements. Here, the superlattice is contacted by interdigitated source and drain electrodes, spaced 10 to 100 μm apart, with a total device length between 5 and 1000 mm. The device was topped with anhydrous acetonitrile with 0.1 M lithium perchlorate as salt in which a counter and a reference electrode (Pt and Ag wires, respectively) were inserted. For this measurement the PbSe surface was passivated by a $PbCl_2$ treatment. Here again, the gate voltage is set on the counter electrode with respect to the reference electrode using a potentiostat. We measured the potential of the sample vs the Ag reference electrode. An increasingly negative potential on the axis of the figures means that we increase the Fermi-level in our PbSe active layer and, eventually, electron injection sets on.

The final type of chip design consists of several micrometer-sized Hall-bar structures, enabling four-probe conductance measurements. For the four-probe measurements the ionic-liquid DEME-TFSI was used and capped by a thin glass slide to protect the sample from water and oxygen. The potential was set on an Au gate pad evaporated on the chip with reference to the ground.

These different setups and different electrolytes used cause differences in the response of the Fermi-level in the sample to a voltage on the gate. First, the alignment with the vacuum level is different in all setups, and this causes an offset in the gate-axis. Second, there is a difference in the coupling of the voltage on the gate to the shift in Fermi-level.

4.3.1 Determination of the carrier density from the optical bleach

To quantify electron injection into the PbSe superlattice, its optical absorption was measured during gating. The conduction band occupation of the PbSe superstructures can be monitored by measuring the quenching of the interband absorption. Figure 4.2a shows the absorption difference at different values of the applied potential for two cyclic potential scans. The second CV cycle almost reproduces the absorption features of the first cycle. This demonstrates that the electrons can be reversibly injected into and extracted from the superlattice. As it is shown in Figure 4.2b, at potentials more negative than V_G = -1.22 V absorption quenching sets in, first at low photon energy between 0.55 and 0.8 eV related to the $1S_hS_e$ transition. With more negative potentials (V_G = -1.46 V to V_G = -1.69 V), the quenching obtains more weight and also extends to higher photon energies. At even more negative potentials, absorption quenching saturates in the energy region 0.55–0.8 eV. This is illustrated by the inset in Figure 4.2b where the fractional absorptance versus applied potential is plotted for both the S-S and P-P transitions. We observe that ΔA/A becomes equal to 1 at a potential of V_G = -1.53 V for the S-S transition. Concomitantly, the absorption quenching in the range 0.8 to 1.2 eV becomes gradually more important with more negative gate potentials. This feature can be related to $1P_hP_e$ transition.

It should be noticed that the energy width of the absorption bleach (0.55-1.2 eV) is about twice that of the voltage region over which quenching occurs (V_G = -1.22 V to -1 V). This reflects that the band occupation involves the conduction band only but results in quenching of optical transitions from the valence to conduction bands, both bands having a nearly symmetric energy-wave vector dispersion.

At a photon energy of 0.7-0.8 eV, the quenching saturates at a potential of V_G = -1.53 V (Figure 4.2b) to a value of 1.4 %, in close agreement with 1.5 % absorptance of the superstructure (Figure 4.1b). At more negative potentials, the quenching extends to photon energies between 0.9 and 1.2 eV, that is quenching of the P-P transition indicating the onset of occupation of the P-bands.

In Figure 4.2a, two other features can also be distinguished. First, we observe a high energy bleach in the range between 2.0 to 2.5 eV. In the Appendices (Figure A4.5), we present TB calculations, which suggest that this feature can be related to the transition of the second L valley in the valence band of bulk PbSe to the lowest state in the conduction band. Second, in the range 1.45 eV to 1.65 eV, we observe a positive signal that can possibly be attributed

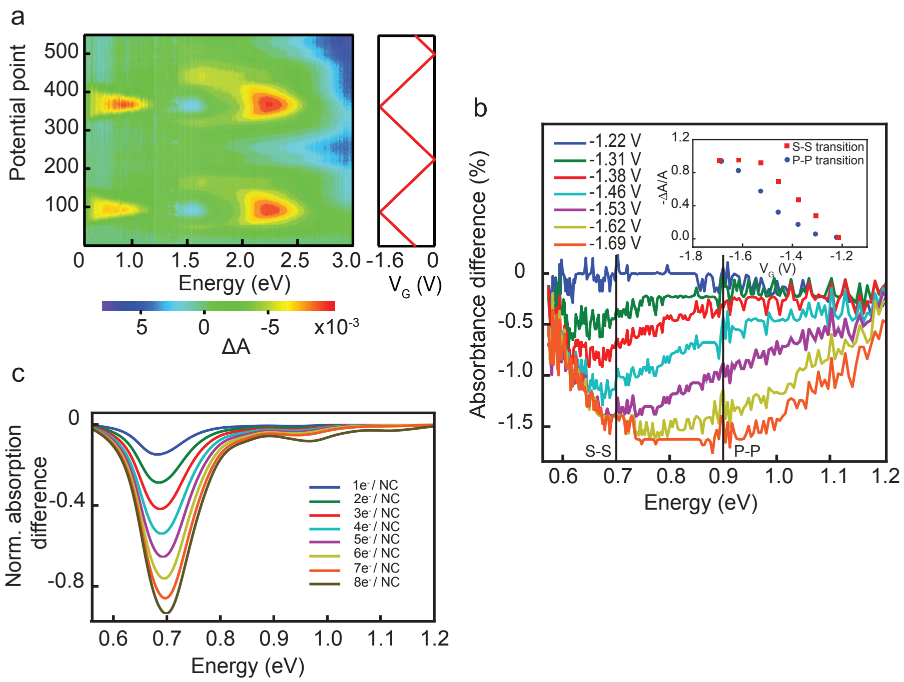

Figure 4.2. (a) Changes in the absorptance on sweeping the gate twice between V_G = 0 and -1.6 V. (b) The absorptance quenching measured at more and more negative potentials; electron injection starts at V_G = -1.22 V(dark blue curve) that can be seen as a reference. With more negative potentials, the quenching initially becomes more dominant at low-photon energy and extends to the high-energy range for the most negative potentials applied. Inset: relative differential absorption for the S-S and P-P transitions at energies of 0.7 eV and 0.9 eV, respectively. (c) Tight-binding calculation of the absorption quenching on the basis of the band structure presented in Figure 4.2b. The gradual increase and saturation of the bleach feature can be understood by a progressive filling of the 8-fold degenerate S-type conduction band and partial occupation of the P-band, due to thermal activation at 300 K. The band structure for a 2D PbSe square superlattice has been calculated by Kalesaki *et al.* [28] we remark here that the degeneration is lifted by coupling, resulting in four 2-fold degenerate S-bands that are weakly separated. The resulting quenching spectrum upon electron occupation of the S-bands with one to eight electrons is presented in Figure 4.2c. The main features of the absorption quenching, that is, the gradual shift of the quenching peak to higher energies, the saturation at the low-energy side, and the upcoming quenching of the P-P transition at more negative potentials are all well captured by the calculations.

to induced absorption. However, interpretation of these features may be affected by the relative strong background.

4.3.2 Differential capacitance and conductivity measurement

To qualify the electron injection into the superlattice, we measured the differential capacitance as a function of the gate voltage. The PbSe superlattices were either as prepared or passivated with $PbCl_2$. We observed that in general the injection and extraction of electrons occurred in a more reversible way with the passivated superlattices. A typical example is presented in Figure 4.3.

Figure 4.3a shows the differential capacitance acquired between V_G = - 0.2 V and -1.2 V. Electron injection sets in at V_G = - 0.7 V, meaning that the channels Fermi level crossed the conduction band. In the backward scan, the Fermi level went below the conduction band approximately at the same potential. However, asymmetry in the differential capacitance curve indicates a loss of electrons by an electrochemical process related to the impurity of the electrolyte solution or the trap states of the superstructure itself. The charge density and the number of charge per NC in the forward scan at every gate potential is displayed in Figure 4.3b. At the most negative potential in this experiment (V_G = -1.2 V), one electron on average was injected to each NC. In this experiment, the uncertainty of the electron density is relatively large because the value of the charge density is calculated based on an estimation of the number of NC sites on the gated part of the PbSe superlattice (see more details in the Appendix A4.5).

In order to investigate the conductivity of the superstructure, the source-drain current upon applying a small bias of 25 mV in a two-probe configuration was recorded. The resulting current-voltage curves are Ohmic when the Fermi level is in the conduction band and their slopes give the conductance (see Figure A4.6). From the conductance and the geometry of the gap, the conductivity of the PbSe superlattice can be obtained as a function of the gate potential (see conductivity and mobility calculation in Appendix A4.5). As illustrated by Figure 4.3c the conductivity sets in at V_G = -0.7 V and increases to 500 S/m at V_G = -1.2 V. The small value observed in the band gap region is related to the faradaic current.

The electron mobility calculated from the charge density and conductivity rises to a

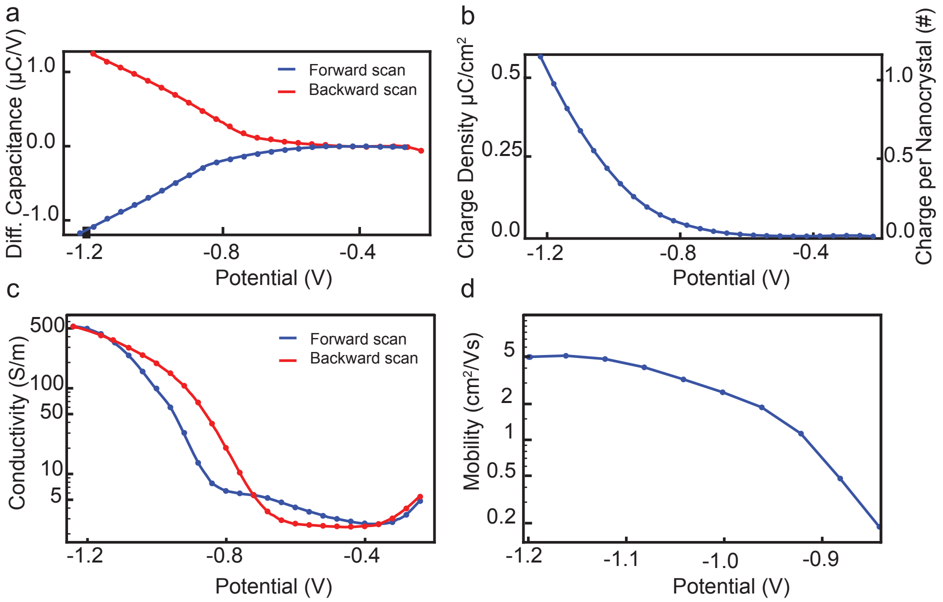

Figure 4.3. (a) Differential capacitance of a PbSe superstructure measured in forward (from −0.2 V to −1.2 V) and backward scan. (b) Charge density and charge per nanocrystal of the PbSe superstructure in the forward scan. (c) The conductivity obtained from the source-drain current and the geometry of the gap (on a logarithmic scale). (d) Electron mobility of the superstructure at the potentials where the Fermi level is above the band gap (logarithmic scale).

maximum of about 5 $cm^2V^{-1}s^{-1}$ at a potential of V_G = -1.1 V and stays constant at more negative potential (see Figure 4.3d). We measured several different samples and found similar values of electron mobility. It should be mentioned that on more "sensitive" devices (*i.e*, longer finger length) the measured mobility can be smaller due to a significant contribution of the contact resistance to the total conductance. The influence of such contact resistance was also observed in previous works.[23,34]

4.3.3 Four-probe measurements

In order to study the 2D square superlattice in small and more homogeneous parts, Hall- bar shaped devices were fabricated (schematic shown in the inset of Figure 4.4b). This device geometry enables to study the two-probe and four-probe conductance. The two-terminal measurements are performed over the inner contacts (2 µm by 16 µm). Four-terminal measurements were performed by sending a current across the two outer contacts while measuring the potential difference between the two inner contacts. The results for the resistance in the electron conduction channel are summarized in Table A4.1. We found that the contact resistance varies from device to device, and dominates in all devices with values ranging between 300 kΩ to 30 MΩ.

To estimate the gate-efficiency in the Hall bar field-effect devices, we measured the ambipolar operation of the field-effect transistors. In Figure 4.4a, the source drain two-probe conductivity is shown on a log-scale; the rise of the conductance observed at voltages below V_G = - 1.2 V shows that electrons are injected in the conduction band. In addition, a linear source-drain conductance is also observed at voltages positive of V_G = - 0.3 V indicating the injection of holes in the highest valence band. The ambipolar operation of the electrolyte gated transistor enables us to relate the insulating gap between V_G = - 1.2 V and - 0.3 V to the band gap of the PbSe superlattice. However, to obtain the single-particle gap it has to be corrected for the gate efficiency. Assuming a linear response of the carrier density on to the gate voltage, that is efficient screening and small charging energies, the gate efficiency is found to be about 0.8 eV/V.

The presence of a sizable contact resistance means that the mobility is underestimated in two-terminal measurements of small devices. We therefore performed four-terminal measurements to obtain a more accurate estimation of the intrinsic mobility. Figure 4.4b shows the gate response of the four-probe conductance in the electron conduction channel. We observe a dramatic increase in conductance when ramping up the gate. Figure 4.4c shows the linear IV characteristics, from which we calculate the conductance and the mobility given the electron density estimated from the optical bleach experiments. Because the complete absorption bleach of the first optical transition occurs at full occupation of the lowest eight bands, the electron density is thus estimated as 8 electrons/NC. We estimate the number of NCs from TEM images to be 2.9×10^{12} NCs/cm^2, giving 2.3×10^{13} electrons/cm^2. The four-probe mobility of the 13 devices spread over 5 different substrates that were investigated are presented in Table A4.1; the values vary between 1 and 18 $cm^2V^{-1}s^{-1}$.

4.4 Discussion

Electron and hole transport in self-assembled nanocrystal solids has been studied in

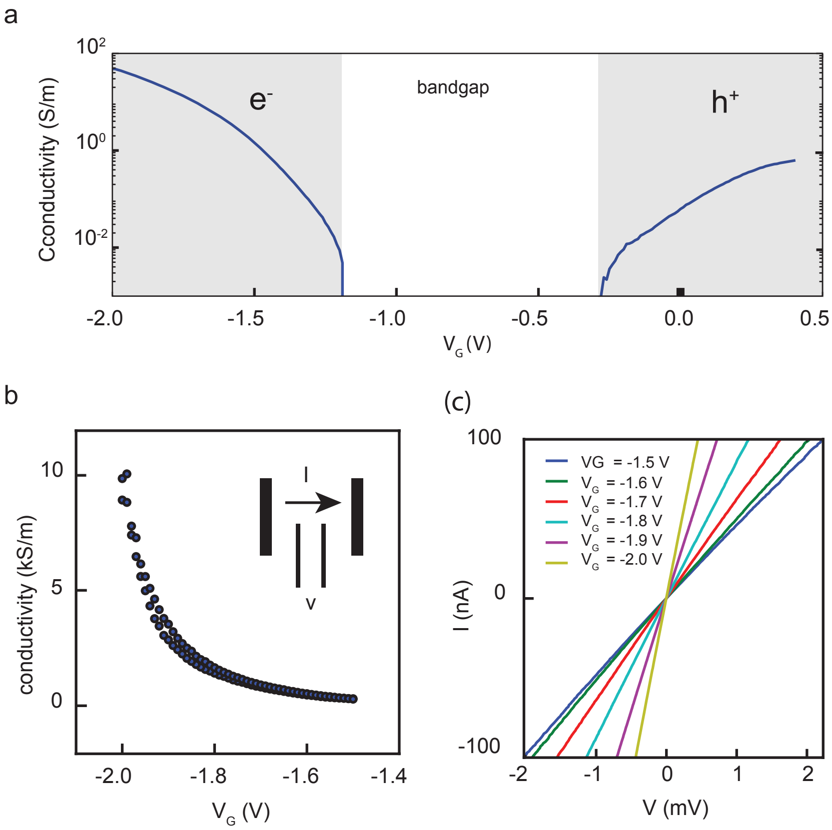

Figure 4.4. (a) Two-probe conductivity on a log-scale. The insulating region is due to the band gap of the PbSe superlattices. (b) The conductivity measured as a function of the gate voltage under conditions of electron injection. The conductivity was measured by setting a constant current of 10 nA between the two outer contacts while measuring the resulting voltage between the two inner contacts. The gated PbSe superlattice has dimensions of 2 μm (distance between the probes) by 16 μm (width of the channel). (c) Current between the outer contacts versus the voltage measured on the inner contacts for different gate voltages, showing that the current-voltage relationship is linear at all electron densities. In this measurement, the gate voltage is applied on the liquid gate pad.

the last two decades both for the intrinsic transport physics as for the possible use of these systems in optoelectronic devices.[1–11] Roughly spoken, we can distinguish three classes of quantum dot solids: The first class consists of NC solids as obtained from a NC dispersion by solvent evaporation or addition of a bad solvent. In these NC solids, the surfaces of the nanocrystals remain capped with the organic ligands. The electron tunneling barriers between adjacent NCs are thus 1-2 times the length of the capping molecules, amounting to 1-3 nm. Such barriers result in a weak coupling between the NCs. Transport characterization in such systems show carrier mobilities below 0.1 $cm^2V^{-1}s^{-1}$, limited mainly by carrier tunneling between the localized nanocrystal energy levels. In the second class of solids, the width and the height of the tunneling barriers is reduced by replacing the organic ligands by a variety of short (in)organic ligands. In these systems, the carrier mobility is drastically enhanced to above 1 $cm^2V^{-1}s^{-1}$. In some cases, values of 20 $cm^2V^{-1}s^{-1}$ are reached;[35,36] the increase of the mobility with decreasing temperature points to band-type transport.[3,14,37,38] In other words, the quantum coupling is sufficiently strong to result in (mini)bands.[28,30] Transport of the carriers in minibands is then limited by scattering to phonons.

The system that we report on here belongs to the third class of solids. Nanocrystals of the Pb-chalcogenide compounds have a rock salt crystal structure and a truncated cubic or, truncated octahedral, shape. The oleic acid capping on the {100} facets is weakly bound and desorption of the capping can result in two- dimensional and three-dimensional solids in which the nanocrystals are epitaxially connected with the occurrence of atomically coherent domains of variable size.[13–15] Atomistic theory shows that minibands arise that depend on the geometry of the superlattice. In quasi 2D structures with a square arrangement of the PbSe NCs, Whitham *et al.*[29] observed mobilities in the order of 0.5 $cm^2V^{-1}s^{-1}$.

Here, we report the first study of electron transport in a 2D system with square geometry, in which band occupation is ensured by the high electron densities between 1 and 8 electrons per NC site. Such high electron densities in 2D systems are typical for 2D systems that are electrolyte gated.[16,17] The electron mobility observed here between 5 and 18 $cm^2V^{-1}s^{-1}$ is comparable to the those observed in the second class of NC solids (see above). The temperature-dependence of carrier transport will reveal if band like transport is obtained in these systems. We should remark here that the transistor mobilities that we report are roughly an order of magnitude smaller than those obtained from terahertz spectroscopy.[39] With the latter method, transport is probed over a length of only a few nanocrystals. We should hence conclude that the mobilities for long-range transport reported here are most likely still limited by structural defects and the size of the atomic coherent domains.

References

1. Drndić, M., Jarosz, M. V., Morgan, N. Y., Kastner, M. A. & Bawendi, M. G. Transport properties of annealed CdSe colloidal nanocrystal solids. *J. Appl. Phys.* **92**, 7498–7503 (2002).
2. Woo, W. K. *et al.* Reversible charging of CdSe nanocrystals in a simple solid-state device. *Adv. Mater.* **14**, 1068–1071 (2002).
3. Houtepen, A. J. & Vanmaekelbergh, D. Orbital occupation in electron-charged CdSe quantum-dot solids. *J. Phys. Chem. B* **109**, 19634–19642 (2005).
4. Yu, D., Wang, C., Wehrenberg, B. L. & Guyot-Sionnest, P. Variable range hopping conduction in semiconductor nanocrystal solids. *Phys. Rev. Lett.* **92**, 1–4 (2004).
5. Talapin, D. V & Murray, C. B. Supporting Online Material for PbSe Nanocrystal Solids for n-and p-Channel Thin Film Field-Effect Transistors. *Science* **310**, 86–90 (2005).
6. Vanmaekelbergh, D. & Liljeroth, P. Electron-conducting quantum dot solids: Novel materials based on colloidal semiconductor nanocrystals. *Chem. Soc. Rev.* **34**, 299–312 (2005).
7. Law, M. *et al.* Structural, optical, and electrical properties of PbSe nanocrystal solids treated thermally or with simple amines. *J. Am. Chem. Soc.* **130**, 5974–5985 (2008).

8. Khon, E. *et al.* Inorganic solids of CdSe nanocrystals exhibiting high emission quantum yield. *Adv. Funct. Mater.* **22**, 3714–3722 (2012).
9. Oh, S. J. *et al.* Stoichiometric control of lead chalcogenide nanocrystal solids to enhance their electronic and optoelectronic device performance. *ACS Nano* **7**, 2413–2421 (2013).
10. Crooker, S. A., Hollingsworth, J. A., Tretiak, S. & Klimov, V. I. Spectrally Resolved Dynamics of Energy Transfer in Quantum-Dot Assemblies: Towards Engineered Energy Flows in Artificial Materials. *Phys. Rev. Lett.* **89**, 18–21 (2002).
11. Roest, A. L., Houtepen, A. J., Kelly, J. J. & Vanmaekelbergh, D. Electron-conducting quantum-dot solids with ionic charge compensation. *Faraday Discuss.* **125**, 55 (2004).
12. Chiu, S. C., Jhang, J. S., Chen, J. F., Fang, J. & Jian, W. Bin. Effects of cross-sectional area on the tunneling-junction array in octahedral PbSe colloidal-nanocrystal solids. *Phys. Chem. Chem. Phys.* **15**, 16127–16131 (2013).
13. Liu, W., Lee, J. S. & Talapin, D. V. III-V nanocrystals capped with molecular metal chalcogenide ligands: High electron mobility and ambipolar photoresponse. *J. Am. Chem. Soc.* **135**, 1349–1357 (2013).
14. Jang, J., Liu, W., Son, J. S. & Talapin, D. V. Temperature-dependent hall and field-effect mobility in strongly coupled all-inorganic nanocrystal arrays. *Nano Lett.* **14**, 653–662 (2014).
15. Nag, A., Zhang, H., Janke, E. & Talapin, D. V. Inorganic surface ligands for colloidal nanomaterials. *Zeitschrift für Phys. Chemie* **229**, 85–107 (2015).
16. Luther, J. M. & Pietryga, J. M. Stoichiometry control in quantum dots: A viable analog to impurity doping of bulk materials. *ACS Nano* **7**, 1845–1849 (2013).
17. Gao, Y. *et al.* Photoconductivity of PbSe quantum-dot solids: Dependence on ligand anchor group and length. *ACS Nano* **6**, 9606–9614 (2012).
18. Sandeep, C. S. S. *et al.* Epitaxially connected PbSe quantum-dot films: Controlled neck formation and optoelectronic properties. *ACS Nano* **8**, 11499–11511 (2014).
19. Koh, W. K., Saudari, S. R., Fafarman, A. T., Kagan, C. R. & Murray, C. B. Thiocyanate-capped PbS nanocubes: Ambipolar transport enables quantum dot based circuits on a flexible substrate. *Nano Lett.* **11**, 4764–4767 (2011).
20. Dong, A., Jiao, Y. & Milliron, D. J. Electronically coupled nanocrystal superlattice films by in situ ligand exchange at the liquid-air interface. *ACS Nano* **7**, 10978–10984 (2013).
21. Kang, M. S., Lee, J., Norris, D. J. & Frisbie, C. D. High carrier densities achieved at low voltages in ambipolar PbSe nanocrystal thin-film transistors. *Nano Lett.* **9**, 3848–3852 (2009).
22. Oh, S. J. *et al.* Engineering charge injection and charge transport for high performance PbSe nanocrystal thin film devices and circuits. *Nano Lett.* **14**, 6210–6216 (2014).
23. Oh, S. J. *et al.* Designing high-performance PbS and PbSe nanocrystal electronic devices through stepwise, post-synthesis, colloidal atomic layer deposition. *Nano Lett.* **14**, 1559–1566 (2014).
24. Kagan, C. R. & Murray, C. B. Charge transport in strongly coupled quantum dot solids. *Nat. Nanotechnol.* **10**, 1013–1026 (2015).
25. Evers, W. H. *et al.* Low-dimensional semiconductor superlattices formed by

geometric control over nanocrystal attachment. *Nano Lett.* **13**, 2317–2323 (2013).

26. Boneschanscher, M. P. *et al.* Long-range orientation and atomic attachment of nanocrystals in 2D honeycomb superlattices. *Science* **344**, 1377–1380 (2014).
27. Schliehe, C. *et al.* Ultrathin PbS sheets by two-dimensional oriented attachment. *Science* **329**, 550–553 (2010).
28. Kalesaki, E., Evers, W. H., Allan, G., Vanmaekelbergh, D. & Delerue, C. Electronic structure of atomically coherent square semiconductor superlattices with dimensionality below two. *Phys. Rev. B* **88**, 1–9 (2013).
29. Whitham, K. *et al.* Charge transport and localization in atomically coherent quantum dot solids. *Nat. Mater.* **15**, 557–563 (2016).
30. Kalesaki, E. *et al.* Dirac cones, topological edge states, and nontrivial flat bands in two-dimensional semiconductors with a honeycomb nanogeometry. *Phys. Rev. X* **4**, 1–12 (2014).
31. Geuchies, J. J. *et al. In situ* study of the formation mechanism of two-dimensional superlattices from PbSe nanocrystals. *Nat. Mater.* **15**, 1248–1254 (2016).
32. Wolcott, A. *et al.* Anomalously large polarization effect responsible for excitonic red shifts in PbSe quantum dot solids. *J. Phys. Chem. Lett.* **2**, 795–800 (2011).
33. Fang, H. *et al.* Quantum of optical absorption in two-dimensional semiconductors. *Proc. Natl. Acad. Sci.* **110**, 11688–11691 (2013).
34. Luther, J. M. *et al.* 001-Schottky solar cells based on colloidal nanocrystal films. *Nano Lett.* **8**, 3488–3492 (2008).
35. Lee, J. S., Kovalenko, M. V., Huang, J., Chung, D. S. & Talapin, D. V. Band-like transport, high electron mobility and high photoconductivity in all-inorganic nanocrystal arrays. *Nat. Nanotechnol.* **6**, 348–352 (2011).
36. Chung, D. S. *et al.* Low voltage, hysteresis free, and high mobility transistors from All-inorganic colloidal nanocrystals. *Nano Lett.* **12**, 1813–1820 (2012).
37. Choi, J. H. *et al.* Bandlike transport in strongly coupled and doped quantum dot solids: A route to high-performance thin-film electronics. *Nano Lett.* **12**, 2631–2638 (2012).
38. Talgorn, E. *et al.* Unity quantum yield of photogenerated charges and band-like transport in quantum-dot solids. *Nat. Nanotechnol.* **6**, 733–739 (2011).
39. Evers, W. H. *et al.* High charge mobility in two-dimensional percolative networks of PbSe quantum dots connected by atomic bonds. *Nat. Commun.* **6**, 1–8 (2015).
40. Allan, G. & Delerue, C. Confinement effects in PbSe quantum wells and nanocrystals. *Phys. Rev. B* **70**, 1–9 (2004).
41. Graf, M. & Vogl, P. Electromagnetic fields and dielectric response in empirical tight-binding theory. *Phys. Rev. B* **51**, 4940–4949 (1995).
42. Delerue, C. & Lannoo, M. Nanostructures: Theory and Modeling (*Springer*, 2006).
43. Delerue, C., Allan, G. & Niquet, Y. M. Collective excitations in charged nanocrystals and in close-packed arrays of charged nanocrystals. *Phys. Rev. B* **72**, 1–6 (2005).
44. Pijpers, J. J. H., Milder, M. T. W., Delerue, C. & Bonn, M. (Multi) exciton dynamics and exciton polarizability in Colloidal InAs Quantum Dots. *J. Phys. Chem. C* **114**, 2–4 (2010).

Appendix

A4.1 Oriented attachment

The square superlattices were prepared by drop casting of 16 μL QDs (5.5×10^{-5} mol/L) dispersion in 3 mL toluene (Figure A4.1 (a) and (b)) on top of the ethylene glycol substrate (Figure A4.1 (c)). The system is left for 45 minutes at 25 °C. Therefore, the toluene will be evaporated and monolayer of oriented QDs is formed (Figure A4.1 (d)). Heating the system at 70 °C for 20 minutes leads to formation of square structure network with stronger atomic connections. The 2D PbSe NC monolayer superstructure is stamped from the ethylene glycol substrate and is put on top of the transistor electrodes by horizontal contact approaching with the device from above (Figure A4.1 (e) and (f)). A part of the NC superstructure was also put on a TEM grid for structural characterization (shown in Figure A4.2 (a)). In the higher magnification image (Figure A4.2 (b)), just a monolayer of the superlattice is observed. A HAADF-STEM image of two square networks is shown in Figure A4.2 (c) and (d). These images show that the nanocrystals are atomically connected *via* their vertical {100}-type facets.

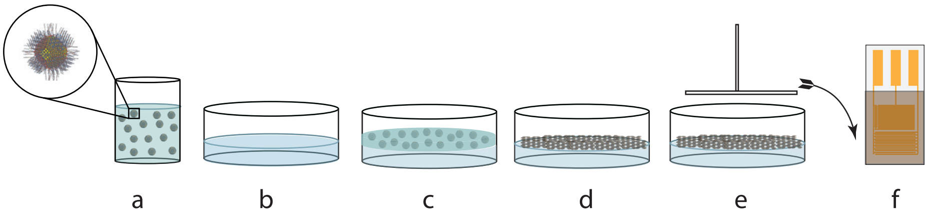

Figure A4.1. (a) Dilution of QDs in toluene, (b) Ethylene glycol substrate, (c) Drop casted QDs on top of the substrate, (d) Evaporation of toluene and formation of the superlattices, (e) Stamping the superstructure on the transistor electrode and (f) Covered fingered electrode by a monolayer of the structure.

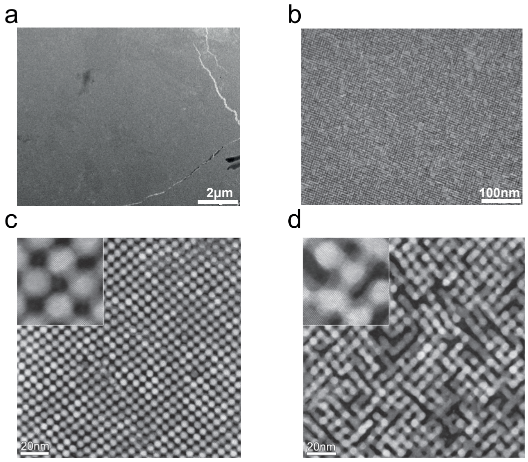

Figure A4.2. Overview of the monolayer square superlattice by (a) TEM image in the scale of 2 μm, (b) magnified TEM image of figure a in the scale of 100 nm, (c) HAADF-STEM image of square lattice showing the connection of nanocrystals by their {100}-type facets, (d) HAADF-STEM image of a square-type lattice showing thicker atomic bridges between the NCs.

A4.2 Electrode designs

Figure A4.3 shows the three different electrode configurations that were used for the experiments. All three designs are gold structures patterned on a Si-SiO_2 wafer by optical or e-beam lithography. For differential capacitance and conductance measurements, the interdigitated gap consists of gold fingers (Figure A4.3a). For *in-situ* absorption measurements an optical window is included which consists of a square grid of gold bars. The second device shown in Figure A4.3b is used for the optical measurements and this design is characterized by a large grating of gold electrodes on top of a thin layer of Al, that is topped by an insulating Al_2O_3 layer. The Al layer results in good reflectivity of the light, enabling us to perform precise absorption quenching measurements on a NC monolayer with an overall absorptivity as low as 1.5 %. The final chip design (Figure A4.3c) consists of several micrometer-sized Hall-bar structures, enabling four-probe conductance measurements. In this design the long leads were isolated from the electrolyte and the superstructure with a thin layer of Al_2O_3 deposited by atomic layer deposition.

For all measurements, the superstructure was gently stamped on top of the fingers. The differential capacitance measurement was performed in an air-tight cell containing anhydrous acetonitrile with 0.1 M lithium perchlorate as salt. For the four-probe measurements, to protect the structure against water and oxygen, a thin glass slid was placed on top of the ionic-liquid electrolyte.

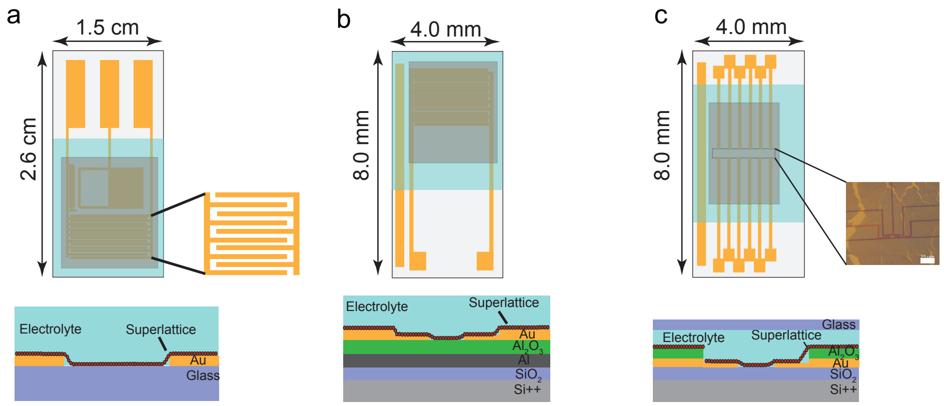

Figure A4.3. Electrode designs used for (a) differential capacitance and conductivity, (b) optical bleach and (c) four-probe measurements.

A4.3 Tight-binding calculations

The band structure of two-dimensional PbSe square lattices of PbSe NCs is calculated using a tight-binding approach detailed in Ref. [22] Each atom in the superlattice is described by a double set of $sp^3d^5s^*$ atomic orbitals, including the spin degree of freedom. The orbitals are assumed to be orthogonal and the matrix elements between two orbitals are restricted to the nearest-neighbor interactions. The tight-binding parameters are those for PbSe, taken from Ref.[40] Spin-orbit coupling is included.

We consider square lattices of spherical NCs of diameter D. All NCs are equivalent by translations in the [001] crystallographic plane. We set the center-to-center distance a (the lattice parameter) between nearest-neighbor NCs equal to D, *i.e.* the spheres are tangential. Between each pair of neighboring NCs, we add a cylinder of atoms that serves as a bond. The cylinders are oriented along [100] and [010] crystallographic directions. The diameter d of the cylinders determines the strength of the coupling between NCs. In the present work, we used D = 5.5 nm and d = 2.2 nm. A lattice parameter of 5.5 nm is consistent with the TEM images. A cylinder diameter of 2.2 nm seems to be a reasonable value, also from TEM measurements, and leads to an optical absorption spectrum in good agreement with experiments (Figure 4.1 of the main chapter).

In the case where the superlattice of PbSe is occupied by N electrons per NC, we calculate the Fermi energy by integration of the density-of-states, assuming a Fermi-Dirac distribution at 300 K. We compute the imaginary part of the dielectric function in the independent-particle approximation as:

$$\epsilon_i(\omega) \propto \frac{1}{N_k}\, Im \sum_{i,j,k}\left[f_i(k) - f_j(k)\right] \frac{|\langle i,k|e.\nabla|j,k\rangle|^2}{\hbar\omega - E_{ji}(k) + i\eta} \qquad \text{(Eq. A.4.1)}$$

where |j,k> is the electronic state in band j and wave vector k, f_j (k) its thermal population, E_{ji} (k) is the difference between energies of states |j,k>and |i,k>, η is small imaginary part (30 meV), and e is the polarization of the light (here, in-plane). We consider N_k vectors k defined on a regular grid in the Brillouin zone. We have checked that, with $N_k = 10^4$, the result is fully converged. A bleach spectrum is defined as the difference between spectra calculated for populations of 0 and N electrons per NC.

The matrix element is rewritten as:[41]

$$\langle i,k|e.\nabla|j,k\rangle = i\,\frac{m_0}{\hbar^2}\,\langle i,k|e.\nabla_k H(k)|j,k\rangle \qquad \text{(Eq. A.4.2)}$$

where H(k) is the tight-binding Hamiltonian matrix defined in the basis of Bloch states. This equation assumes that all intra-atomic matrix elements of the momentum can be neglected. This approximation, validated in many situations, leads to a gauge invariant representation.[41,42]

In the calculations, we neglect local-field effects, which is justified since we are not interested in the absolute value of the absorption coefficient but in the relative variations with respect to the electronic population of the bands. Excitonic effects are also neglected. This is a good approximation in PbSe because of the high dielectric constant of this material ($\varepsilon_r \approx 23$). The independent-particle approximation is reasonable when the number N of electrons per NC is small (*e.g.*, N = 0,1,2). For example, it explains very well the intra-band optical transitions in charged CdSe NCs[43] and the polarizability of charged InAs NCs.[44] In the present work, this is confirmed by the good agreement between calculated and measured bleach spectra shown in Figure 4.2 for gate voltages corresponding to small injected charge. However, for large values of N, especially for N getting closer to 8, we expect that electron-electron interactions will play an increasingly important role. The electron-electron repulsion will tend to push the electronic density from the NC centers to the boundaries of the superlattice, including the inter-NC bonds. This will result in a partial hybridization of S-like bands with P-like (or higher orbitals) ones. In addition, due to electron-electron interactions, the response to the electromagnetic perturbation will involve a many-particle response of increasing importance as N is increased. All these effects could explain why the experimental bleach spectra extent to higher energy than the calculated ones for the highest injected charges (Figure 4.4). The theoretical treatment of such correlation effects in lattices of NCs is beyond the objectives of the present work but should be of high interest in future studies.

A4.4 Band structure of multilayers of 2D NC superlattices

Figure A4.4 shows the evolution of the electronic band structure with adding NC layers on top of the first layer. We assume for simplicity that all layers are identical and the nearest-neighbor NCs of superposed layers are epitaxially connected through their {100} facets. In the case of two layers with very weak connections (coupling) between them (Figure A4.4a), we basically recover the same band structure as for the monolayer (Figure 4.1b of the main chapter). There is just an additional two-fold degeneracy of the bands. When the coupling between the two layers is increased, this band degeneracy is lifted and band dispersions are modified. This is particularly clear in the case where we take the same NC coupling between and within the layers (Figure A4.4b). When the number of layers is increased (5 layers in the case of Figure A4.4c), the number of bands in each manifold (S, P) varies in proportion, the total width of the band manifold increases which results in a broaden density-of-states. The band structure becomes progressively 3D when the quantization of the k-vector of the electronic states in the vertical direction becomes less effective. In that limit, the electron transport becomes 3D instead of 2D.

This evolution of the band structure with the number of layers can be understood by focusing for example on the lowest conduction bands. In the case of the monolayer (Figure A4.4d), there are four (spin-degenerate) bands coming from the four equivalent L valleys of the conduction band of bulk PbSe. The small splittings between them come from inter-valley couplings. However, each band can be described by an effective tight-binding model in which each NC is characterized by one S state of energy E_s.[28] For a square lattice in the xOy plane, the energy dispersion with respect to the 2D wavevector $K = (K_x, K_y)$ can be approximately written as:

$$E_{N=1}(K) = E_s + 2t[\cos(K_x a) + \cos(K_y a)] \qquad \text{(Eq. A.4.3)}$$

where t is the hopping matrix element between S states of nearest-neighbor NCs, N is the number of layers, and a is the lattice parameter (NC-NC distance). The total bandwidth is equal to $8|t|$. The electron transport in these bands is therefore of pure 2D character, especially when inter-valley scattering is negligible, which necessarily occurs at sufficiently low temperature (inter-valley scattering involves high-energy phonons).

In the case of a bilayer, each unit cell is composed of two superposed NCs. The coupling between the S states then results in bonding and antibonding states of energy $E_s \pm t$. In the superlattice, bonding states cannot couple to antibonding states of a neighbor cell. Sectors of bonding and antibonding states are therefore uncoupled which leads to band

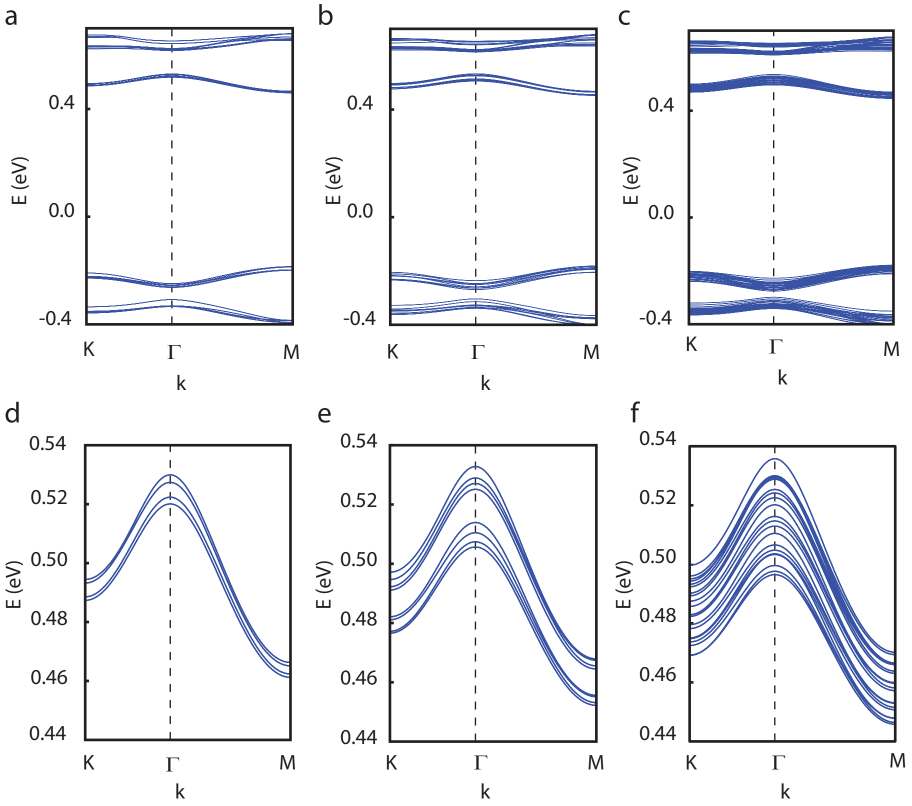

Figure A4.4. (a) Tight-binding band structure for a bilayer of square PbSe superlattices in which the nanocrystals are modelled as spheres with a diameter of 5.5 nm. The spheres are tangent and are connected in-plane (intra-layer) by cylinders of 2.2 nm in diameter (like in Figure 4.1 of the main chapter). In addition, each sphere of the lower layer is connected to the sphere of the upper layer (inter-layer) by a cylinder of 0.5 nm diameter. (b) Same as (a) but the diameter of the inter-layer cylinders is increased to 2.2 nm. (c) Same as (b) but with five layers of NC superlattices instead of two. Detailed view on the lowest conduction bands in a monolayer (d) (zoom in Figure 4.1 of the main document), in a bilayer (e) (zoom in (b)) and in a superlattice made of 5 layers (f) (zoom in (c)).

dispersions of the form:

$$E_{N=2}(K) = E_s \pm t + 2t\left[\cos(K_x a) + \cos(K_y a)\right] \qquad \text{(Eq. A.4.4)}$$

Including the effect of the valley degeneracy, this simple model explains very well the formation of two sets of four bands shown in Figure A4.4e. The distance between the two sets is rather large, approximately 2|t|, *i.e.* one quarter of the total bandwidth of the monolayer. As a consequence, even if the Fermi level crosses the two sets of bands, the transport will be relatively independent in the two sets of channels (bonding/antibonding), it will remain of 2D character.

The situation is clearly different in the film composed of 5 layers (Figure A4.4f) where the band structure is composed many bands which seem to be rather regularly distributed in energy. In fact, this behavior can be understood from the energy dispersion for the 3D lattice:

$$E_{3D}(K_{3D}) = E_s + 2t\left[\cos(K_x a) + \cos(K_y a) + \cos(K_z a)\right] \qquad \text{(Eq. A.4.5)}$$

In a film composed of N layers, the component of K_{3D} along z is quantized due to the quantum confinement: $K_z a = p\pi\backslash(N = 1)$. The allowed solutions are thus given by:

$$E_N(K) = E_s + 2t\left[\cos(K_x a) + \cos(K_y a)\right] + 2t\cos\left(\frac{p\pi}{N+1}\right) \qquad \text{(Eq. A.4.6)}$$

with p = 1...N. Therefore, the number of bands is proportional to N, and the distance between them scales as t\N. The electron transport in these bands becomes of 3D character when electrons can easily scatter from bands to bands, which is probably the case for N = 5 (Figure A4.4f). At increasing N, the total bandwidth tends to 12|t|.

A4.4 High energy bleach

It was mentioned that in Figure 4.2a two high-energy features can be distinguished. To illustrate these features more objectively, we present the absorptance difference versus energy in Figure A4.5a. The high-energy bleach in the visible range of 2.0 eV to 2.5 eV can be related to the transition of the second L valley in the valence band of bulk PbSe to the lowest state in the conduction band. The TB calculation of absorption bleach for the superstructure formed from 3.0 nm and 3.6 nm PbSe QDs is also in line with this hypothesis (Figure A4.5b). For the superstructure formed from 3.6 nm, a positive signal is observed at lower energy which can be attributed to induced absorption. We also distinguished these positive peaks in the range 1.45 eV to 1.65 eV which is in good agreement with TB calculation results.

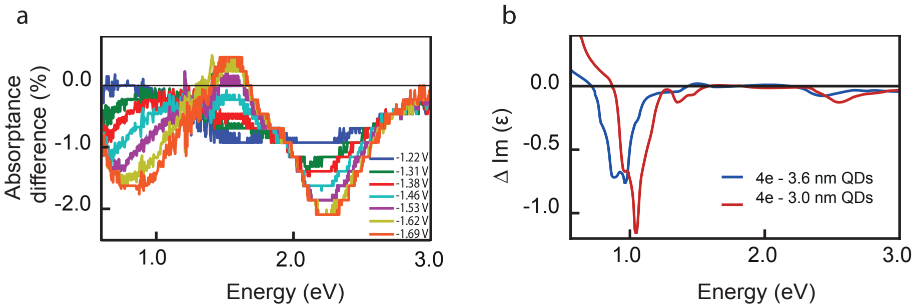

Figure A4.5. (a) The absorption quenching measured between V_G = 0 V and -1.69 V. (b) The TB absorption quenching calculated for four electrons injected in the superstructure with 3.0 nm and 3.6 nm basic QDs.

A4.5 Conductivity and mobility calculation

To calculate the charge density, at first we integrated the differential capacitance over the complete range of applied potential which yields the total amount of charge injected to the superstructure. The next step is to estimate the number of nanocrystal sites on the gated part of the electrode. After stamping the superstructure on the electrode, we visually checked the percentage of the electrode area covered by supperlattices. In addition, we considered that not the whole part of the covered area includes nanocrystals since there are some cracks and empty places between the patches of the superstructure which can be estimated from TEM images. For the sample presented in this work, we roughly considered 40 % coverage of the electrode by the superstructure:

$$n = 0.4\,\frac{Q}{w \times L} \qquad \text{(Eq. A.4.7)}$$

where n is charge density, Q is total charge injected to the system, w and L are electrode width and length.

From the source-drain current *versus* applied potential in transport measurement presented in Figure A4.6, the conductance of the network can be calculated. The conductivity, σ, of the PbSe nanocrystal sheet can be determined from the conductance and the geometry of the fingers:

$$\sigma = \frac{G \times w}{h \times L} \qquad \text{(Eq. A.4.8)}$$

where σ is conductivity, w and L the width and length of the gap, G is conductance and h is monolayer thickness.

Therefore, the mobility can be calculated from the charge density obtained from the differential capacitance measurements and the conductivity of the sheet:

$$\mu = \frac{\sigma}{n \times e} \qquad \text{(Eq. A.4.9)}$$

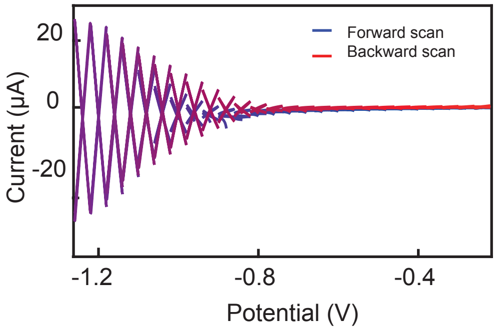

Figure A4.6. Source-drain current versus applied potential. When the Fermi level is inside the conduction band, ohmic behavior starts (at -0.8 V).

A4.6 Conductivity and mobility calculation in four-probe measurements

Table A 4.1 summarizes the resistances measured and the mobility calculated for 13 devices on five different substrates. The resistance values are calculated from the linear IV-curves at V_G = 2.0V. The two-probe IV curves are measured by sweeping the voltage

(-10 mV to 10 mV) between the two inner probes of a device and measuring the current. For the four probe measurements a current was set between the two outer probes of the device, and the voltage drop between the two inner probes was recorded. Before taking an IV, the gate voltage was applied to the gate pad and the sample was left to relax for a minute. Forward and backward sweeps did not show hysteresis. The NC density was estimated from TEM images to be 2.9×10^{12} NC/cm^2. The mobility was then calculated assuming full occupation of the p-orbitals, *i.e.* 8 e^-/NC and full coverage of the device.

	R_{2p}(kΩ)	R_{4p}(kΩ)	μ_{2p}(cm^{2}V^{-1}s^{-1}) 8e^- at V_G = 2V	μ_{4p}(cm^{2}V^{-1}s^{-1}) 8e^- at V_G = 2V
sample A				
device 1	1342	104.8	0.20	2.6
sample B				
device 1	120.3	197	0.57	1.37
device 2	66.7	248	1	1.1
device 3	374.2	71.2	0.18	4.01
device 4	333.3	140	0.82	2.13
sample C				
device 1	3300	200	0.02	1.4
device 2	2500	112	0.03	2.4
device 3	-	40	-	6.8
sample D				
device 1	40	15.2	1.7	18
sample E				
device 1	217.6	121.9	0.3	2.2
device 2	358.7	105	0.2	2.6
device 3	228.8	187.9	0.3	1.4
device 4	474	287	0.1	0.9

Table A4.1. Two- and four probe resistances and mobilities for 13 Hall-bar devices spread over five different samples.

Chapter 5

Room-temperature electron transport in PbSe honeycomb superstructures studied in a transistor configuration and by terahertz spectroscopy

Abstract

2D semiconductors with a honeycomb nanogeometry show a regular band gap, but with Dirac-type conduction and valence bands as in graphene. We report on the band occupation and electron transport in PbSe honeycomb superstructures at room temperature studied by two different methods. First, we incorporated single-layers of PbSe honeycomb structures into transistor-type devices. With electrochemical gating we could populate the lowest conduction band with electrons in a controlled way. The electron mobility was found to be 1.5 ± 0.5 $cm^2V^{-1}s^{-1}$. Second, electrons and holes were photogenerated in freestanding honeycomb superstructures, and we measured the transient terahertz conductivity. The terahertz data show a similar mobility as found in the transistor devices, but also pronounced backscattering by imperfections in the superstructure. The study of Dirac physics in honeycomb semiconductors will require improved superlattices and control of the Fermi level at cryogenic temperatures.

5.1 Introduction

Quantum dot solids composed of colloidal nanocrystals (NCs) have attracted strong interest since about two decades. Such solids show optoelectronic properties that reflect the properties of the individual nanocrystalline quantum dots together with the dipolar and electronic coupling between them. Since there are many types of NCs that can be incorporated in a solid and the quantum coupling between the NCs can be varied by control over the NC surface chemistry, NC solids form a material platform with considerable tunability and versatility. This platform is of great interest to address basic scientific questions in quantum transport and shows promises for future optoelectronics.[1–12]

In this field, solids that are formed by NC assembly followed by oriented attachment of the NCs constitute a special class, since oriented attachment results in atomically coherent systems and strong quantum coupling. Over the years, atomically coherent one-dimensional rods,[13,14] two-dimensional quantum wells,[15] and nearly three dimensional[16] nanostructured but atomically coherent systems have been reported. Since, due to the NC/NC epitaxy, the quantum coupling is strong, the energy level and band structure of these systems is determined by their overall dimensions. A remarkable class is 2D superstructures that show a silicene-type honeycomb structure: these systems retain the semiconductor band gap but the highest valence and lowest conduction bands show a linear dispersion near the K-points of the Brillouin zone. This would mean that at sufficiently low temperature and with precise control of the Fermi level at around the K-points, massless electrons (holes) may dominate the transport properties, as in graphene.[17]

However, before this type of physics can be explored, several challenges must be addressed: one must be able to prepare sufficiently large domains of honeycomb superlattices to incorporate them in an electrical device with suitable contacts and to change the Fermi-level in a controlled way by gating. Control over the band occupation also means that a decent knowledge on the presence of in-gap states is a prerequisite. Second, it will be required to cool down the entire transistor system (at a given position of the Fermi-level), without mechanical or electrical breakage.

Here, we start this endeavor by a room-temperature study of the band occupation and electron transport in silicene-type honeycomb structures prepared from PbSe NCs. We used a transistor device allowing to measure the electronic properties under electronic equilibrium, and terahertz (THz) spectroscopy to measure the transient behavior of photo-generated electrons and holes. This study is motivated by the fact that we recently were able to reproducibly fabricate extended (> 100 µm) domains of PbSe honeycomb structures by nanocrystal assembly and oriented attachment.[18] We show that we can incorporate wet-chemically prepared superstructures as individual silicene sheets in an electrolyte gated device. We can change the Fermi level in a controlled way and occupy the lowest conduction band with up to 4 electrons, without interference of mid-gap electron traps. By moving the Fermi level to lower energies towards the valence band, holes are injected. They might either occupy the valence band or mainly trap states in the gap. The electron mobility measured in the transistor type device (about 1.5 ± 0.5 $cm^2V^{-1}s^{-1}$) compares well with that obtained by THz spectroscopy. The frequency-dependent THz results indicate that the room temperature electron mobility is not limited by electron scattering on lattice phonons, but mostly by lattice imperfections.

5.2 Formation of 2D honeycomb superlattices of PbSe

We prepared 2D honeycomb superlattices from PbSe NCs (with the size of 6.15 ± 0.4 nm) dispersed in toluene by self-assembly at the toluene-nitrogen interface and oriented attachment (see Appendix A5.1).[18] An atomically coherent silicene-type honeycomb structure is formed by epitaxial attachment of the PbSe NCs *via* 3 of their 6 {100} facets. A part of such a honeycomb structure is shown in Figure 5.1a. The Fourier transform of the image in the inset shows that the honeycomb periodicity holds for the entire image and is thus long ranged. We remark here that, due to the epitaxial connection, the quantum

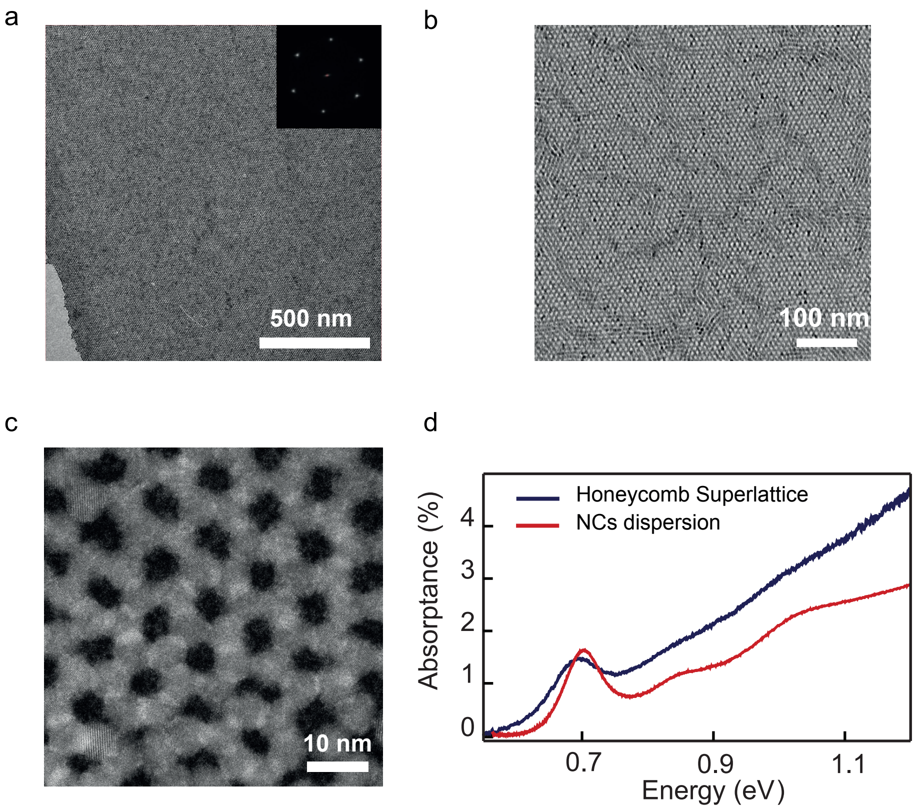

Figure 5.1. Structural properties of the PbSe honeycomb superlattice studied here. (a) TEM overview of a PbSe superlattice with honeycomb nanogeometry; the inset is the Fourier transform of the image showing that the honeycomb periodicity is long ranged and holds for the entire image. (b) TEM image of a superlattice with smaller honeycomb domains connected by slightly disordered grain boundaries. (c) High resolution HAADF-STEM image showing several types of NC misalignment in the honeycomb structure. (d) Absorption spectrum of a single-layer honeycomb superlattice deposited on a quartz substrate compared to that of dispersed NCs. The first excitonic absorption feature of the PbSe superlattice shows a red shift and broadening, compared to the NCs in dispersion. For the honeycomb superlattice monolayer on a quartz substrate, the absorption is 1.5 % at a photon energy of 0.7 eV. The absorption of NC dispersion is scaled down for comparison to the superlattice.

coupling between the NCs is strong. Atomic tight binding (TB) calculations have shown that this coupling results in mini-band formation with a band width in 0.1 eV range.[19] This means that, for ideal honeycomb structures, high mobility values only limited by phonon scattering are expected. On the other hand, disorder could also limit carrier transport. Several types of disorder have been observed and detailed in a recent work:[18] non-perfect epitaxial connections between the NCs is probably the most important origin of crystallographic disorder. In the experiments described here, the PbSe superstructures also showed slightly more disordered regions between the honeycomb domains (Figure 5.1b). Disorder due to the nanocrystal misalignment in the lattice is obvious from Figure 5.1c.

5.3 Light absorption by a PbSe honeycomb monolayer

The optical absorption spectrum of the NCs dispersed in tetrachloroethylene exhibits a peak at 0.7 eV related to the first exciton transition (Figure 5.1d). For a single PbSe honeycomb layer, the first feature is broadened such that it almost looks as a step, and it is also red shifted. Similar features have been observed for the square superlattices.[20] The broadening is due to quantum coupling between the PbSe NCs, ultimately resulting in mini-bands (see also below).[3,20,21] The red shift has been attributed to the effect of the dielectric environment.[3,20] The band structure obtained from a TB calculation is presented in Figure A5.2 without inclusion of many-body electron-hole interaction effects, which are probably weak, due to the large dielectric constant of PbSe. The calculated band structure yields an effective mass of 0.21 m_0 for electrons (m_0 being the free electron mass). We should remark here that models for 2D quantum wells predict a value of the absorptance of 2.3 % (related to the fine structure constant) for a single quantum well. The value that we measure is 1.5 %, about half the predicted value for a single free standing layer. A similar reduction of absorption of a 2D monolayer has been observed previously and was attributed to the presence of the quartz substrate (see Chapter 3).[22]

5.4 Transport measurements in an electrolyte-gated transistor.

Single sheets of a honeycomb superlattice were incorporated into a transistor-type device by horizontal transfer of the structure from the ethylene glycol (EG) surface on which it was formed (see Methods). The surface of the sample is treated by $PbCl_2$, in an attempt to passivate the surface traps. Using electrochemical gating, the number of conduction electrons in the honeycomb superlattice can be controlled. From the source-drain conductance and the electrode-gap geometry, the electron conductivity and, finally, the electron mobility can be obtained.[20]

In order to investigate the occupation of the bands with electrons (holes), differential capacitance measurements were performed (see Methods). Figure 5.2a shows the differential capacitance characterizing the injection of electrons and holes into the PbSe honeycomb superlattice treated with $PbCl_2$. It can be seen that electron injection sets on at -0.4 V (*versus* Ag, reference electrode) and increases gradually up to a sample potential of -1.2 V. The shapes of the forward and backward scans are similar but not entirely identical. It means that the charge injection is not entirely electrochemically reversible and some minor side reactions, such as the reduction of residual molecular oxygen, may be ongoing. At positive potentials, the differential capacitance rises, showing that positive charge carriers are injected into the PbSe superstructure.

The total amount of injected charge carriers and the number of carriers per NC site (≡1/2 unit cell) in the forward scan is depicted in Figure 5.2b. The method to determine this number is outlined in the Appendix A5.4. At the most negative potential (-1.2 V), we observed 4 electrons per NC site, meaning that the 8-fold degenerate S-type conduction band is, in principle, half occupied. We should mention here that the uncertainty in the occupation number is relatively large due to the uncertainty in the effective active area of the device (see details in Appendix A5.4). Also note that at room temperature, electrons can be thermally excited from the S-type mini-band into the P-type mini-band.

At sample potentials more negative than -0.5 V, the source-drain transport current increased linearly with the source-drain bias (see Figure A5.5); the slope provides the conductance of the superlattice. From the conductance and the geometry of the interdigitated source-drain electrodes and gap, the electronic conductivity was calculated. We have plotted the conductivity of the sample as a function of the sample potential on a linear scale (Figure 5.2c) and a logarithmic scale (Figure 5.2d) for convenience. As can be observed in Figure 5.2c, the conductivity sets on at around -0.5 V and rises steeply with the electrochemical potential, up to 1100 S/m at the most negative potential. For positive electrochemical

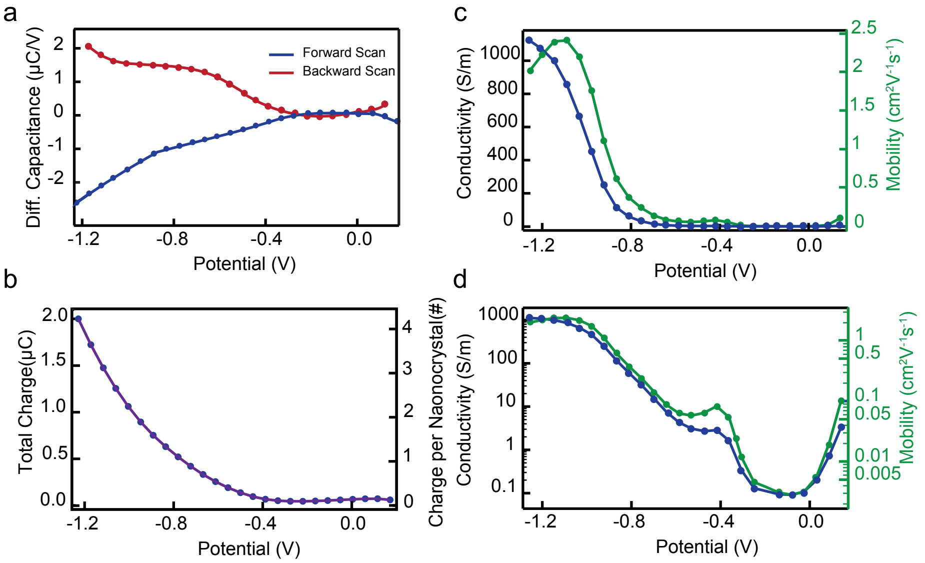

Figure 5.2. Electron injection and electron transport characteristics in a passivated PbSe honeycomb superstructure incorporated in an electrolyte gated transistor. (a) Differential capacitance of a passivated PbSe honeycomb superlattice measured in forward (from 0.2 to -1.2 V) and backward scan. (b) The total injected charge and the charge per NC site as measured in the forward scan. (c) The conductivity (blue) and the electron mobility (green) of the superlattice obtained from the source-drain conductance (See FigureA5.5), the geometry of the source-gap-drain fingers system and the charge density presented as a function of the electrochemical potential. (d) The conductivity (blue) and the electron mobility (green) of the superlattice in logarithmic scale.

potentials the differential capacitance increases again, this is accompanied with a small increase of the source-drain conductance (Figure 5.2d). It appears that the conductivity at positive potential is much smaller than the electron conductivity. This indicates that the injected positive charges to the superlattice might either occupy the valence band, or could occupy localized in-gap states. In the logarithmic scale in Figure 5.2d, the conductivity shows a step-like peak (not clearly visible on a linear scale) at a potential of -0.4 V. However, the charge density at this potential has a very small value. Therefore, we cannot conclude whether this peak is real and related to the band occupation of the superlattice.

Results obtained with other samples, also a sample that is not treated with $PbCl_2$, are provided in the Appendix A5.6. Similar results are obtained for those samples; *i.e.* the onset of the conductivity close to the onset of electron injection, the number of electrons in the conduction band varying between 4 and 8 per nanocrystal site, and a smaller conductance at positive potentials at which holes either occupy the valence band or trap states.

The electron mobility of the sample of Figure 5.2 calculated from the electron density and conductivity reached a maximum value of 2.3 $cm^2V^{-1}s^{-1}$ at -1 V. We performed differential capacitance and conductivity measurement on three other PbSe honeycomb devices. On average, we find an electron mobility of 1.5 ± 0.5 $cm^2V^{-1}s^{-1}$ in the PbSe honeycomb superlattices in the potential window of $-1.05 < V < -0.75$. The mobility of the non-treated sample has a value of 0.4 $cm^2V^{-1}s^{-1}$ (see Figure A5.6). Since these measurements could only be performed on a limited number of samples, we do not want to draw conclusions on the effect of $PbCl_2$ treatment on the electron mobility.

We further note that at the most negative potentials the conductivity is probably limited by the contact resistance between the honeycomb superlattice and the gold source and drain contacts. This may explain why the conductivity levels off and why the derived value of the mobility even decreases. Hence the values obtained here are a lower limit to the intrinsic dc mobility.

5.5 Terahertz photoconductivity spectroscopy

The THz photoconductivity was studied by photoexciting PbSe honeycomb superlattices treated by $PbCl_2$ with 50 fs laser pulses at a photon energy of 1.55 eV. The experimental procedure involves detection of charges and excitons with a single-cycle THz field and is identical to that described previously.[23,24] In general, photoexcitation of a semiconductor leads to formation of free mobile charges that can coexist with bound e-h pairs in the form of neutral excitons.[25–27] Free mobile charges and neutral excitons both contribute to the THz conductivity to an extent that is different for the real and imaginary parts.[28,29] At higher photoexcitation density recombination of free charges into excitons is more likely and consequently the quantum yield of charges decreases. If excitons co-exist with free charges in the honeycomb superlattice the relative magnitude of the real and imaginary THz conductivity should depend on the initial photoexcitation density and the decay kinetics of the real and imaginary parts should be different. Since the normalized decay of the real and imaginary parts are identical (see Figure A5.8) it can be inferred that the contribution of excitons is negligible and the initial quantum yield of charges can be taken equal to 1. The real part (positive sign) of the THz conductivity is due to the in-phase charge velocity in the probing THz field, and the imaginary part (negative sign) is due to the out-of-phase charge velocity.[30–32] The electrolyte gated transistor measurements have shown that holes might mostly occupy localized in-gap states. Therefore that the mobility of holes can be neglected and the THz conductivity can be described as being due to electrons only.

Figure 5.3 shows the product of the time-dependent quantum yield of electrons and their mobility: defined $S(t) = \phi_e(t)\mu_e$ with the initial quantum yield $\phi_e(t = 0) = 1$, as discussed above. The results in Figure 5.3 were obtained for an excitation density of 2.5×10^{13} cm^{-2}, which corresponds to 10 electron-hole (e-h) pairs per nanocrystal (NC) (see Methods). The signal S(t) reaches a maximum value of 2.1 ± 0.4 cm^{2}V^{-1}s^{-1} at a pump-probe delay time of 1.5 ps, which reflects the pulse duration of the probing single-cycle THz field. This value of S(t) is attributed to relaxed charge carriers at the band edge, since for a photoexcitation energy of 1.55 eV initially hot e-h pairs in PbSe NCs cool down to the band edge within a picosecond.[33,34] The electrons are seen to decay *via* trapping or recombination with a lifetime for half decay of ~ 10 ps. Similar results were obtained for lower (0.8×10^{13} cm^{-2}) and higher (2.5×10^{13} cm^{-2}) excitation densities (see Figure A5.7), which implies that higher-order recombination is not important for these densities.

To understand the charge transport mechanism, we plot in Figure 5.3b the frequency dependent electron mobility obtained by averaging S(t) over a pump-probe delay time interval of 2-6 ps. The increase of the mobility in Figure 5.3b with frequency ω and the negative imaginary mobility disagree with the simple Drude model.[30] The THz mobility is described by the Drude-Smith model, yielding:[35]

$$\mu(\omega) = \frac{e\tau}{m^*(1 - i\omega\tau)}\left(1 + \frac{c}{1 - i\omega\tau}\right) \qquad \text{(Eq. 5.1)}$$

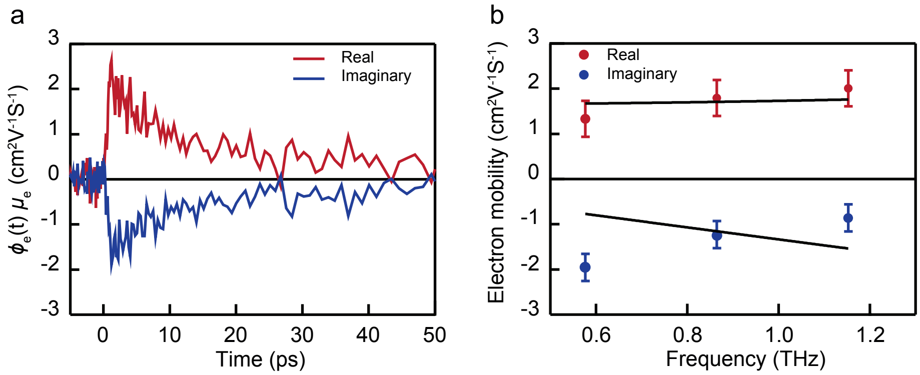

Figure 5.3. Terahertz photoconductivity obtained by photoexciting the PbSe honeycomb superlattice at photon energy of 1.55 eV. (a) Real (positive signal) and imaginary part (negative signal) of the quantum yield weighted mobility as a function of time obtained at excitation density 2.5×10^{13} cm^{-2}, which corresponds to 10 electron-hole pairs per NC. (b) Experimental frequency dependent charge carrier mobility (markers) together with fit of the Drude-Smith model to the data.

with e the elementary charge, τ the scattering time, m^* the effective mass, and c = <cosθ> a persistence of velocity parameter accounting for elastic backscattering with θ the scattering angle.

Solving for the real and imaginary parts of the Drude-Smith model yields:

$$\mu_{real}(\omega) = \frac{e\tau}{m^*(1+\omega^2\tau^2)}\left(1+\frac{c(1-\omega^2\tau^2)}{1+\omega^2\tau^2}\right) \quad \text{(Eq. 5.2)}$$

$$\mu_{imag}(\omega) = \frac{e\omega\tau^2}{m^*(1+\omega^2\tau^2)}\left(1+\frac{2c}{1+\omega^2\tau^2}\right) \quad \text{(Eq. 5.3)}$$

Taking the value of $m^* = 0.21\ m_0$, from atomistic tight binding (see Figure 5.4), and fitting expressions 5.2 and 5.3 to the frequency dependent mobility in Figure 5.3b yields τ = 5.2 ± 0.6 fs and c = -0.96 ± 0.01. At lower excitation densities we obtain similar values for τ and c (see Figure A5.9), which indicates that for the densities studied band filling does not affect the THz mobility. The backscattering parameter c close to -1 implies significant backscattering of the charges, which is typical for NC solids.[36,37] The DC mobility obtained from the Drude-Smith fit parameters is 1.7 $cm^2V^{-1}s^{-1}$, which is close to the value of 1.5 ± 0.5 $cm^2V^{-1}s^{-1}$ obtained from the transistor measurements described above. Hence, although the coupling between the NCs in the honeycomb structure is considerable, the electron mobility is strongly limited by scattering at imperfections.

The Drude-Smith fit reproduces the measured real part of the THz mobility, while it does not agree very well with the measured imaginary part. Structural disorder may cause the site-energy of a charge to vary on going from one NC to another. The disorder in the site-energies is roughly equal to the width of the first optical absorption peak of the NCs, which is about 0.1 eV, see Figure 5.1d. Such disorder is not included in the Drude-Smith model, which may cause the model to be inaccurate for the current material. A more detailed model of charge transport should include effects of disorder, however, that is beyond the scope of this study.

5.6 Discussion

We have studied electron transport in single sheets of PbSe with a silicene-type honeycomb geometry. In an ideal case, these structures are atomically coherent: the <111> axis of PbSe rock salt is perpendicular to the plane of the sheet. Each nanocrystal unit is epitaxially connected to three other ones, forming [100]/[100] connections. Silicene honeycomb structures of PbSe, very similar to the ones used here, have been structurally characterized in detail in a recent work.[18] It has been shown that while the honeycomb domains are very large (> 10 µm), there are several types of crystallographic defects, mostly related to non-ideal [100]/[100] connections between the constituting NCs. Our electrolyte-gated transport measurements show that the injected electrons occupy the lowest conduction band. However, the injected holes might either occupy the valence band or localized in-gap states. The similarity between the mobility obtained with an electrochemically gated transistor type device and the THz mobility is remarkable (both values are about 1.5 $cm^2V^{-1}s^{-1}$). This indicates that the quantum yield for charge carrier photo-generation in the terahertz experiments is close to unity, and also that mainly electrons contribute to the THz conductivity. From the above, it is thus reasonable to state that the electron mobility at room temperature is close to 1.5 cm^{2}V^{-1}s^{-1}.

Here we provide an interpretation of this result, using the band structure calculated for a PbSe silicene-type honeycomb structure with the same size of the honeycomb units (NCs) and periodicity. The lowest conduction bands calculated with atomistic tight-binding theory are shown in Figure 5.4. The lowest conduction band is 8-fold degenerate (including spin). It shows a conventional parabolic dispersion at the Γ-point, and a linear Dirac-type dispersion at the K-points. When electrons are injected and the occupation is low, the (low-T) occupation is at the Γ-point. The effective mass of electrons, obtained from atomistic tight binding calculations is 0.21 m_0 (see Figure 5.4). It is instructive to compare the mobility observed in the honeycomb superstructures with that reported for bulk PbSe. The experimental value for macroscopic crystals of PbSe at room temperature is 1000 cm^{2}V^{-1}s^{-1}.[38] When we assume that the effective mass in bulk PbSe is 0.1 m_0,[39] the scattering time in a macroscopic PbSe crystal is calculated to be 60 fs, which is more than 10 times larger the value of 5.2 ± 0.6 fs we found for the honeycomb superlattice. For the PbSe superstructures, we find that the mobility is almost 500 times smaller than the bulk value, whereas the effective mass is only (here at the Γ-point) 2 times larger. This means that in our PbSe honeycomb superlattice the electron scattering time is considerably shorter than in the bulk PbSe; hence electrons do not only scatter at lattice phonons, but also at lattice imperfections. This is corroborated by the frequency dependence of the THz mobility. The real and imaginary parts cannot be described by the Drude model, which accounts only for electron-phonon scattering, but backscattering of electrons on defects needed to be included. The THz mobility could be reproduced approximately

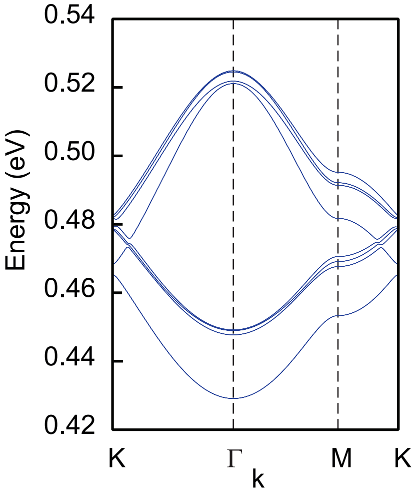

Figure 5.4. Tight binding (TB) of PbSe honeycomb superlattice. The lowest conduction bands calculated with atomistic tight-binding (TB) theory. The lowest conduction band is 8-fold degenerate (including spin); the degeneration is slightly broken due to quantum coupling of the 4 L points in the zone. The bands show a conventional parabolic dispersion at the Γ-point, and a linear Dirac-type dispersion at the K-points. The calculated band structure yields an effective mass of 0.21 m_0 for electrons (m_0 is the free electron mass).

by the Drude-Smith model with c = -0.96 ± 0.01, which implies strong backscattering of electrons at imperfections in the PbSe honeycomb superstructures. We believe that imperfect [100]/[100] connections between the NCs are the most important origin of disorder in the PbSe honeycomb superstructures.

5.7 Summary and outlook

We studied the electronic properties of PbSe honeycomb superstructures in a transistor type device and with THz spectroscopy. The results show that electrons occupy the lowest conduction band. The electron mobility is limited by lattice imperfections. The electronic characterization at room-temperature presented here shows that it should be possible to subtly move the Fermi level through the energy range of the conduction mini-band. Once PbSe honeycomb transistor-type devices can be cooled down to cryogenic temperatures (*i.e.* k_BT << band width), it should be possible to study the transport physics with the Fermi level positioned in a narrow energy window, *e.g.* to distinguish the Γ point from K-points. Eventually, this research would enable to display the Dirac character of the carriers in the energy region around the K-points, as has been predicted by simple and advanced theories.

5.8 Methods

Chemicals

Lead acetate trihydrate (99.99 %, Sigma-Aldrich), oleic acid (90 %, Sigma-Aldrich), 1-octadecene (90 %, Sigma-Aldrich), selenium powder (99.99 %, Alfa Aesar), trioctylphosphine (90 %, Sigma-Aldrich), diphenylphospine (98 %, Sigma-Aldrich), 1-butanol (99.8 % anhydrous, Sigma-Aldrich), methanol (99.8 % anhydrous, Sigma-Aldrich), toluene (99.8 % anhydrous, Sigma-Aldrich), ethylene glycol (99.8 %, anhydrous, Sigma-Aldrich), acetonitrile (99.8 % anhydrous, Sigma-Aldrich), lithium perchlorate (99.99 %, Sigma-Aldrich), lead(II) chloride (99.99 %, Sigma-Aldrich).

PbSe NCs synthesis

PbSe QDs were synthesized based on the methodology of Steckel *et al.* method.[40] For the lead precursor, a mixture of 4.77 g lead acetate, 10.35 g oleic acid and 39.75 g 1-octadecene was heated at 120 °C under vacuum for 5 hours. For the selenium precursor, a mixture of 3.52 g selenium powder, 46.59 mL trioctylphosphine and 0.41 mL diphenylphospine were prepared by dissolving selenium. Subsequently, 10.25 mL of the lead containing solution was heated upto 180 °C and 7.5 mL of the selenium precursor was injected. The mixture was kept at 150 °C for 70 second and the NC growth was quenched with 30 mL of a methanol/butanol mixture (1:2). The NC product solution was centrifuged and the NCs were dissolved in toluene. This concentrated suspension of PbSe NCs was washed twice more with methanol and the NCs were dissolved in toluene.

The formation of honeycomb superstructure by means of oriented attachment

Honeycomb superlattices were obtained by the NCs assembly at the toluene-nitrogen interface followed by oriented attachment. We followed an ultra-slow procedure that has been developed recently in our group (Figure A5.1). A small petri dish was filled with ethylene glycol as a liquid substrate. This dish was placed in a bigger petri dish that also contained toluene. A certain volume of PbSe NC dispersion in toluene was drop casted on top of ethylene glycol. A beaker was placed on top of the petri dishes to slow down the toluene evaporation. The evaporation of the toluene solvent and the superlattice formation was really slow and took around 16 hours. The honeycomb monolayer was transferred onto a TEM grid for structural characterization, quartz substrates for THz measurement and a device with microstructured gold electrodes, *i.e.* source and drain, separated by a gap for electrolyte gating and transport measurements (details in Appendix A5.3). The formation of PbSe honeycomb superlattices and their transport to a TEM grid, the quartz substrate and a transport device were performed in a glove box.

Surface treatment by $PbCl_2$

In an attempt to passivate the surface traps, the surface of the honeycomb superlattices was treated by $PbCl_2$. For this purpose, a saturated dilution of $PbCl_2$ in methanol was prepared. The substrates with the superlattices were immersed shortly into the $PbCl_2$ dilution and then into methanol, to remove the residuals.

Electron injection and transport measurement in an electrolyte gated transistor

Electrochemical gating is a well-stablished methods used to investigate the transport properties of 2D superlattices. The device used for this measurement consists of interdigitated source and drain electrodes, on top of a SiO_2 substrate (details in Appendix A5.4). In this experiment we used acetonitrile containing a Li^+ salt as an electrolyte. An Ag wire and a Pt sheet were inserted into the electrolyte for reference and counter electrodes, respectively. The Fermi level of the superlattices moved towards the conduction band (valence band) by applying negative (positive) potential with respect to the reference electrode by using a potentiostat. To investigate the charge injection into the honeycomb superlattice, differential capacitance measurements were performed. By applying the potential in small steps of 55 mV, the current in an interval time was measured. The integration of the current gave us the total amount of charge injected to the structure. For measurement of the sample conductance at a given potential, a small potential was applied between source and drain electrodes and the source-drain current was measured. As soon as the Fermi level was in the conduction band, the source-drain resistance was ohmic. The conductivity was obtained from the measured conductance the geometry of the electrodes. Eventually, the electron mobility was obtained from the conductivity and the electron density (details in Appendix A5.3).

Terahertz conductivity measurements

The honeycomb superlattice was photoexcited by optical pulses with photon energy 1.55 eV. The photoconductivity was probed by single-cycle THz pulses analogous to our previous work.[23,24] According to the thin film approximation the quantum yield weighted complex mobility $\phi_e(t)\ \mu_e + \phi_h\ (t)\ \mu_h$ is related to the differential THz signal $\Delta E\ (\omega,t)$ by:[31,32]

$$\phi_e(t)\mu_e + \phi_h(t)\mu_h = \frac{\Delta E(\omega,t)}{E_0(\omega)}\frac{(1+n_s)c\varepsilon_0}{eN_a} \qquad \text{(Eq. 5.4)}$$

with e the elementary charge, c the speed of light in vacuum, ε_0 the relative permittivity of free space, n_s the refractive index of the quartz substrate, N_a the number of absorbed photons per unit area (excitation density).

The initial number of e-h pairs per NC was obtained as the ratio of the excitation density and the number of NCs per unit area, with the latter determined to be 2.6×10^{12} NCs per cm^2 from analysis of a TEM image of the honeycomb superlattice.

References

1. Talapin, D. V. & Murray, C. B. Supporting Online Material for PbSe Nanocrystal Solids for n-and p-Channel Thin Film Field-Effect Transistors. *Science* **310**, 86–90 (2005).
2. Vanmaekelbergh, D. & Liljeroth, P. Electron-conducting quantum dot solids: Novel materials based on colloidal semiconductor nanocrystals. *Chem. Soc. Rev.* **34**, 299–312 (2005).
3. Sandeep, C. S. S. *et al.* Epitaxially connected PbSe quantum-dot films: Controlled neck formation and optoelectronic properties. *ACS Nano* **8**, 11499–11511 (2014).
4. Talapin, D. V., Lee, J. S., Kovalenko, M. V. & Shevchenko, E. V. Prospects of Colloidal Nanocrystals for Electronic and Optoelectronic Applications. *Chem. Rev.* **110**, 389–458 (2010).
5. Law, M. *et al.* Structural, optical, and electrical properties of PbSe nanocrystal solids treated thermally or with simple amines. *J. Am. Chem. Soc.* **130**, 5974–5985 (2008).
6. Oh, S. J. *et al.* Engineering charge injection and charge transport for high performance PbSe nanocrystal thin film devices and circuits. *Nano Lett.* **14**, 6210–6216 (2014).

7. Oh, S. J. *et al.* Stoichiometric control of lead chalcogenide nanocrystal solids to enhance their electronic and optoelectronic device performance. *ACS Nano* **7**, 2413–2421 (2013).
8. Chiu, S. C., Jhang, J. S., Chen, J. F., Fang, J. & Jian, W. Bin. Effects of cross-sectional area on the tunneling-junction array in octahedral PbSe colloidal-nanocrystal solids. *Phys. Chem. Chem. Phys.* **15**, 16127–16131 (2013).
9. Luther, J. M. *et al.* 001-Schottky solar cells based on colloidal nanocrystal films. *Nano Lett.* **8**, 3488–3492 (2008).
10. Gao, Y. *et al.* Photoconductivity of PbSe quantum-dot solids: Dependence on ligand anchor group and length. *ACS Nano* **6**, 9606–9614 (2012).
11. Kang, M. S., Lee, J., Norris, D. J. & Daniel Frisbie, C. High carrier densities achieved at low voltages in ambipolar PbSe nanocrystal thin-film transistors. *Nano Lett.* **9**, 3848–3852 (2009).
12. Baumgardner, W. J., Whitham, K. & Hanrath, T. Confined-but-connected quantum solids via controlled ligand displacement. *Nano Lett.* **13**, 3225–3231 (2013).
13. Koh, W. K., Bartnik, A. C., Wise, F. W. & Murray, C. B. Synthesis of monodisperse PbSe nanorods: A case for oriented attachment. *J. Am. Chem. Soc.* **132**, 3909–3913 (2010).
14. Cho, K. S., Talapin, D. V., Gaschler, W. & Murray, C. B. Designing PbSe nanowires and nanorings through oriented attachment of nanoparticles. *J. Am. Chem. Soc.* **127**, 7140–7147 (2005).
15. Schliehe, C. *et al.* Ultrathin PbS sheets by two-dimensional oriented attachment. *Science* **329**, 550–553 (2010).
16. Whitham, K. & Hanrath, T. Formation of Epitaxially Connected Quantum Dot Solids: Nucleation and Coherent Phase Transition. *J. Phys. Chem. Lett.* **8**, 2623–2628 (2017).
17. Neto, A. H. C., Guinea, F., Peres, N. M. R., Novoselov, K. S. & Geim, A. K. The electronic properties of graphene. *Rev. Mod. Phys.* **81**, 110-162 (2009).
18. Peters, J. L. *et al.* Mono- and Multilayer Silicene-Type Honeycomb Lattices by Oriented Attachment of PbSe Nanocrystals: Synthesis, Structural Characterization, and Analysis of the Disorder. *Chem. Mater.* **30**, 4831–4837 (2018).
19. Kalesaki, E. *et al.* Dirac cones, topological edge states, and nontrivial flat bands in two-dimensional semiconductors with a honeycomb nanogeometry. *Phys. Rev. X* **4**, 1–12 (2014).
20. Alimoradi Jazi, M. *et al.* Transport Properties of a Two-Dimensional PbSe Square Superstructure in an Electrolyte-Gated Transistor. *Nano Lett.* **17**, 5238–5243 (2017).
21. Wolcott, A. *et al.* Anomalously large polarization effect responsible for excitonic red shifts in PbSe quantum dot solids. *J. Phys. Chem. Lett.* **2**, 795–800 (2011).
22. Fang, H. *et al.* Quantum of optical absorption in two-dimensional semiconductors. *Proc. Natl. Acad. Sci.* **110**, 11688–11691 (2013).
23. Evers, W. H. *et al.* High charge mobility in two-dimensional percolative networks of PbSe quantum dots connected by atomic bonds. *Nat. Commun.* **6**, 1–8 (2015).
24. Kulkarni, A. *et al.* Efficient Steplike Carrier Multiplication in Percolative Networks of Epitaxially Connected PbSe Nanocrystals. *ACS Nano* **12**, 378–384 (2018).

25. Kaindl, R. A., Hägele, D., Carnahan, M. A. & Chemla, D. S. Transient terahertz spectroscopy of excitons and unbound carriers in quasi-two-dimensional electron-hole gases. *Phys. Rev. B* **79**, 1–13 (2009).

26. Ambigapathy, R. *et al.* Coulomb correlation and band gap renormalization at high carrier densities in quantum wires. *Phys. Rev. Lett.* **78**, 3579–3582 (1997).

27. Hangleiter, A. *et al.* Efficient formation of excitons in a dense electron-hole plasma at room temperature. *Phys. Rev. B* **92**, 1–5 (2015).

28. Lauth, J. *et al.* Photogeneration and Mobility of Charge Carriers in Atomically Thin Colloidal InSe Nanosheets Probed by Ultrafast Terahertz Spectroscopy. *J. Phys. Chem. Lett.* **7**, 4191–4196 (2016).

29. Lauth, J., Kinge, S. & Siebbeles, L. D. A. Ultrafast Transient Absorption and Terahertz Spectroscopy as Tools to Probe Photoexcited States and Dynamics in Colloidal 2D Nanostructures. *Zeitschrift für Phys. Chemie* **231**, 107–119 (2017).

30. Ulbricht, R., Hendry, E., Shan, J., Heinz, T. F. & Bonn, M. Carrier dynamics in semiconductors studied with time-resolved terahertz spectroscopy. *Rev. Mod. Phys.* **83**, 543–586 (2011).

31. Joyce, H. J., Baig, S. A. & Parkinson, P. A review of the electrical properties of semiconductor nanowires: insights gained from terahertz conductivity spectroscopy: The influence of surfaces on the transient terahertz conductivity and electron mobility of GaAs nanowires. *Semicond. Sci. Technol* **31**, (2016).

32. Lloyd-Hughes, J. & Jeon, T. I. A review of the terahertz conductivity of bulk and nano-materials. *J. Infrared, Millimeter, Terahertz Waves* **33**, 871–925 (2012).

33. Spoor, F. C. M. *et al.* Hole cooling is much faster than electron cooling in pbse quantum dots. *ACS Nano* **10**, 695–703 (2016).

34. Spoor, F. C. M., Tomić, S., Houtepen, A. J. & Siebbeles, L. D. A. Broadband Cooling Spectra of Hot Electrons and Holes in PbSe Quantum Dots. *ACS Nano* **11**, 6286–6294 (2017).

35. Smith, N. V. Classical generalization of the Drude formula for the optical conductivity. *Phys. Rev. B* **64**, (2001).

36. Bergren, M. R. *et al.* Ultrafast electrical measurements of isolated silicon nanowires and nanocrystals. *J. Phys. Chem. Lett.* **5**, 2050–2057 (2014).

37. Beard, M. C. *et al.* Electronic Coupling in InP Nanoparticle Arrays. *Nano Lett.* **3**, 1695–1699 (2003).

38. Kittel, C. Introduction to Solid State Physics. (*New York, John Willey and Sons*, 2004).

39. Kang, I. & Wise, F. W. Electronic structure and optical properties of PbS and PbSe quantum dots. *J. Opt. Soc. Am. B* **14**, 1632 (1997).

40. Steckel, J. S., Yen, B. K. H., Oertel, D. C. & Bawendi, M. G. On the mechanism of lead chalcogenide nanocrystal formation. *J. Am. Chem. Soc.* **128**, 13032–13033 (2006).

Appendix

A5.1 Oriented attachment

The oriented attachment of PbSe QDs to form honeycomb superlattices were performed following our recent slow process.[18] A dispersion of 2 µL of PbSe QDs (with concentration of 1.56×10^{-5} M) in 800 µL toluene was prepared (Figure A5.1 a). A 6.5 mL petri dish with 28 mm in diameter was filled with ethylene glycol and used as a liquid substrate. This dish was placed in a bigger petri dish containing 3 mL toluene (Figure A5.1b). 350 µL of PbSe QDs dispersion in toluene was drop casted on top of the ethylene glycol substrate. A beaker was placed on top of the petri dishes to slow down the toluene evaporation (Figure A5.1c). After 16 hours, the solvent was evaporated and the honeycomb superlattice formed on the liquid-nitrogen interface (Figure A5.1d). The monolayer of the superstructure was transferred onto quartz substrates for THz measurement and electrochemical golden fingered electrodes for electrochemical gating measurements (Figure A5.1e).

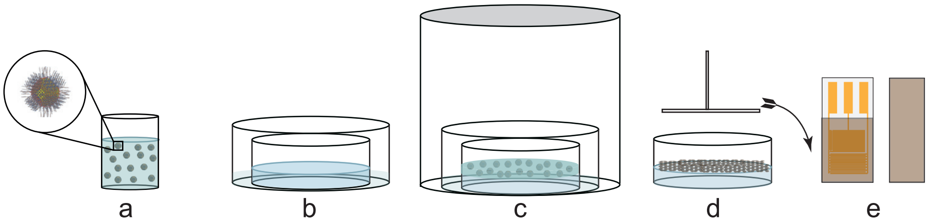

Figure A5.1. (a) Dilution of QDs in toluene, (b) 6.5 mL petri dish with ethylene glycol as substrate inside a bigger petri dish containing 2 mL toluene, (c) drop casted QDs on top of the EG substrate and covered with a 500 mL beaker to slow down the toluene evaporation, (d) formation of honeycomb superlattices and stamping the superstructure on the solid substrates and (e) covered quartz substrate and fingered electrode by a monolayer of the structure.

A5.2 Band structure of a honeycomb superstructure

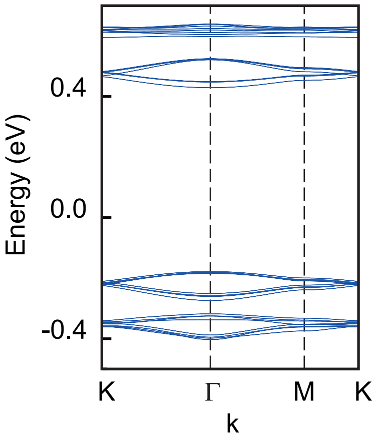

Figure A5.2. Conduction and valence band of a silicene-type PbSe honeycomb superlattice consisting of tangential spheres connected by cylinders.

A5.3. Electrode design for gating measurement

Figure A5.3 shows the electrode design used for electrochemical gating measurements. The gold figure pattern is created by optical lithography on a SiO_2 substrate. These interdigitated fingers are spaced 10 to 50 μm apart, with a total device length between 9 and 1200 mm.

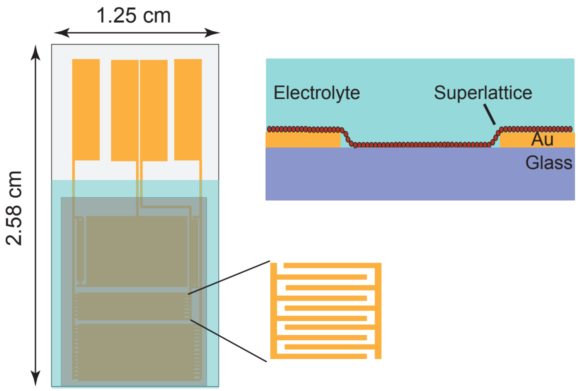

Figure A5.3. Electrode designs used for differential capacitance and conductivity measurements in an electrochemical gating setup.

A5.4. Conductivity & mobility for electrochemical gating measurements

To calculate the charge density, we integrated the differential capacitance giving us the total amount of charge injected to the superstructure. Next, we should know the number of nanocrystal in the gated area of the electrode. For this purpose, we visually checked the area of the electrode covered by superlattices. In addition, from the TEM images, we saw that not the whole area is covered by superstructure due to the empty places and cracks (Figure A5.4 a). For the sample presented in this work, we estimated that 70 % of the area is covered by the superlattices. To estimate the number of NCs in the covered area, we got an HAADF image and counted the number of presented NCs in the image which was equal to 34 (Figure A5.4 b). The area of the image was 1.6×10^{-15} nm^2. Therefore, the number of NCs in a cm^2 is equal to 2.2×10^{12}. Therefore, the number of charge per NC was:

$$N = \frac{\frac{Q}{e}}{0.7 \times A \times 2.2 \times 10^{12}} \qquad \text{(Eq. A5.1)}$$

Where N is the number of charge per nanocrystal, Q is total charge injected to the superlattice, e is elementary charge and A is the area of the electrode where the superstructure was stamped on.

From the source-drain current *versus* applied potential shown in figure A5.5, the conductance of the superstructure was determined. From the conductance and the fingers geometry, the conductivity of the superlattices was calculated:

$$\sigma = \frac{G \times w}{l \times h} \qquad \text{(Eq. A5.2)}$$

Where G is the conductance, w and l are the width and length of the fingers and h is the thickness of the honeycomb monolayer.

From the charge per NC and the conductivity, the mobility of the honeycomb superlattice was calculated:

$$\mu = \frac{\sigma}{e \times \frac{N}{V}} \qquad \text{(Eq. A5.3)}$$

Where V is the volume of a NC considered as sphere.

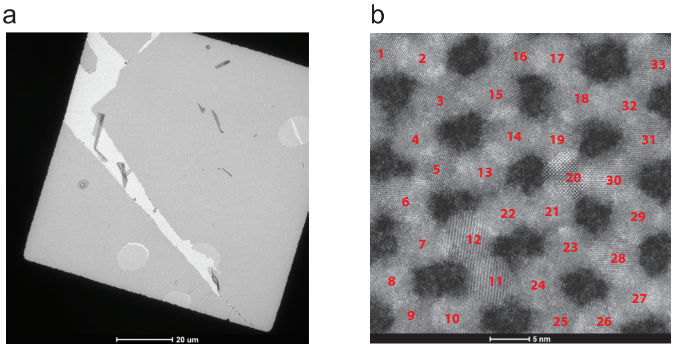

Figure A5.4. (a) Zoom out TEM image of the superstructure used to estimate the coverage of the sample on the electrode and (b) HAADF image of the honeycomb superlattice to estimate the number of NCs in a cm^2 area

A5.5. Source-drain current versus applied potential.

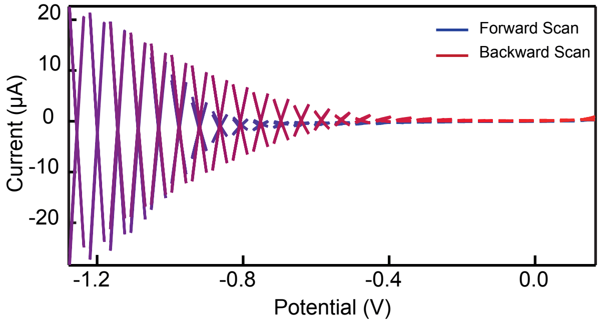

Figure A5.5. Source-drain current versus applied potential. In the forward scan when the potential is more negative than -0.7 V, the Fermi level is in the conduction band.

A5.6. Transport measurements in an electrolyte-gated transistor on a non-treated honeycomb sample

Figure A5.6a shows the differential capacitance characterizing the injection of electrons into the honeycomb superlattice; electron injection sets on at -0.4 V and rises gradually until a sample potential of -1.2 V. The shapes of the forward and backward scans are very similar showing that electron injection and extraction are reversible in this potential window. At positive potentials, the differential capacitance raises again, showing that positive charge carriers are injected into the PbSe superstructure.

The total amount of injected charge carriers and the number of carriers per NC site (= 1/2 unit cell) in the forward scan are depicted in Figure A5.6b. At the most negative potential (-1.2 V), we observed 8 electrons per NC site, meaning that the 8-fold degenerate S-type conduction band is, in principle, fully occupied.

As it can be observed in Figure A5.6c and A5.6d, the conductivity sets on at -0.4 V and rises with the electrochemical potential, up to 50 S/m at the most negative potential. The raise in the conductivity is pretty small for potentials more negative than -0.8 V, this is due to the fact for this device the interfacial PbSe superstructure/gold contact resistance starts to dominate over the resistance of the superstructure. The conductance onset agrees with the onset of the differential capacitance, showing that the injected electrons occupy conductive states only. While for electrochemical potentials positive of 0 V the differential capacitance increases again, this is not accompanied with an increase of the source-drain conductance. We conclude that positive charges are injected in the PbSe superstructure, but they occupy localized in-gap states.

The electron mobility of the PbSe honeycomb superstructure calculated from the electron density and conductivity reached the value of 0.4 cm^{2}V^{-1}s^{-1} at -0.8 V as it is shown in Figure A5.6c.

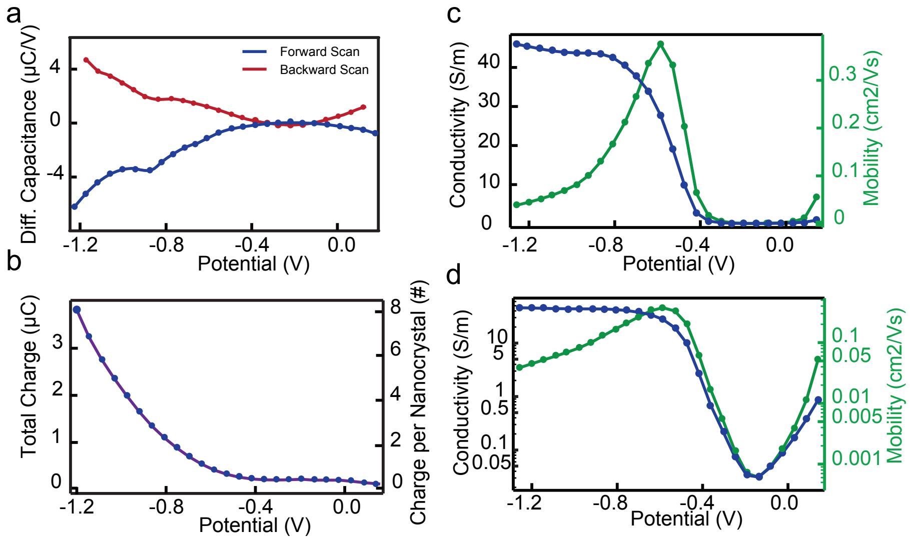

Figure A5.6. (a) Differential capacitance of a passivated PbSe honeycomb superlattice measured in forward (from 0.2 to -1.2 V) and backward scan. (b) The total injected charge and the charge per NC site as measured in the forward scan. (c) The conductivity (red) and the electron mobility (blue) of the superlattice obtained from the source-drain conductance, the geometry of the source-gap-drain fingers system and the charge density presented as a function of the electrochemical potential. (d) The conductivity (red) and the electron mobility (blue) of the superlattice in logarithmic scale.

A5.7 Terahertz conductivity data

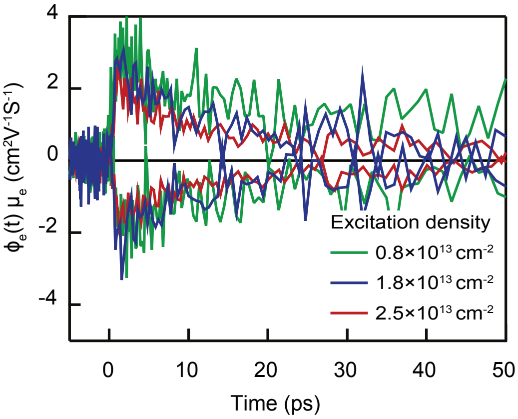

Figure A5.7. Product of quantum yield and mobility of electrons for excitation densities of 0.8×10^{13} cm^{-2}, 1.8×10^{13} cm^{-2}, and 2.5×10^{13} cm^{-2} which correspond to 3, 7, and 10 electron-hole pairs per NC, respectively.

A5.8 Normalized real and imaginary part of the THz conductivity at different excitation densities

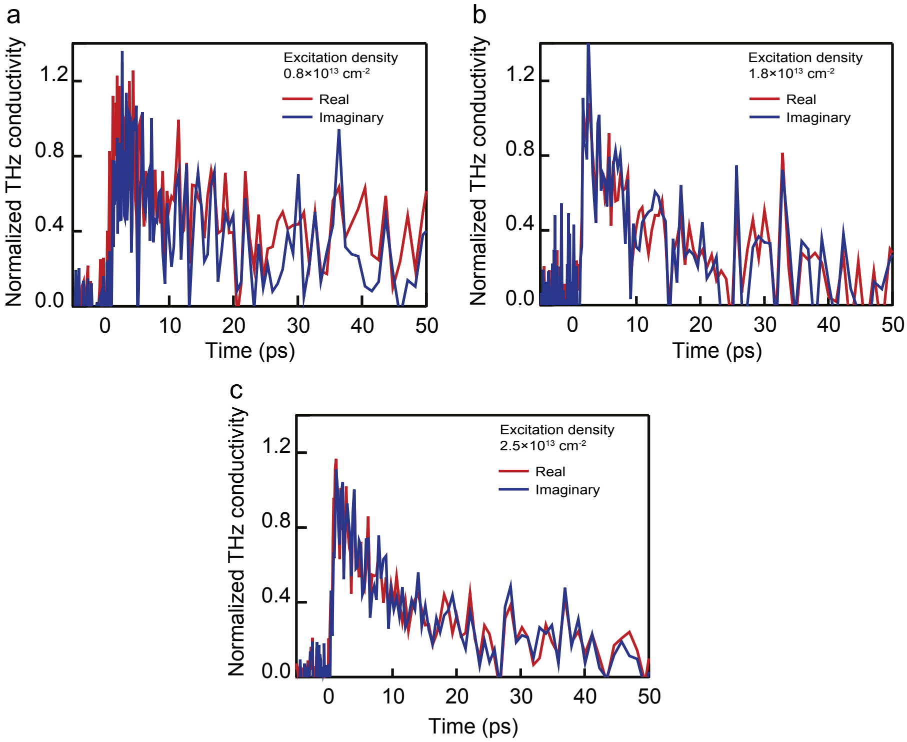

Figure A5.8. Normalized real and imaginary part of the THz conductivity at excitation densities (a) 0.8×10^{13} cm^{-2}, (b) 1.8×10^{13} cm^{-2}, and (c) 2.5×10^{13} cm^{-2}.

A5.9 Drude-Smith model fits to the frequency dependent electron mobility

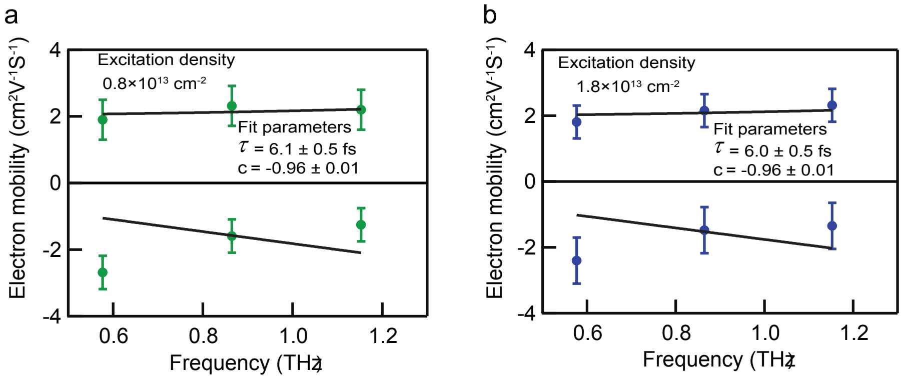

Figure A5.9. Drude-Smith model fits to the frequency dependent electron mobility for excitation densities of (a) 0.8×10^{13} cm^{-2}, and (b) 1.8×10^{13} cm^{-2}.

Chapter 6

Room-temperature band occupation and electron transport in CdSe superlattices with square and honeycomb geometry

Abstract

2D superlattices of lead- and cadmium-chalcogenide quantum dots with atomic connections between the nanocrystals form a novel class of materials for optoelectronic applications due to their unique band structure dictated by the geometry. Theoretical studies show that these 2D systems have distinct band structures with the appearance of Dirac cones in the case of the honeycomb lattice. Here, we present crystallographic characterization of CdSe superlattices obtained after Cd for Pb cation exchange. Our results show that most CdSe nanocrystals in the superlattices are crystallographically aligned and thus connected after the Cd for Pb cation exchange. The structural analysis indicates that the rock salt superlattices of PbSe are transformed to wurtzite/zinc blende core/shell in the CdSe superlattices. Furthermore, we investigate the band occupation and charge transport properties of these 2D CdSe superlattices. A monolayer of CdSe square and honeycomb superstructures is incorporated in a transistor type setup with electrolyte gating. The electron density is controlled by the gate potential. We observe that injected electrons occupy the conduction orbitals in the nanocrystals. The electron mobility at room temperature is found to be up to 10 $cm^2V^{-1}S^{-1}$ for the honeycomb superstructure.

6.1 Introduction

In recent years, self-assembled nanocrystal (NC) solids formed by close packed arrays of monodisperse semiconductor quantum dots (QDs) have been extensively investigated.[1–8] The individual NC building blocks of these arrays are separated by surface ligand molecules defining the charge tunneling barriers. The nature and length of the ligands determines the dot-to-dot tunneling rate and hence carrier mobility.[9,10] Chemical methods have been introduced to decrease the interdot separation by stripping or exchanging the long ligands for shorter ones, driving an evolution from low-mobility hopping transport to high-mobility band-like transport.[11–17] Furthermore, chemical treatment of NC solids can significantly improve the charge carrier mobility via surface trap passivation.[18–21] Lately, 2D square and honeycomb superlattice of Pb- and Cd-chalcogenide have been prepared.[22–24] In these structures, truncated cubes of QDs are epitaxially connected *via* their {100} facets. Therefore, the electronic coupling is much stronger compared to the NCs solids in which the NCs are separated by ligands molecules.[25] Theoretical studies show that these 2D systems have distinct band structures with the appearance of Dirac cones in the case of a honeycomb superstructure.[26,27] In Chapter 4 and 5, we reported the first study of electron transport in a 2D PbSe system with a square and honeycomb geometry. Electron mobilities between 1 and 18 $cm^2V^{-1}s^{-1}$ were observed for these superlattices. The terahertz measurement on PbSe honeycomb superlattices (Chapter 5) show a similar mobility as obtained with an electrochemically gated transistor type device. In addition, terahertz mobilities up to 250 $cm^2V^{-1}s^{-1}$ were measured by Evers *et al.* on 2D percolative networks of PbSe.[28]

Here, we transformed PbSe honeycomb and square superstructures into CdSe superlattices *via* a cation exchange reaction.[29,30] We performed an orientation mapping *via* a region-growing segmentation procedure on HAADF-STEM images to determine the deviation of each particle from a perfect crystallographic orientation. It is observed that all CdSe nanocrystals are crystallographically aligned and thus connected after the Cd for Pb cation exchange. However, there is a small misorientation between each nanocrystal. In addition, this procedure revealed that the rock salt square and honeycomb superlattices of PbSe NCs are transformed to wurtzite/zinc blende core/shell superlattices of CdSe. Furthermore, we show that the superlattices of CdSe nanocrystals can be incorporated as a monolayer in a transistor set-up with an electrolyte gate. The band occupation of the superlattices was monitored in detail by means of spectroelectrochemical differential absorption measurements. We found that electrons can be reversibly injected and extracted up to 2 electrons per nanocrystal site. The agreement between the onset of the conductivity and the average bleach of the $1S_{3/2}S_e$ transition demonstrates that the electrons occupying the conduction band are highly mobile. An electron mobility up to 10 $cm^2V^{-1}s^{-1}$ is obtained for CdSe honeycomb superlattices.

6.2 Structural characterization of a CdSe honeycomb structure

We prepared 2D square and honeycomb superlattices with the thickness of one nanocrystal (5.8 nm) by means of self-assembly followed by oriented attachment explained in the Methods section. Atomically coherent square and silicene-type honeycomb structures are formed by epitaxial attachment of the PbSe NCs *via* four and three of their 6 {100} facets, respectively. We transformed PbSe superstructures into CdSe superlattices *via*

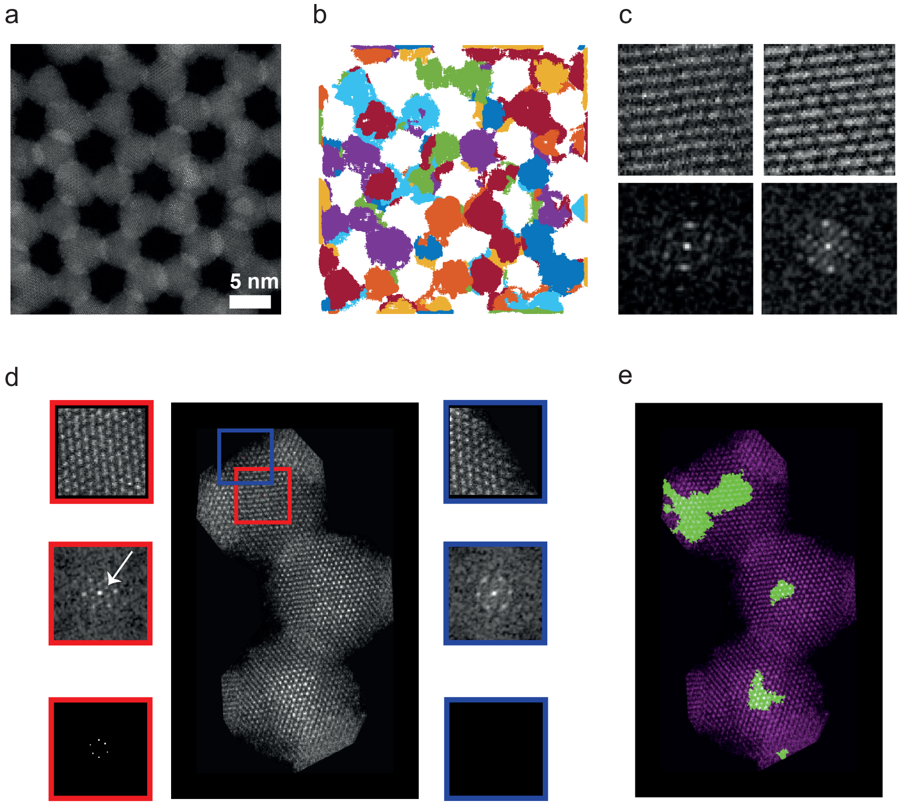

Figure 6.1. Structural characterization of a CdSe honeycomb structure. (a) HAADF-STEM image of a CdSe superlattice with honeycomb nanogeometry. (b) Regional map of the HAADF-STEM image obtained from region growing segmentation procedure (different colors identify slightly different orientations). It shows that most CdSe nanocrystals possess the same crystallographic orientation. (c) (Left) Different region of interest ROI of the real HAADF-STEM projection image accompanied by the power spectrum of its Fourier transform; (Right) Simulated HAADF-STEM projection image of the simulated structure accompanied by the power spectrum of its Fourier transform. (d) Two ROIs in the superlattices nanocrystals are compared. One in the center of the nanocrystal (red) and one at the edge (blue). For both ROIs we illustrate the power spectrum of its Fourier transform and the position of the maxima's within the inner ring. It is observed that for a given nanocrystal, extra (weak) reflections are present in the Fourier transforms of the middle part of the nanocrystal, indicated by white arrow, which are not present at the outer part. The zone axis for the outer and inner parts are the [111] of the CdSe zinc blende and [001] of the CdSe wurtzite structures, respectively. (e) Overlay between part of the HAADF-STEM projection image and regions with extra reflections (green) showing that the central parts have extra reflections, indication of a wurtzite region.

a cation exchange reaction (see Methods). In Chapter 3 (Figure A3.2), we show that the Energy Dispersive X-ray (EDX) Spectroscopy measurement confirms the (nearly) complete transformation of PbSe superstructure to CdSe (the detection limit is 0.5 %). Determination of the crystallographic orientation of regions of the superlattices as seen in a given atomic resolution STEM image (Figure 6.1a) is of great importance. For this purpose we designed a region-growing segmentation procedure where we compare the

Fast Fourier transformation (FFT) of a small region around each pixel to the FFT of its surroundings, to determine which areas are in the same orientation (for more detail see Methods). Figure 6.1b shows the regional map obtained from this procedure on the honeycomb STEM image in Figure 6.1a (different colors identifies slightly different orientation of the [111] axis). Due to noise and artefacts resulting from the sharp edges of the object, there are some discontinuities in the regional map. Figure 6.1 a-c indicates that the nanocrystals are oriented with the [111] axis upwards, with sharp but visible misorientation (as indicated by the different colors in Figure 6.1.b).

Given the structure symmetry is known, we can model it, and simulate projection images. In this way we can determine if the nanocrystals are in zone or not. If not we can estimate how much the nanocrystals are disorientated. This principle is illustrated in Figure 6.1c. On the left side we show a small region of interest of a CdSe nanocrystal, together with the power spectrum of its Fourier transform. On the right both the simulated HAADF-STEM projection image as the power spectrum of its Fourier transform are shown in case our predefined model was rotated 2 degrees out of zone. The good agreement shows that this methodology shows promise to determine the offset of every symmetric region found in Figure 6.1b.

By looking carefully at the atomic resolution data and the FFTs, we realized that for a given nanocrystal in the honeycomb geometry, extra weak reflections are present in the Fourier transforms of the middle part of the nanocrystals, indicated by white arrow in the Fourier transform at the left in Figure 6.1d, which are not present at the outer parts (Figure 6.1d right). The zone axis for the outer part is the [111] of the CdSe zinc blende structure. However, these extra reflections do not correspond to the zinc blende structure. The distances for these reflections match those at the [001] orientation of the wurtzite structure. We extended our approach to see whether these additional reflections in the FFT of the central part of the NCs are always present or only in some of the nanocrystals. The presence or lack of such extra reflections can again be used for the seed mediated segmentation. The results of this are shown in Figure 6.1e. It is clear that the central parts have extra reflections while further away from the center they disappear. This means that there are wurtzite domains in the center of the NCs, while the outside is composed of pure zinc blende, effectively forming wurtzite/zinc blende core/shell structures.

6.3 Band structure and optical absorption of CdSe superlattices

We have performed tight-binding (TB) calculations of the band structure for both square and honeycomb superlattices. Although the NCs have truncated cubic shape with defined crystallographic planes, the necks between NC-NC interfaces after oriented attachment result in a more spherical NC shape. Therefore, in our calculations we considered the NCs as spheres (with the size of 6.1 nm) attached by cylinders (with the length of 2.5 nm).

As can be observed in Figure 6.2a and b the valence bands in both superstructures show complicated energy dispersion due to the presence of coupled heavy-hole and light-hole bands.[31] The S-conduction band (in blue) is well separated from the next higher band states due to strong confinement.[32] The lowest conduction band is two-fold degenerate including the spins. For honeycomb superstructures, the lowest two conduction bands form a Dirac cone at the K-points. The Fermi-level will be positioned at this Dirac point, when every nanocrystal site (≡ 1/2 unit cell) is occupied with one electron. The next three bands consist of a flat band, and a second Dirac cone, due to coupling and interference of the in-plane P_x, P_y orbitals. The Fermi-level is situated at the second Dirac point if every CdSe nanocrystal site is occupied by 4 electrons.

The calculated absorption spectra of both superlattices are presented in Figure 6.2c and d. The total of all transitions is depicted in black. The blue-dashed spectrum is related to the transitions between the valence S-type and conduction S-type states. The peaks at lower and higher energy in these spectra represent the heavy hole and light hole transitions to

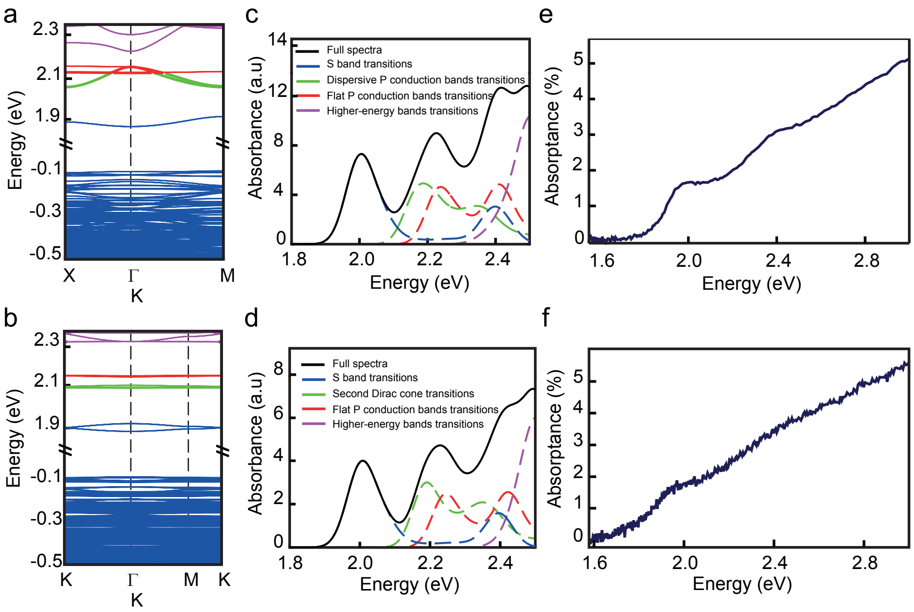

Figure 6.2. Band structure, orbital occupation and absorption spectra of 2D CdSe superlattices obtained from atomistic Tight-Binding calculation and experimental absorption spectra. (a, b) Highest valence and lowest conduction bands for a 2D CdSe square and honeycomb superlattice obtained from TB calculations. The S-conduction band (in blue) is well separated from the next higher band states due to strong confinement. The valence bands show a more complicated energy dispersion due to the presence of coupled heavy-hole and light-hole bands. The Fermi level crosses the lowest CB when every nanocrystal sites becomes occupied by one electron. For honeycomb superstructures, the lowest two conduction bands form Dirac Cones at the K-points. The Fermi level will be positioned at the Dirac point, when every nanocrystal site (≡ 1/2 unit cell) is occupied with one electron. (c, d) The TB calculated absorption spectrum of superstructures consists of four main transitions from valence bands to S-type, two P-type and higher energy states of the conduction band. The peaks at lower and higher energy in the S-type transitions represent the heavy hole and light hole transitions to the S-type conduction band, respectively. The NCs building blocks are considered to be sphere with a diagonal of 6.1 nm. The NCs are connected by cylinders with the length of 2.5 nm. (f) Experimental absorption spectra of a monolayer of CdSe superlattice with square (e) and honeycomb geometry with a very broad feature (peak) at 1.96 eV related to S_eS_h transitions. Both the theoretical spectra and the experimental spectra are unable to present fine structure related to the Dirac type bandstructure.

the S-type conduction band, respectively. The green and red dashed spectra are related to the transitions to the dispersive and flat P-type conduction bands, respectively. The P-type transitions start to contribute to the whole absorption spectrum at around 2.25 eV. The last contribution to the absorption spectrum is made by transitions to higher energy states in the conduction band (purple dashed spectrum). These calculated absorption spectra will serve as references to evaluate the experimental absorption bleach measurements. We should mention that excitonic effects are not considered in our calculations; these excitonic effects might shift the peaks by up to 100 meV to lower energy. Our calculation gives a bandgap of 1.66 eV (at 300K) for bulk zinc-blende CdSe, in agreement with experimental observation.[33]

The calculated absorption spectra of both superlattices (Figure 6.2c and d) show the same features; once a Gaussian temperature broadening of 35 meV is included, fine structure features related to the Dirac cone cannot be observed. This can be understood by the fact that we considered artificial broadening of 35 meV in the calculation parameters. The bandwidth of the S-type conduction bands in the CdSe honeycomb superlattices is less than 40 meV. Therefore, we cannot observe the influence of Dirac cones in the features of calculated absorption. If we consider a smaller artificial broadening of 5 meV in our calculation, the optical transitions between the valence and conduction Dirac cones may result in a double-peak absorption fine strucure due to the density of states approaching zero at the Dirac point (Figure A6.1).

The experimental absorption spectra of both superlattices are presented in Figure 6.2e and f with a very broad feature (peak) at 1.96 eV. This peak can be attributed to the S-type valence to S-type conduction band transitions. The second feature at higher energy of 2.38 eV in the absorption spectrum of the square superlattice can be related to transitions to dispersive or flat P-type bands, as predicted in the TB calculations. For the honeycomb superlattice, the fine structure due to the transitions between two Dirac cones cannot be observed in the absorption spectrum due to temperature broadening very possibly also disorders.

6.4 Band occupation and transport properties of CdSe superlattices

Below we discuss the band occupation and charge transport into the CdSe square superlattices obtained *via* cation exchange as explained above. The conduction band occupation of the CdSe square superstructures can be monitored by measuring the optical absorption during electrochemical gating (see Methods). Figure 6.3a shows the absorption difference while sweeping the potential (from 0 to -1.5 V *versus* Ag reference electrode) for four cyclic scans. The CV cycles show (almost) the same features demonstrating that electrons can be repeatedly injected into and extracted from the superlattice.

As presented in Figure 6.3b, at a potential of -0.9 V the absorption quenching starts and increases as the potential is decreased further. The spectra of the absorption bleach were fitted by three Gaussians to unveil the optical transitions (see details in Appendix A6.2). Since the potential dependences of the features at 1.97 and 2.42 eV are the same, the smaller feature at higher energy must also involve in $1S_e$ transition. Therefore, the bleaches at 1.97 eV and 2.42 eV are related to $1S_{3/2}1S_e$ (heavy hole-electron transition) and $2S_{3/2}1S_e$

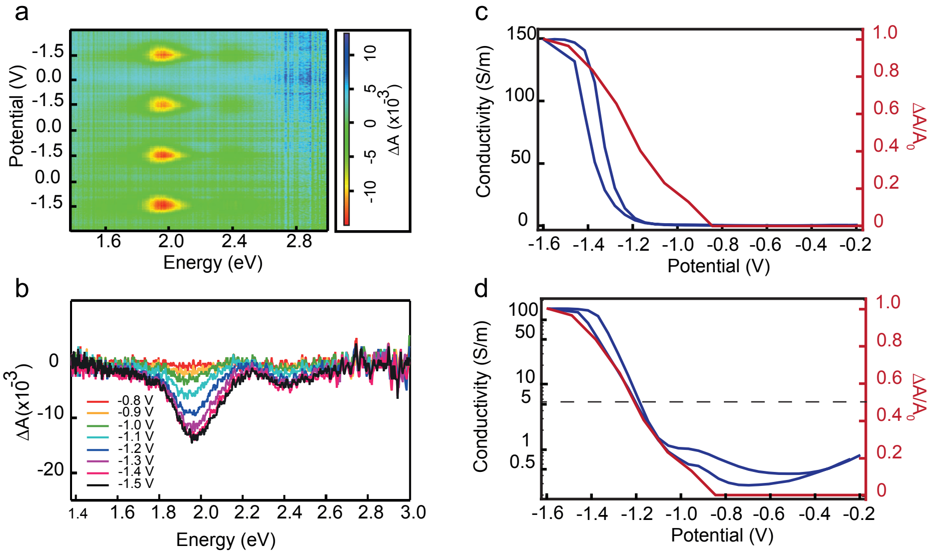

Figure 6.3. Occupation of the conduction bands and charge transport upon electron injection in a 2D square CdSe superlattice incorporated in an electrolyte-gated FET. (a) Differential absorbance as a function of the applied potential from 0 V to -1.5 V, electrons are injected in the CdSe superlattice and occupy the conduction bands, as seen by the enhanced absorption quenching (yellow-orange) for photon energies between 1.8 and 2.1 eV. In the reverse scan, electrons are extracted. The reproducibility of the signal shows that electron injection into and extraction from the CdSe superlattice is reversible. (b) Quenching of the light absorption measured in the range of 1.4 eV ≤ hυ ≤ 3eV at different potentials. Quenching is observed for potentials more negative than -0.9 V. The two features (at 1.97 eV and 2.42 eV) show the same saturation behavior and reflect occupation of the conduction S-band. Saturation is reached at two electrons per nanocrystal sites. At 2.1 - 2.2 eV, there is a non-saturated signal, reflecting occupation of the higher P-bands. (c) Conductivity obtained from the source-drain current and the geometry of the device (in blue). Fractional absorption related to $1S_{3/2}S_e$ transition (at hυ = 1.97 eV) (in red). The onset of the bleach is in close agreement with the onset of the conductance showing that injected electrons occupy only the conductive states. (d) The conductivity (blue) in logarithmic scale and fractional bleach of $1S_{3/2}S_e$ transition in linear scale (in red) showing that both conductivity and bleach sets on at nearly the same potential. The dashed line indicates the $\Delta A/A_0 = 0.5$ meaning that the S-type conduction band is half occupied.

(light hole-electron transition), respectively; which is in good agreement with our TB calculations presented in Figure 6.2c. At potentials more negative than -1.1 V another feature appeared in the differential absorption (see Figure A6.2). This feature is related to the P-band occupation which is also well captured by the TB calculations.

In order to investigate the conductivity of the superlattice, the source-drain current for small source-drain biases upto 45 mV was recorded. When the Fermi level is inside the conduction band, the current-voltage curves show Ohmic behavior and their slopes reveal the conductance of the sample. From the conductance and the geometry of the gap, the conductivity of the superlattice was obtained (for more detail see Appendix A6.3) as depicted in Figure 6.3c and d (in blue) in linear and logarithmic scales, respectively. The conductivity sets on at a potential of -1.1 V and increases to 150 S/m at the most negative potential. The fractional absorption ($\Delta A/A_0$), for $1S_{3/2}1S_e$ transition (at hυ = 1.97 eV) *versus* applied potential is plotted in Figure 6.3c and d (in red). ΔA is the bleach due to the S_e state filling (at each potential) and A_0 is the extremum of the bleach at the most negative potential (-1.5 V), for which we can assume that the S-band is fully occupied by 2 electrons. The onset of the $1S_{3/2}1S_e$ bleach is in close agreement with the onset of the conductance showing that the electrons in the S-conduction band are mobile. The existence of in-gap states cannot be entirely excluded from these results. The electron mobility of the sample calculated from the conductivity and electron density reaches a value of 0.6 $cm^2V^{-1}s^{-1}$ at the most negative potential.

We performed the same differential absorbance and conductivity measurements, as discussed above, on CdSe superlattices with honeycomb geometry. The results are shown in figure 6.4. The differential absorbance bleach spectra (Figure 6.4b) follow the same

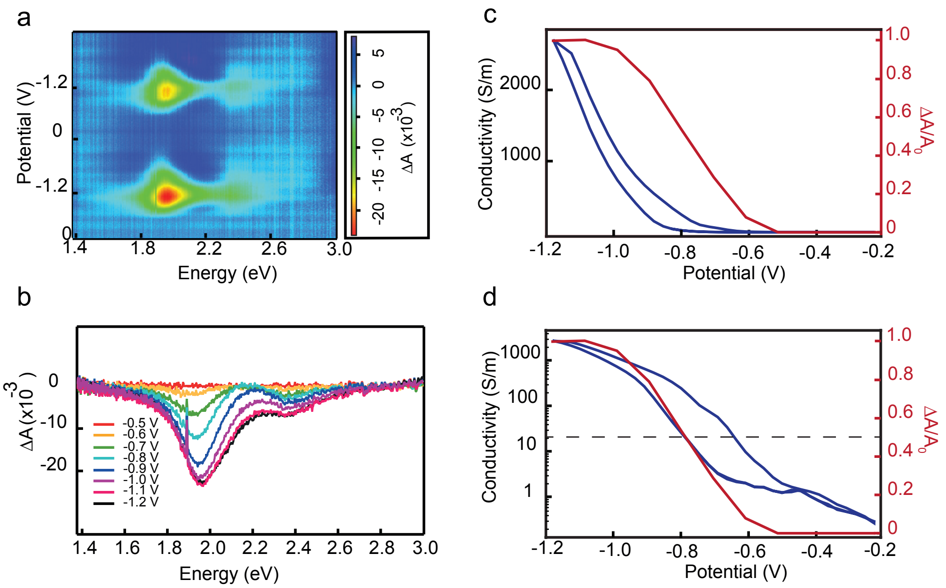

Figure 6.4. Band occupation and charge transport upon electron injection in a 2D honeycomb CdSe superlattice incorporated in an electrolyte-gated FET. (a) Differential absorbance as a function of the applied potential from 0 V to -1.2 V, electrons are injected in the conduction band of the CdSe honeycomb superlattice as seen by the enhanced absorption quenching (yellow-orange) for photon energy between 1.9 eV and 2 eV. In the reverse scan, electrons are extracted. The reproducibility of the signal shows that electron injection into and extraction from the CdSe superlattice is reversible. (b) Quenching of the light absorption measured in the range of 1.4 eV ≤ hυ ≤ 3eV at different potentials. Quenching is observed for potentials more negative than -0.6 V. The two features (at 1.97 and 2.35 eV) show the same saturation behavior and reflect occupation of the conduction S-band. Saturation is reached at two electrons per nanocrystal site. At 2 - 2.2 eV, there is a non-saturated signal, reflecting occupation of the higher P-bands. (c) Conductivity obtained from the source-drain current and the geometry of the device (in blue) and fractional absorption for S-S transition (in red). (d) The conductivity (blue) in logarithmic scale and average bleach related to $1S_{3/2}S_e$ transition in linear scale (in red). The dashed line indicates the $\Delta A/A_0 = 0.5$ meaning that the Fermi level is at the first Dirac cone in the conduction band.

trend observed for the square superlattice. The absorption quenching starts at -0.6 V at the regions of photon energies of 1.9 eV to 2 eV and 2.3 eV to 2.4 eV simultaneously and saturates at -1.1 V. This reveals that both features are related to the S-S transitions. The conductivity of the honeycomb superlattice reaches a higher value of 2600 S/m at the most negative potential (Figure 6.4c and d) leading to a mobility of 10 $cm^2V^{-1}s^{-1}$, considerably higher than for the square superlattice. However, more square and honeycomb samples have to be investigated before we have statistical trustful values of the respective electron mobilities.

6.5 Discussion

We have studied band occupation and electron transport in single sheets of CdSe with a square and honeycomb geometry. Until now, we have trustful results of only one sample for each geometry. This means that presented results should be seen as preliminary. These superstructures are atomically coherent due to the epitaxial connections between the nanocrystals. Theoretical studies have shown that the atomic connection of the NCs causes the electronic band structure of these superlattices to be profoundly distinct from that of weakly coupled nanocrystals and continuous nanosheets, with the appearance of Dirac cones in the case of a honeycomb superstructure.[26,27] Our electrolyte-gated transport measurements show that upon electron injection the lowest conduction band becomes occupied with up to 2 electrons per nanocrystal. Our results do not allow us to exclude electron occupation of localized states before the onset of the absorption bleach. Furthermore, no significant difference is observed in the band occupation of the square and honeycomb superlattices. Thermal broadening clouds the fine structure related to the Dirac bands. The small bandwidth of the S-type conduction band (≈ 40 meV) is comparable to the temperature broadening. Our recent work on the structural characterization of silicene-type honeycomb structures of PbSe indicates that there are several types of crystallographic defects in these superlattices.[24] In Chapter 5, we showed that despite the strong electronic coupling between the PbSe nanocrystals in the honeycomb superstructures, the mobility is limited by scattering on superlattice imperfections. It is well possible that structural disorder in the present CdSe superlattices affects the presence of mid-gap states and the electron transport.

We find a maximum average electron mobility of 0.6 $cm^2V^{-1}s^{-1}$ in the CdSe square superlattices. The mobility of the honeycomb sample has an order of magnitude higher value, 10 $cm^2V^{-1}s^{-1}$. We should mention here that the mobility of the superstructures can be strongly influenced by the thickness of the atomic connections (necks) between the NCs. Furthermore, due to the complication of the incorporation of CdSe superlattices in electrolyte-gate transistor devices, we have been able to perform these measurements on just one square and one honeycomb sample. Therefore, we are reluctant to relate the observed motilities to the nanoscale geometry of the superlattices. We remark that the electron mobility observed here for both superlattices is comparable to those observed for PbSe superstructures in Chapter 4 and 5.

6.6 Methods

PbSe QDs synthesis

PbSe QDs were synthesized based on Steckel *et al.* method.[34] For lead precursor, mixture of 4.77 g lead acetate trihydrate (99.999 %, Sigma-Aldrich), 12 g oleic acid (90 %, Sigma-Aldrich) and 39.75 g 1-octadecene (90 %, Sigma-Aldrich) were heated at 120 °C under vacuum for 2 hours. For selenium precursor, mixture of 4.5 g selenium powder (99.999 %, Alfa Aesar), 12.2 mL trioctylphosphine (90 %, Sigma-Aldrich) and 0.41 mL diphenylphospine (98 %, Sigma-Aldrich) were prepared by dissolving selenium. Subsequently, 10.25 mL of lead containing solution were heated up to 180 °C and 7.5 mL of selenium precursor was injected. The reaction was kept at 150 °C for 1 minute and quenched with 10 mL 1-butanol (99.8 % anhydrous, Sigma-Aldrich). The synthesized mixture was washed twice by methanol and butanol and re-dispersed in toluene. The final PbSe QDs had size of 5.8 ± 0.4 nm as inferred from TEM.

Oriented Attachment and Cation Exchange

The oriented attachment of PbSe QDs to form square and honeycomb superlattices were performed following our previous method.[22,23] For honeycomb superlattice, 350 µL of PbSe QDs dispersion in toluene with the concentration of 1.75×10^{-7} M was drop casted on top of 6.5 mL ethylene glycol (99.8 % anhydrous, Sigma-Aldrich) substrate in a glass petri dish with 28 mm in diameter. To obtain 2D square superlattice, the EG substrate contains 20nL of oleic acid (90 %, Sigma-Aldrich). The solution left at 20 °C for 1h and annealed step wise at 30 °C, 50 °C and 80 °C.

We transferred PbSe square and honeycomb lattices to CdSe via a cation exchange reaction

For this purpose, mixture of 0.55 g cadmium acetate dihydrate (99.99 %, Sigma-Aldrich), 5.42 g oleic acid (90 %, Sigma-Aldrich) and 21.6 mL 1-octadecene (90 %, Sigma-Aldrich) were heated at 120 °C under vacuum for 2 hours. The SiN TEM grids and the electrochemical gating electrodes with superlattices on top were kept in cadmium oleate solution for 1h at 150 °C and then 175 °C for 10 minutes. Afterwards, we cleaned the samples by immersing them in toluene, butanol/methanol (1:1) and methanol, respectively.

Region growing segmentation procedure

To determine the crystallographic orientation of every composing part in a given atomic resolution STEM image, we designed a region growing segmentation procedure where we compare the FFT of a small region around each pixel to the FFT of its surroundings, to determine which areas are in the same orientation. During this approach several random points, or 'seeds', are chosen on the high resolution image. For each 'seed' the pseudo diffraction pattern (FFT) of a small region (± 20 pixels), is compared to the pseudo diffraction pattern of its surrounding neighbors. This comparison consists of calculating the maximum of the normalized cross correlation between both images. Whenever the calculated maximum is higher than the predetermined threshold, both pixels are labelled as having the same orientation. When its lower, the neighboring pixel is defined as a new 'seed' for a new region and the labelling algorithm continues.

The conventional TEM and the HAADF-STEM images were obtained using FEI Tecnai 20 and FEI TITAN operated at 300 kV, respectively.

Spectroelectrochemical Measurements

To study the band occupation and charge transport of a 2D CdSe superlattice, an electrochemical gating method was used. By means of an optical bleach measurement band occupation mechanism and charge density of the superlattices were investigated. The device design used for this measurement is characterized by large gold grating electrodes on top of a thin Al layer as an optical reflector. This Al layer is isolated from the gold gratings *via* a thick layer of Al_2O_3. In this experiment, the supporting electrolyte consisted of a 0.1 M solution of $LiClO_4$ in polyethyleneglycol (PEG). Ag wire and Pt sheet were inserted to the electrolyte for reference and counter electrode, respectively. The Fermi level of the superlattices was moved toward conduction band (valence band) by applying a negative (positive) potential to the counter electrode with respect to the reference electrode, using a CHI832B potantiostat. Changes in the absorption of the superlattice were measured during gating with a DH-2000 halogen lamp as light source and detected with a USB2000 UV-vis spectrometer.

References

1. Woo, W. K. *et al.* Reversible charging of CdSe nanocrystals in a simple solid-state device. *Adv. Mater.* **14**, 1068–1071 (2002).
2. Yu, D., Wang, C., Wehrenberg, B. L. & Guyot-Sionnest, P. Variable range hopping conduction in semiconductor nanocrystal solids. *Phys. Rev. Lett.* **92**, 1–4 (2004).

3. Talapin, D. V & Murray, C. B. PbSe Nanocrystal Solids for n-and p-Channel Thin Film Field-Effect Transistors. Science **310**, 86–90 (2005).
4. Vanmaekelbergh, D. & Liljeroth, P. Electron-conducting quantum dot solids: Novel materials based on colloidal semiconductor nanocrystals. *Chem. Soc. Rev.* **34**, 299–312 (2005).
5. Luther, J. M. *et al.* 001-Schottky solar cells based on colloidal nanocrystal films. *Nano Lett.* **8**, 3488–3492 (2008).
6. Khon, E. *et al.* Inorganic solids of CdSe nanocrystals exhibiting high emission quantum yield. *Adv. Funct. Mater.* **22**, 3714–3722 (2012).
7. Law, M. *et al.* Structural, optical, and electrical properties of PbSe nanocrystal solids treated thermally or with simple amines. *J. Am. Chem. Soc.* **130**, 5974–5985 (2008).
8. Liu, W., Lee, J. S. & Talapin, D. V. III-V nanocrystals capped with molecular metal chalcogenide ligands: High electron mobility and ambipolar photoresponse. *J. Am. Chem. Soc.* **135**, 1349–1357 (2013).
9. Nag, A., Zhang, H., Janke, E. & Talapin, D. V. Inorganic surface ligands for colloidal nanomaterials. *Zeitschrift für Phys. Chemie* **229**, 85–107 (2015).
10. Chiu, S. C., Jhang, J. S., Chen, J. F., Fang, J. & Jian, W. Bin. Effects of cross-sectional area on the tunneling-junction array in octahedral PbSe colloidal-nanocrystal solids. *Phys. Chem. Chem. Phys.* **15**, 16127–16131 (2013).
11. Lee, J. S., Kovalenko, M. V., Huang, J., Chung, D. S. & Talapin, D. V. Band-like transport, high electron mobility and high photoconductivity in all-inorganic nanocrystal arrays. *Nat. Nanotechnol.* **6**, 348–352 (2011).
12. Chung, D. S. *et al.* Low voltage, hysteresis free, and high mobility transistors from All-inorganic colloidal nanocrystals. *Nano Lett.* **12**, 1813–1820 (2012).
13. Jarosz, M. V., Porter, V. J., Fisher, B. R., Kastner, M. A. & Bawendi, M. G. Photoconductivity studies of treated CdSe quantum dot films exhibiting increased exciton ionization efficiency. *Phys. Rev. B* **70**, 1–12 (2004).
14. Choi, J. H. *et al.* Bandlike transport in strongly coupled and doped quantum dot solids: A route to high-performance thin-film electronics. *Nano Lett.* **12**, 2631–2638 (2012).
15. Oh, S. J. *et al.* Stoichiometric control of lead chalcogenide nanocrystal solids to enhance their electronic and optoelectronic device performance. *ACS Nano* **7**, 2413–2421 (2013).
16. Talgorn, E. *et al.* Unity quantum yield of photogenerated charges and band-like transport in quantum-dot solids. *Nat. Nanotechnol.* **6**, 733–739 (2011).
17. Liu, Y. *et al.* Dependence of carrier mobility on nanocrystal size and ligand length in PbSe nanocrystal solids. *Nano Lett.* **10**, 1960–1969 (2010).
18. Murphy, J. E., Beard, M. & Nozik, A. Time-resolved photoconductivity of PbSe nanocrystal arrays. *J. Phys. Chem. B* **110**, 25455–25461 (2006).
19. Talapin, D. V & Murray, C. B. PbSe Nanocrystal Solids for n-and p-Channel Thin Film Field-Effect Transistors. *Science* **310**, 86–90 (2005).
20. Yu, D., Wehrenberg, B. L., Jha, P., Ma, J. & Guyot-Sionnest, P. Electronic transport of n-type CdSe quantum dot films: Effect of film treatment. *J. Appl. Phys.* **99**, (2006).
21. Norman, Z. M., Anderson, N. C. & Owen, J. S. Electrical Transport and Grain

Growth in Solution-Cast, Chloride-Terminated Cadmium Selenide Nanocrystal Thin Films. *ACS Nano* **8**, 7513–7521 (2014).

22. Boneschanscher, M. P. *et al.* Long-range orientation and atomic attachment of nanocrystals in 2D honeycomb superlattices. *Science* **344**, 1377–1380 (2014).
23. Evers, W. H. *et al.* Low-Dimensional Semiconductor Superlattices Formed by Geometric Control over Nanocrystal Attachment. *Nano Lett.* **13**, 2317–2323 (2013)
24. Peters, J. L. *et al.* Mono- and Multilayer Silicene-Type Honeycomb Lattices by Oriented Attachment of PbSe Nanocrystals: Synthesis, Structural Characterization, and Analysis of the Disorder. *Chem. Mater.* **30**, 4831–4837 (2018).
25. Whitham, K. *et al.* Charge transport and localization in atomically coherent quantum dot solids. *Nat. Mater.* **15**, 557–563 (2016).
26. Kalesaki, E., Evers, W. H., Allan, G., Vanmaekelbergh, D. & Delerue, C. Electronic structure of atomically coherent square semiconductor superlattices with dimensionality below two. *Phys. Rev. B* **88**, 1–9 (2013).
27. Kalesaki, E. *et al.* Dirac cones, topological edge states, and nontrivial flat bands in two-dimensional semiconductors with a honeycomb nanogeometry. *Phys. Rev. X* **4**, 1–12 (2014).
28. Evers, W. H. *et al.* High charge mobility in two-dimensional percolative networks of PbSe quantum dots connected by atomic bonds. *Nat. Commun.* **6**, 1–8 (2015).
29. Beberwyck, B. J., Surendranath, Y. & Alivisatos, A. P. Cation exchange: A versatile tool for nanomaterials synthesis. *J. Phys. Chem. C* **117**, 19759–19770 (2013).
30. Luther, J. M., Zheng, H., Sadtler, B. & Alivisatos, A. P. Synthesis of PbS nanorods and other ionic nanocrystals of complex morphology by sequential cation exchange reactions. *J. Am. Chem. Soc.* **131**, 16851–16857 (2009).
31. Tadjine, A. & Delerue, C. Colloidal nanocrystals as LEGO® bricks for building electronic band structure models. *Phys. Chem. Chem. Phys.* **20**, 8177–8184 (2018).
32. Christophe J. D., Lannoo M. Nanostructures: Theory and Modeling. (*Springer*, 2006).
33. Kim, Y. D. *et al.* Optical properties of zinc-blende CdSe and $Zn_xCd_{1-x}Se$ films grown on GaAs. *Phys. Rev. B* **49**, 7262–7270 (1994).
34. Steckel, J. S., Yen, B. K. H., Oertel, D. C. & Bawendi, M. G. On the mechanism of lead chalcogenide nanocrystal formation. *J. Am. Chem. Soc.* **128**, 13032–13033 (2006).

Appendix

A6.1 Optical absorption obtained from tight-binding calculation with artificial broadening of 5 meV

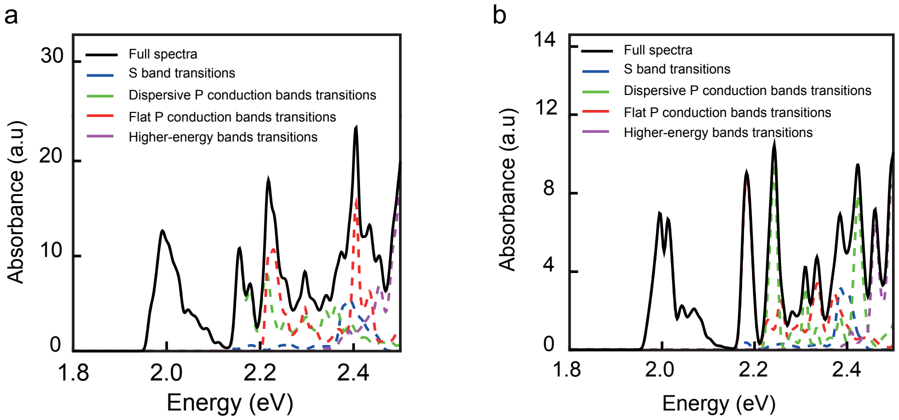

Figure A6.1. Absorption spectra of 2D CdSe superlattices obtained from atomistic Tight-Binding calculation with artificial broadening 5 meV. (a, b) The absorption spectrum of superstructures consists of four main transitions from valence bands to S-type, two P-type and higher energy states of the conduction band. The main difference between the spectrum of the square and honeycomb superlattice is that the S_eS_h transition peak splits in two small narrow peaks indicating the existence of massless electrons in the S-type Dirac cones. The NCs building blocks are considered to be sphere with a diagonal of 6.1 nm. The NCs are connected by cylinders with the length of 2.5 nm.

A6.2 Fitted optical absorption bleach of CdSe superlattices

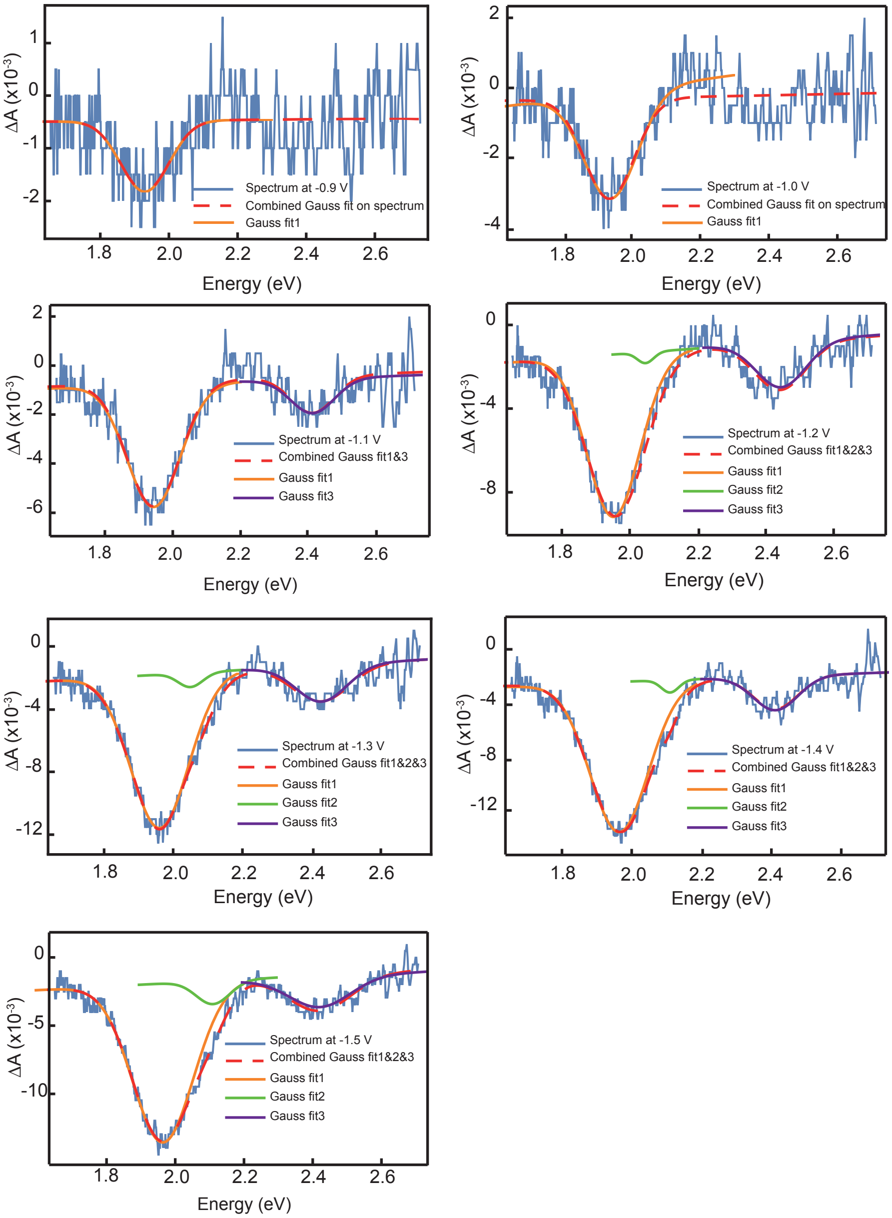

Figure A6.2. Fitted absorption bleach spectra of the square superlattice upon applied potential from -0.9 V to -1.5 V with three Gaussians. The fitting indicates the appearance of a small bleach feature in the range of 2 eV to 2.2 eV for potential more negative than -1.1 V. This feature can be related to the P-band occupation.

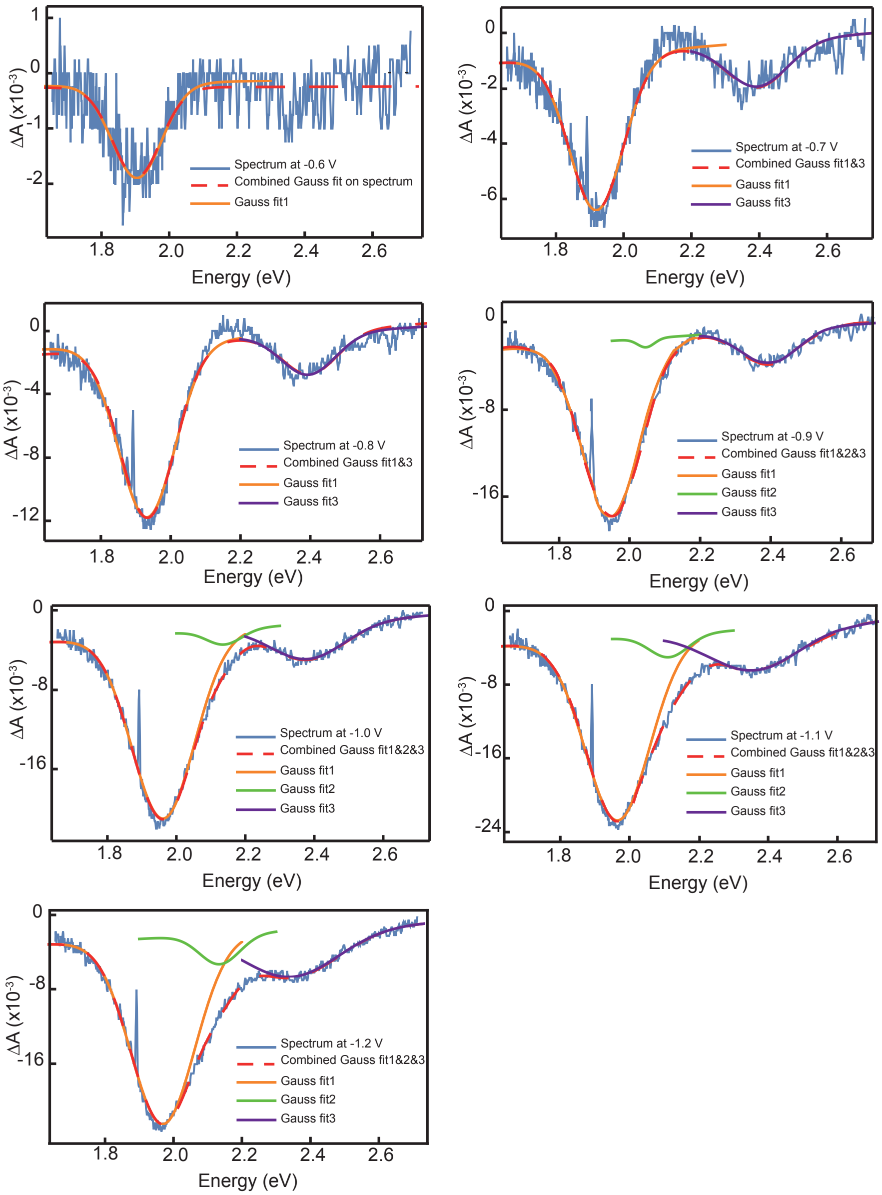

Figure A6.3. Fitted absorption bleach spectra of the honeycomb superlattice upon applied potential from -0.6 V to -1.2 V with three Gaussians. The fitting indicates the appearance of a small bleach feature in the range of 2 eV to 2.2 eV for potential more negative than -0.8 V. This feature can be related to the P-band occupation.

A6.3 Conductivity and mobility calculation

From the source-drain current *versus* applied potential in transport measurement, the conductance of the network can be calculated. The conductivity, σ, of the CdSe nanocrystal sheet can be determined from the conductance and the geometry of the fingers:

$$\sigma = \frac{G \times w}{h \times L} \qquad \text{(Eq. A6.1)}$$

where σ is conductivity, w and L the width and length of the gap, G is conductance and h is monolayer thickness.

The number of charges injected into a superlattice energy level can be determined from:

$$\langle n_i(V) \rangle = g_i \int_0^{\infty} \frac{A_i(V) - A_i(V_{oc})}{A_i(V_{oc})} dE \qquad \text{(Eq. A6.2)}$$

Therefore, the mobility can be:

$$\mu = \frac{\sigma}{n \times e} \qquad \text{(Eq. A6.3)}$$

n is charge density calculated from absorption quenching and e is elementary charge.

Chapter 7

Summary & Outlook

Abstract

The experiments presented in this thesis have provided new insights regarding the optoelectronic properties of two-dimensional PbSe and CdSe superlattices with superimposed square and honeycomb geometries, which have been prepared by interfacial nanocrystal assembly and attachment. We studied the light absorption properties of these superlattices using absorption and photoconductivity techniques. Furthermore, we incorporated single-layers of the superlattices into transistor-type devices and extensively investigated the band occupation and charge transport in the superlattices by electrochemical gating. We also studied the charge transport in the PbSe honeycomb superlattices by terahertz spectroscopy. In this chapter we summarize the main results and briefly discuss the potential ideas for the future of this research.

7.1 Introduction

Semiconductor nanocrystals (NCs) have gained a lot of attention because their optoelectronic properties can be tuned by variation of size, shape and composition. The effects of nanocrystal structure on the optoelectronic properties are of scientific interest and offer challenging prospects for applications in optoelectronic devices. In the experiments presented in this thesis, we studied the optoelectronic properties of coherent 2D superlattices, with just a monolayer thickness, formed from Pb- and Cd- chalcogenide nanocrystals that are epitaxially connected. Calculations show that if the coupling between the nanocrystals is strong enough, a novel material is developed with a geometry-specific band-structure.[1] In particular, it has been calculated that two-dimensional NC superstructures with a honeycomb geometry show Dirac-type valence- and conduction-bands, separated by the semiconductor band gap, thus combining valuable semiconductor properties with those of graphene.[2]

7.2 Formation of 2D superlattices

The highly ordered 2D PbSe superlattices studied in this thesis are formed by using the liquid substrate procedure (Figure 7.1). We drop cast PbSe NCs dispersion in toluene on top of ethylene glycol as liquid substrate. The NCs do not dissolve in the ethylene glycol, but adsorb at the liquid/nitrogen interface. After the solvent (toluene) evaporates and some of the surface ligands dissolve in the ethylene glycol, the NCs attach *via* their {100} facets and form 2D square superlattices with just a monolayer thickness (Figure 7.2a). Honeycomb superlattices (Figure 7.2b) are obtained by an ultra-slow oriented attachment procedure where the solvent evaporation occurs under a gas atmosphere (Figure 7.1b).[3] We transform PbSe square and honeycomb superlattices into CdSe *via* a Cd^{2+} for Pb^{2+} cation exchange reaction. In the cation exchange reaction, the Pb cations are exchanged

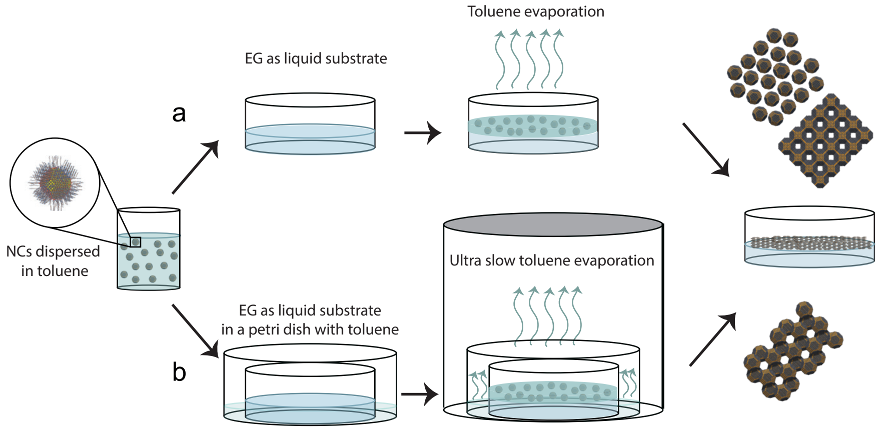

Figure 7.1. Schematic representation of the experimental setup for self-assembly and oriented attachment of PbSe NCs. A dispersion of PbSe NCs in toluene is prepared. (a) The NCs dispersion is drop casted on top of the EG substrate, after which the toluene evaporates. The PbSe square superlattices are formed by assembling PbSe NCs at the toluene/air interface after which the NCs attach *via* their four vertical {100} facets. (b) To form honeycomb superlattices, an ultra-slow oriented attachment procedure is used where the solvent evaporation occurs under a gas atmosphere.

with Cd cations from a solution contacting the superlattice. This chemical transformation can be complete and preserves the nanoscale square or honeycomb geometry of the superlattice (Figure 7.2c).

7.3 Light absorption by 2D superlattices

One of the remarkable optical properties of 2D systems is the universal value of light absorptivity by these materials. Free-standing graphene is found to absorb a significant amount of light, $\pi\alpha$ = 2.3 % (α being the fine structure constant), related to its two-dimensional nature.[4] Yablonovitch and co-workers indicated that the magnitude of the light absorption in InAs quantum membranes (QMs) is an integer product of quantum absorptance; $A_Q = \pi\alpha/n_c$ = 1.6 %, where α is a fine structure constant and n_c is the optical local field correction factor.[5]

In **Chapter 3** we study the light absorption properties of 2D PbSe and CdSe superlattices with a square and honeycomb geometry. We demonstrate that the absorptivity of a monolayer superlattice is about 1.6 ± 0.1 %, independent of the material (CdSe or PbSe) and geometry (square or honeycomb); this is in good agreement with optical transitions in a quantum membrane as reported by Feng *et al.*.[5] One additional layer of PbSe superlattice adds another 1.6 ± 0.1 % to the absorptance. Figure 7.2d-f show the absorption spectra of all superlattices. In addition, we show that the honeycomb superlattice of PbSe nanocrystals can be incorporated in a photodetector device. The responsivity spectrum closely reproduces the same features of the absorption spectrum of the PbSe honeycomb superlattices, however with a better signal-to-noise ratio.

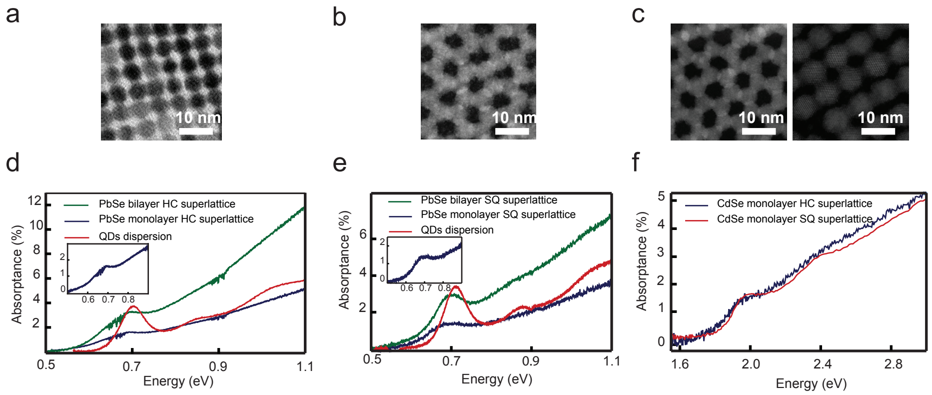

Figure 7.2. TEM, HAADF-STEM and absorption spectra of PbSe and CdSe square and honeycomb superlattices. (a, b, c) TEM and HAADF-STEM images of a part of a PbSe and CdSe square and honeycomb lattices (monolayer) prepared by self-assembly and oriented attachment. (d, e) Absorption spectra of a mono and double layer of PbSe superlattices. The first excitonic absorption features show a red shift and broadening, compared to the NCs in suspension (red curve). For the superlattices, a NC monolayer in thickness on a quartz substrate, the absorption is 1.5 % at photon energy of 0.69 eV. The addition of one more layer adds another 1.5 % to the light absorptance. Inset: Zoom-in of monolayer absorption in the energy range of 0.5 eV to 0.9 eV for better observation of the absorption peak shape. (f) Absorption spectrum of a monolayer of CdSe honeycomb and square superlattices. These single layers of CdSe honeycomb superlattices absorb 1.65 % of the white light.

7.4 Band occupation and charge transport in the superlattices

From an electronic viewpoint, the as-prepared 2D superlattices are intrinsic semiconductors. To populate the conduction (valence) bands with electrons (holes) in a controlled way, chemical doping or external gating is required. In **Chapter 4, 5** and **6**, it is shown that square and honeycomb superlattices of PbSe and CdSe nanocrystals can be transferred and incorporated as a nanocrystal monolayer in a transistor setup with an electrolyte gate (Figure 7.3a). The devices used for these measurements consist of interdigitated source and drain electrodes, on top of a Si-SiO$_2$ substrate (Figure 7.3b). In these experiments we used acetonitrile and polyethylene glycol (PEG) containing Li$^+$ salt as electrolytes. An Ag wire and a Pt sheet were inserted into the electrolyte for reference and counter electrodes, respectively (Figure 7.3c). The Fermi level of the superlattices moves towards the conduction band (valence band) by applying negative (positive) potential with respect to the reference electrode by using a potentiostat.

In **Chapter 4** we study the injection of carriers into the PbSe square superlattices by using three types of liquid electrolyte gating; differential absorption experiments, differential capacitance measurements and two- and four-probe conductance measurements in a Hall-bar geometry. By means of a differential capacitance measurements and a differential absorption experiments the band occupation is monitored and high electron densities between 1 and 8 electrons/NC sites are determined. The electron mobility at room temperature obtained from the electron densities and conductivity measurements is between 5 and 18 cm^{2}V^{-1}s^{-1}.

Chapter 5 presents a study of the band occupation and charge transport in PbSe Silicene-type honeycomb superlattices at room temperature, using both electrochemical gating

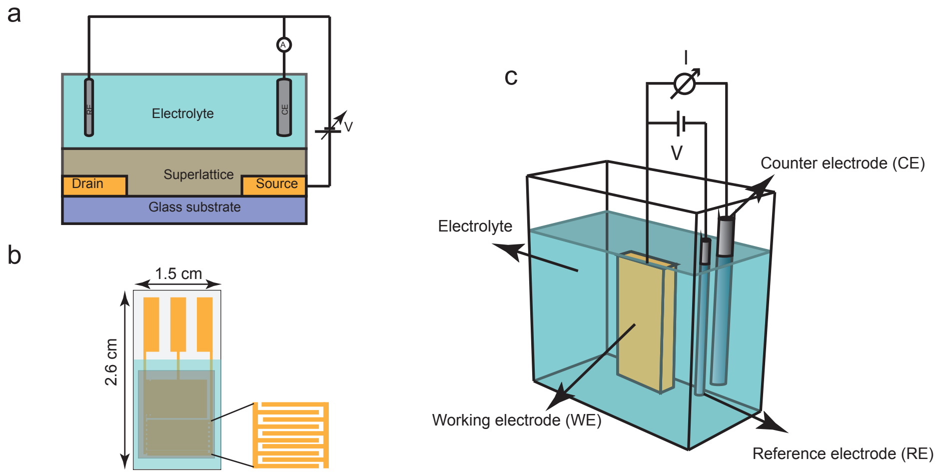

Figure 7.3. Schematic diagram of transistor setup, electrode design and three-electrode electrochemical cell in electrochemical gating measurements. (a) A transistor setup of superstructure monolayer with an electrolyte gate. (b) The devices used for the measurements consist of interdigitated source and drain electrodes on top of a Si-SiO$_2$ substrate. (c) Typical three-electrode electrochemical cell with a working electrode a reference electrode (RE) and a counter electrode (CE).

and terahertz spectroscopy. Our electrolyte-gated transport measurements show that injected electrons occupy the lowest conduction band. However, injected holes might either occupy the valence band or localized in-gap states. The similarity between the mobility obtained with an electrochemically gated transistor and the THz mobility is remarkable (both values are about 1.5 $cm^2V^{-1}s^{-1}$). This indicates that the quantum yield for charge carrier photo-generation in the terahertz experiments is close to unity, and also that mainly electrons contribute to the THz conductivity. It has been shown that even though the honeycomb domains are very large, there are several types of crystallographic defects, mostly related to non-ideal [100]/[100] connections between the constituting NCs.[3] Therefore, in our opinion, the electron mobility of the honeycomb superlattice is limited by lattice imperfections, giving rise to the similarity between THz and DC electron mobilities.

In **Chapter 6** we show that the rock salt square and honeycomb superlattices of PbSe NCs are transformed to wurtzite/zinc blende core/shell superlattices of CdSe *via* cation exchange. A monolayer of CdSe superlattices is incorporated in a transistor type setup with electrolyte gating. The conductivity and differential bleach measurements show that the injected electrons occupy the lowest conduction band with up to 2 electrons per nanocrystals. There is no indication of localized in gap states in these measurements. The electron mobility observed for these superlattices is up to 10 $cm^2V^{-1}s^{-1}$, which is comparable to those observed for the PbSe superlattices in chapters 4 and 5.

7.5 Outlook

The broad absorption peak without any sign of the predicted Dirac features in the CdSe honeycomb absorption spectrum (Figure 7.2f) indicates that several origins of broadening must be present. Tentative explanations are: the small bandwidth of the S-type conduction band (≈ 40 meV) compared to temperature broadening, broadening effects due to several types of structural disorder, and possibly (e, h) Coulomb effects. In line with this the room temperature electron transport properties, even with the Fermi level being resonant with the Dirac point, show no signs of special properties related to the linear dispersion relation, but appear instead to be dominated by disorder. Applying cryogenic techniques to investigate the absorption spectrum of the honeycomb superlattices seems to be essential. Therefore, since the signal-to-noise in the responsivity spectra of the photoconductivity measurement is much better than in light transmission measurements, performing the photoconductivity measurements at cryogenic temperatures on CdSe honeycomb superlattices should be considered.

The electronic characterizations at room-temperature presented in this thesis show that it should be possible to subtly move the Fermi level through the energy range of the conduction mini-band of the superlattices. Once PbSe and CdSe honeycomb transistor-type devices can be cooled down to cryogenic temperatures (*i.e.* $k_BT <<$ band width), it should be possible to study the transport physics with the Fermi-level positioned in a narrow energy window, *e.g.* to distinguish the Γ point from K-points. Eventually, this research would enable to display the Dirac character of the carriers in the energy region around the K-points, as has been predicted theoretically.

References

1. Kalesaki. *et al.* Electronic structure of atomically coherent square semiconductor superlattices with dimensionality below two. *Phys. Rev. B* **88**, 1–9 (2013).
2. Kalesaki, E. *et al.* Dirac cones, topological edge states, and nontrivial flat bands in two-dimensional semiconductors with a honeycomb nanogeometry. *Phys. Rev. X* **4**, 1–12 (2014).
3. Peters, J. L. *et al.* Mono- and Multilayer Silicene-Type Honeycomb Lattices by Oriented Attachment of PbSe Nanocrystals: Synthesis, Structural Characterization, and Analysis of the Disorder. *Chem. Mater.* **30**, 4831–4837 (2018).
4. Nair, R. R. *et al.* Fine Structure Constant Defines Visual Transperency of Graphene. *Science* **320**, 2008 (2008).
5. Fang, H. *et al.* Quantum of optical absorption in two-dimensional semiconductors. *Proc. Natl. Acad. Sci.* **110**, 11688–11691 (2013).

Samenvatting in het Nederlands

Overzicht

In dit hoofdstuk wordt het onderzoek van dit proefschrift samengevat voor een breder publiek. Er wordt een korte inleiding over halfgeleider nanokristallen gegeven gevolgd door de belangrijkste resultaten en ideeën voor verder onderzoek.

I. Inleiding

Het onderzoek gepresenteerd in dit proefschrift richt zich op de opto-elektronische eigenschappen van tweedimensionale (2D) superstructuren van halfgeleider nanokristallen. Maar wat zijn half-geleider nanokristallen? Wat betekent 2D en hoe hebben we een 2D superstructur gemaakt met deze nanokristallen? Wat zijn de opto-elektronische eigenschappen van de superstructuren en hoe hebben we deze gemeten? In dit hoofdstuk zullen wij proberen deze vragen te beantwoorden.

Wat zijn halfgeleiders? Op basis van hun geleidende eigenschappen kunnen materialen worden ingedeeld in drie verschillende categorieën: geleiders, isolatoren en halfgeleiders. Deze classificatie is gebaseerd op de beweging van elektronen (elektrische stroom) in de materialen. Geleiders zijn materialen waarin elektronen gemakkelijk kunnen bewegen, *b.v.* zilver of koper. Het tegenovergestelde van een geleider is een isolator. Een isolator belemmert de stroom van elektronen. Glas, plastic en papier zijn goede voorbeelden van isolatoren. Halfgeleiders gedragen zich tussen geleiders en isolatoren in. In een halfgeleider kunnen de elektronen bewegen als een bepaalde hoeveelheid energie wordt geleverd. Silicium is de meest gebruikte halfgeleider.

Wat is een nanokristal? Een kristal is een vast materiaal waarin de componenten (bijvoorbeeld atomen of moleculen) in een ordelijk herhalend patroon zijn gerangschikt. Suiker, sneeuwvlokken en edelstenen, zoals diamant en kwarts, zijn allemaal kristallen. Het voorvoegsel “nano” betekent “miljardste”, dus een nanometer is een miljardste van een meter. Wij leven op de schaal van meters en kilometers en het is daarom moeilijk voor ons om een “nano” object voor te stellen. De volgende voorbeelden kunnen helpen de nanoschaal te visualiseren. Een stuk papier is ongeveer 100000 nanometer dik. Als je een van je haren over de lengte snijdt in 100000 stukjes, is elk stukje één nanometer dik. Een nanokristal is een kristal met tenminste één dimensie op nanometerschaal. Voor ons onderzoek hebben we loodselenide (PbSe) en cadmiumselenide (CdSe) nanokristallen met een diameter van 5.5 tot 6.3 nm gebruikt.

Wat is een tweedimensionaal (2D) materiaal? 2D-materialen, soms ook enkellaagse materialen genoemd, zijn kristallijne materialen bestaande uit een enkele laag atomen. In dit onderzoek maakten we een enkele laag (monolaag) van aangehechte PbSe- en CdSe-nanokristallen met een vierkant en een hexagonaal (honingraat) patroon. Deze structuren worden 2D-superstructuren genoemd. Figuren la en 1b tonen modellen van vierkante en honingraat superstructuren gemaakt van PbSe nanokristallen.

Waarom zijn we geïnteresseerd in deze 2D superstructuren? De interesse in 2D superstructuren komt van grafeen dat ook een hexagonaal patroon heeft, zoals getoond in figuur 1c. Grafeen heeft een speciale eigenschap die in de volgende paragraaf zal worden uitgelegd.

Voordat we de speciale eigenschappen van grafeen uitleggen, is het nodig om het concept “bandstructuur” te introduceren. Zoals we eerder hebben vermeld, classificeren we de materialen als geleiders, isolatoren en halfgeleiders op basis van de beweging van elektronen. Het energiebereik dat deze elektronen in het materiaal kunnen hebben en het

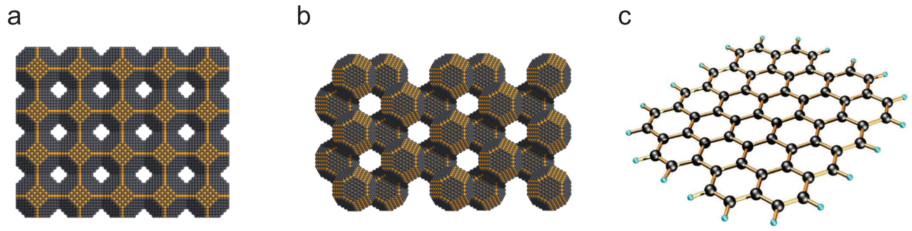

Figuur 1. Modellen van (a) vierkante en (b) honingraat superstructuren gemaakt van PbSe nanokristallen. De zwarte (gele) bollen vertegenwoordigen de Pb (Se) atomen. (c) grafeenrooster gemaakt van koolstofatomen[1]. De zwarte bollen vertegenwoordigen koolstofatomen.

energiebereik dat ze niet kunnen hebben (bekend als bandkloof of verboden banden) kan worden beschreven door "bandstructuur". De bandstructuur van de materialen kan op verschillende manieren worden berekend en kan veel informatie geven over de materialen zelf. Als voorbeeld wordt de bandstructuur van indiumarsenide getoond in figuur 2a. Elke lijn in de bandstructuur vertegenwoordigt de energie die elk elektron kan hebben. Als er geen lijn is betekent dit dat er een bandkloof is. De speciale eigenschap van grafeen komt van de unieke bandstructuur die wordt getoond in figuur 2b. Er zijn enkele punten in de bandstructuur waar de energielijnen elkaar ontmoeten. Deze punten worden Dirac-kegels genoemd. Omdat de energielijnen elkaar raken, is er geen bandkloof ter hoogte van de Dirac-kegels. Dit betekent dat elektronen gemakkelijker en sneller kunnen bewegen als ze de energie hebben om de Dirac-kegels te bereiken. Wetenschappers denken dat deze eigenschap het resultaat is van het hexagonale patroon van grafeen. We verwachten daarom dezelfde Dirac-kegels te zien in de bandstructuur van onze hexagonale (honingraat) superstructuren. Theoretische berekeningen bevestigden onze voorspelling van de aanwezigheid van Dirac-kegels in de bandstructuur van de honingraat superstructuren, zoals weergegeven in figuur 2c.

II. Synthese van 2D superroosters

De 2D superstructuren, met vierkante en honingraatgeometrie, worden gevormd door gebruik te maken van een vloeibaar substraat. Het syntheseproces is weergegeven in figuur

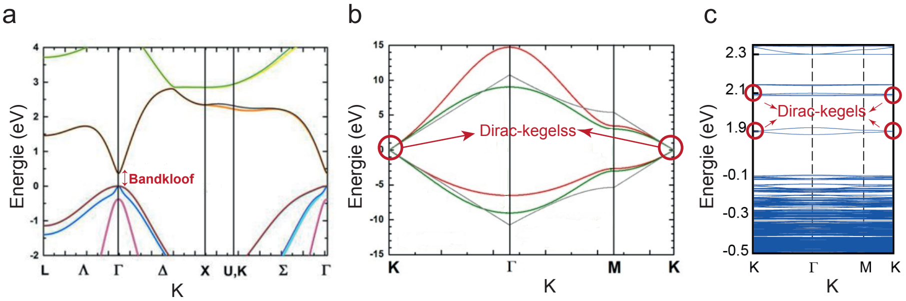

Figuur 2. Bandstructuur van (a) een indiumarsenide halfgeleider[2], (b) een grafeenrooster met Dirac-kegels[2] en (c) een CdSe honingraat superstructur met Dirac-kegels. Dirac-kegels zijn de punten waar de energielijnen elkaar ontmoeten.

3a. Eerst verdunnen we de PbSe nanokristallen in een oplosmiddel, meestal tolueen. De PbSe nanokristallen hebben de vorm van een kubus; ze zijn echter geen volledige kubus. Er zijn enkele afknottingen op de hoeken en randen van de kubussen die verschillende facetten op het oppervlak van de nanokristallen creëren. Deze afgeknotte PbSe nanokubussen hebben 6 {100}, 12 {110} en 8 {111} facetten, zoals geïllustreerd in figuur 3b. Na verdunning wordt de suspensie van PbSe nanokristallen op een zeer viskeus vloeibaar substraat gebracht (ethyleenglycol) waarna het oplosmiddel verdampt. De nanokristallen hechten via hun {100} facetten en vormen 2D vierkante en honingraat superstructuren van slechts één enkele laag (figuur 3c en d). In de vierkante superstructuren verbinden de nanokristallen zich via hun vier verticale {100} facetten, zoals afgebeeld in de inzet van figuur 3c. In de honingraat superstructuren vormen de nanokristallen via drie van de {100} facetten een golfstructuur (inzet figuur 3d).

We kunnen de superstructuren niet rechtstreeks maken van CdSe nanokristallen, omdat deze nanokristallen bollen zijn en geen kubussen met facetten. Om CdSe superstructuren te verkrijgen, transformeren we vierkante en honingraat superstructuren van PbSe naar CdSe-structur via een Cd voor Pb-uitwisselingsreactie. Hiervoor brengen we de

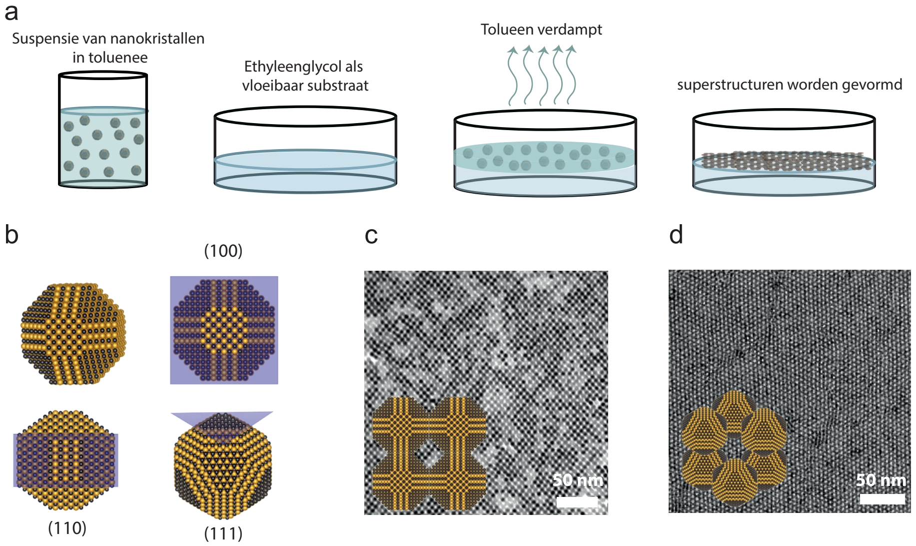

Figuur 3. (a) Schematische weergave van de experimentele opstelling voor het maken van de vierkante en honingraat superstructuren van PbSe nanokristallen. We gebruiken een suspensie van gefacetteerde PbSe nanokubussen. De suspensie wordt druppelsgewijs aangebracht op een viskeus vloeibaar substraat (ethyleenglycol) waarna het oplosmiddel verdampt en de nanokristallen via hun {100} facetten hechten en 2D vierkante en honingraat superstructuren vormen. (b) Model van de gefacetteerde kubussen van PbSe nanokristallen met 6 {100}, 12 {110} en 8 {111} vlakken. De zwarte (gele) bollen vertegenwoordigen de Pb (Se) atomen. (c) Transmissie-elektronenmicroscopie (TEM) afbeelding van een deel van een vierkant PbSe superstructur. De PbSe nanokristallen hechten met behulp van de vier verticale {100} facetten, zoals afgebeeld in de inzet. (d) TEM-afbeelding van een deel van een honingraat PbSe superstructuren. De PbSe nanokristallen hechten via de {100} facetten. Inzet: een model van zes nanokristallen in het superstructur met honingraatvelden waarbij de nanokristallen via drie van hun {100} facetten zijn verbonden en een golfstructuur vormen.

superstructuren van het vloeibare substraat over op elk gewenst substraat, bijvoorbeeld glas. We maken een oplossing met Cd en we houden het substraat met superstructuren in deze oplossing en verhogen de temperatuur van de oplossing tot 150 °C. Bij deze temperatuur wordt de Pb in de superstructuren vervangen door de Cd in de oplossing.

III. Opto-elektronische eigenschappen van 2D superstructuren

We hebben al eerder gezegd dat we geïnteresseerd zijn in de opto-elektronische eigenschappen van onze superstructuren. In de opto-elektronica draait het om de detectie, vorming en manipulatie van licht voor verschillende doeleinden. De 2D superstructuren die we hebben gemaakt, hebben een groot potentieel om te worden gebruikt in transistors, zonnecellen en fotodetectoren. In de volgende alinea's zullen we het onderzoek van de opto-elektronische eigenschappen van onze superstructuren beschrijven.

Lichtabsorptie door 2D superstructuren

Een van de technieken die we hebben gebruikt om de opto-elektronische eigenschappen van onze superstructuren te onderzoeken is lichtabsorptie. De resultaten van dit onderzoek zijn beschreven in **Hoofdstuk 3** van dit proefschrift. Bij lichtabsorptie ligt de frequentie van de invallende lichtgolf op of dichtbij de energieniveaus van de elektronen in het materiaal. De elektronen absorberen de energie van de lichtgolf en veranderen hun energietoestand. Er zijn verschillende opties voor wat er vervolgens kan gebeuren. Een van de opties is dat de energie wordt vastgehouden door het materiaal en dat het licht wordt geabsorbeerd. Als we kijken naar het absorptiesignaal verkregen uit de absorptiemetingen, dan blijkt dat in de buurt van de energieniveaus van onze superstructuren, het absorptiespectrum een duidelijke piek vertoont (zoals weergegeven in figuur 4). Deze piek geeft aan dat de superstructuren het licht absorberen bij deze energieniveaus.

Welke informatie kunnen we uit de lichtabsorptiespectra halen? Wetenschappers van de Universiteit van Manchester hebben aangetoond dat hun 2D-grafeen (een materiaal gemaakt van koolstofatomen) een bepaalde hoeveelheid licht absorbeert, te weten 2.3 %, wat verband houdt met de tweedimensionale aard van het materiaal.[3] Ze hebben ook aangetoond dat één extra laag van het 2D-materiaal nog eens 2.3 % toevoegt aan het lichtabsorptievermogen. De metingen werden uitgevoerd op gesuspendeerd grafeen, wat betekent dat grafeen niet op een vast substraat werd aangebracht. Wetenschappers van de Universiteit van Californië verkregen min of meer dezelfde resultaten bij absorptiemetingen uitgevoerd op een ander 2D-materiaal, indiumarsenide (InAs).[4] De waarde van de lichtabsorptie was iets kleiner (1.6 %) dan de waarde die werd verkregen voor grafeen. De reden hiervoor is dat de meting niet is uitgevoerd op gesuspendeerd materiaal, maar op een substraat. De absorptiemeting werd uitgevoerd op InAs ondersteund door een calciumfluoridesubstraat. Dit substraat absorbeert ook een fractie van het licht.

Aangezien een dergelijke sterke absorptie een veelbelovend kenmerk is voor het gebruik van 2D-halfgeleiders in opto-elektronische apparaten, bestuderen we in **Hoofdstuk 3** de lichtabsorptie-eigenschappen van 2D PbSe en CdSe superstructuren met een vierkante en honingraatgeometrie. We tonen aan dat het absorptievermogen van een monolaag superstructur ongeveer 1.6 % is, onafhankelijk van het materiaal (CdSe of PbSe) en de geometrie (vierkant of honingraat). Figuur 4d, e en f tonen de absorptiespectra van alle

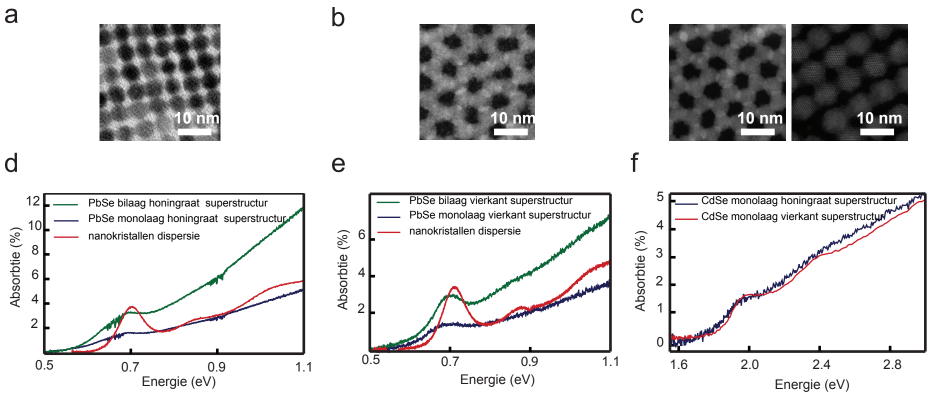

Figuur 4. TEM afbeeldingen en absorptiespectra van PbSe en CdSe vierkante en honingraat superstructuren. (a, b, c) Afbeeldingen van een deel van een PbSe en CdSe vierkant en honingraat superstructur (monolaag). (d, e) Absorptiespectra van een mono- en bilaag van PbSe superstructuren. De superstructuren absorberen 1.5 % van het licht bij een fotonenergie van 0.69 eV per monolaag. Een extra laag voegt nog eens 1.5 % toe aan de lichtabsorptie. Inzet: uitvergroting van de absorptiepiek in het energiebereik van 0.5 eV tot 0.9 eV. (f) Absorptiespectrum van een monolaag van CdSe honingraat en vierkante superstructuren. Ongeveer 1.65 % van het witte licht wordt geabsorbeerd bij 1.97 eV door de CdSe honingraat monolaag superstructuren.

superstructuren.

Elektronentransport in 2D-superstructuren

Elektrische geleidbaarheid en elektronenmobiliteit zijn andere opto-elektronische eigenschappen waarin we geïnteresseerd zijn voor onze superstructuren. Elektrische geleidbaarheid is een maat voor hoe goed een materiaal geschikt is voor het transport van elektrische lading. Elektronmobiliteit geeft aan hoe snel een elektron door een materiaal kan bewegen. De resultaten van dit onderzoek worden gepresenteerd in **Hoofdstuk 4**, **5** en **6**. De vergelijking in elektronenmobiliteit tussen vierkante en honingraat superstructuren kan ons meer informatie geven over het bestaan van Dirac-kegels in de bandstructuur van de honingraat superstructuren.

De elektrische geleiding en elektronenmobiliteit van onze superstructuren hebben we onderzocht met elektrochemische gating. De apparaten die voor deze techniek worden gebruikt, bestaan uit kamvormige in elkaar grijpende gouden elektroden (bron en afvoer) bovenop een glassubstraat (figuur 5a). De superstructuren zijn op deze gouden elektroden gebracht. Een elektrochemische cel met drie elektroden bestaat uit een werkelektrode (afvoer en bron), een tegenelektrode (TE) en een referentie-elektrode (figuur 5b). De potentiaal van de werkelektrode (WE) wordt gemeten ten opzichte van een referentie-elektrode (RE). De elektrochemische stroom vloeit in het werkelektrode-tegenelektrodecircuit. Om een potentiaal aan te brengen en de optredende stroom te meten, wordt het apparaat met de superroosters ondergedompeld in een elektrolyt, welke positieve ladingen bevat. Een schema van een elektrochemische cel met drie elektroden (WE, RE en TE) en een elektrolyt is weergegeven in figuur 5b.

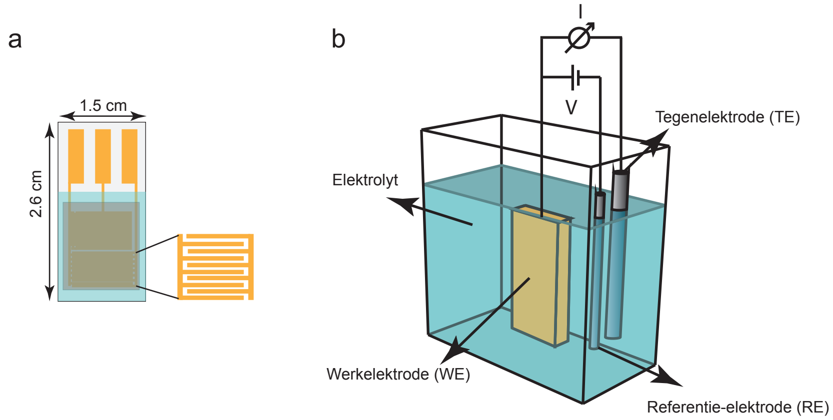

Figuur 5. Schematische weergave van de elektrodes en elektrochemische cel met drie elektroden die gebruikt worden voor de elektrochemische-gatingmetingen. (a) De systemen die gebruikt worden voor de metingen bestaan uit kamvormige in elkaar grijpende bron- en afvoerelektroden op een glassubstraat. (b) Elektrochemische cel met een werkelektrode (WE), een referentie-elektrode (RE) en een tegenelektrode (TE).

In **Hoofdstuk 4** en **5** bestuderen we de geleidbaarheid en elektronenmobiliteit van de PbSe vierkante en honingraat superstructuren. De elektronenmobiliteit, die bij kamertemperatuur uit elektrochemische-gatingmetingen is verkregen, ligt tussen 5 en 18 cm^2 $V^{-1}s^{-1}$. In **Hoofdstuk 6** laten we zien dat de vierkante en honingraat superstructuren van PbSe Nanokristallen via uitwisselingsreactie worden omgezet in superstructuren van CdSe. De elektronenmobiliteit waargenomen voor deze superstructuren is maximaal 10 cm^2 $V^{-1}s^{-1}$, wat vergelijkbaar is met de mobiliteit waargenomen voor de PbSe superstructuren in **Hoofdstuk 4** en **5**. De mobiliteitswaarden verkregen voor alle superstructuren (met slechts één monolaag) zijn vergelijkbaar of zelfs hoger dan de waarden verkregen voor een dikke laag andere nanokristallen. Dit betekent dat in de toekomst opto-elektronische apparaten gemaakt van superstructuren kleiner en goedkoper kunnen zijn. De elektronenmobiliteiten van vierkante superstructuren en de honingraat superstructuren zijn vrijwel gelijk. Daarom kunnen we het bestaan van Dirac-kegels in de honingraatstructuur van superstructuren niet bewijzen.

VI. Vooruitzichten

Hoewel de resultaten in dit proefschrift uitstekend zijn voor monolaag halfgeleiders, is de voorspelde Dirac-kegel niet waargenomen in de bandstructuur van de honingraat superstructuren. Alle metingen werden echter uitgevoerd bij kamertemperatuur. De berekende bandstructuur voor onze superstructuren laat een klein verschil tussen elke energielijn zien, wat betekent dat bij geringe thermische activatie de elektronen misschien niet op de positie van de Dirac-kegels zitten. Het uitvoeren van alle experimenten bij een lagere temperatuur kan daarom mogelijk het theoretisch voorspelde Dirac-karakter van de elektronen wel weergeven.

Literatuur

1. Graphene-Info: the graphene experts: *https://www.graphene-info.com/graphene-mobile-industry.*
2. Nextnano, Software for semiconductor nanodevices : *https://www.nextnano.de/nextnano3/tutorial/1Dtutorial_TightBinding_bulk_GaAs_GaP.htm.*
3. Nair, R. R. *et al.* Fine structure constant defines visual transparency of graphene. *Science* **320**, 1308 (2008).
4. Fang, H. *et al.* Quantum of optical absorption in two-dimensional semiconductors. *Proc. Natl. Acad. Sci.* **110**, 11688–11691 (2013).

List of publications

This thesis was based on the following publications:

Maryam Alimoradi Jazi, P. Tim Prins, Wiel H. Evers, Niall killilea, Christophe Delerue, Wolfgang Heiss, Arjan J. Houtepen and Daniel Vanmaekelbergh. “Investigation of the band structure of PbSe and CdSe nanocrystal superlattices with light absorption and photoconductivity spectroscopy.” *Submitted*

Maryam Alimoradi Jazi, Vera A. E. C. Janssen, Wiel H. Evers, Athmane Tadjine, Christophe Delerue, Laurens D. A. Siebbeles, Herre S. J. van der Zant, Arjan J. Houtepen and Daniel Vanmaekelbergh. Transport Properties of a Two-Dimensional PbSe Square Superstructure in an Electrolyte-Gated Transistor. *Nano Letters*, **17**, 5238-5243 (2017).

Maryam Alimoradi Jazi, Aditya Kulkarni, Sophia Buhbut Sinai, Joep L. Peters, Eva Geschiere, Michele Failla, Christophe Delerue, Arjan J. Houtepen, Laurens D. A. Siebbeles and Daniel Vanmaekelbergh. “Room-temperature electron transport in PbSe honeycomb superstructures studied in a transistor configuration and by terahertz spectroscopy.” *Submitted*

Maryam Alimoradi Jazi, Wiel H. Evers, Thomas Altantzis, Hans Vanrompay, Christophe Delerue, Sara Bals, Laurens D. A. Siebbeles, Arjan J. Houtepen and Daniel Vanmaekelbergh. “Room-temperature band occupation and electron transport in CdSe superlattices with square and honeycomb geometry.” *In preparation*

Other Publications:

Joep L. Peters, Thomas Altantzis, Ivan Lobato, Maryam Alimoradi Jazi, Carlo van Overbeek, Sara Bals, Daniel Vanmaekelbergh and Sophia Buhbut Sinai. Mono- and Multilayer Silicene-Type Honeycomb Lattices by Oriented Attachment of PbSe Nanocrystals: Synthesis, Structural Characterization, and Analysis of the Disorder. *Chem. Mater.* **30**, 4831–4837 (2018).

Maryam Alimoradi Jazi,Tobias Meisch, Martin Klein and Ferdinand Scholz. Defect reduction in GaN regrown on hexagonal mask structure by facet assisted lateral overgrowth. J. *Cryst. Growth*, **429**, 13-18 (2015).

Tobias Meisch, Maryam Alimoradi Jazi, Martin Klein and Ferdinand Scholz. (20-21) MOVPE and HVPE GaN grown on patterned sapphire substartes. *Phys. Status Solidi C*, **11**, 537-540 (2014).

Conference contributions and presentations

Oct 2018	**Band occupation and charge transport in PbSe & CdSe nanocrystal superlattices** (oral) at nanoGe Fall Meeting, Torremolinos, Málaga, Spain
Jun 2018	**Quantum of optical absorption and band occupation in 2D PbSe and CdSe nanocrystal superlattices** (oral) at the 10th Biannual Conference on Quantum Dots, Toronto, Canada
Jun 2018	**Band occupation and charge transport in PbSe nanocrystal superlattices** (poster) at the 10th Biannual Conference on Quantum Dots, Toronto, Canada
Jun 2018	**Transport properties of 2D PbSe square superlattices in an electrolyte gated transistor** (invited talk) at the 19th Congress on Materials Science and Engineering, Barcelona, Spain
Jul 2017	**Transport properties of a 2D CdSe square superstructure** (oral) at Nanoscience and Nanocrystals, Braga, Portugal
Jul 2017	**Transport properties of a 2D PbSe square superstructure** (poster) Physical School on Applied Photonics, Bad Honnef, Germany
Sep 2016	**Electronic charging and transport in 2D CdSe superstructure** (oral) International Conference on Solution Based 2D Nanomaterials, Berlin, Germany
Aug 2015	**Investigation of transport properties of 2D semiconductor nanocrystals by electrochemical gating** (Poster) at the NanoSa15 conference, Dresden, Germany

About the Author

Maryam Alimoradi Jazi was born in Isfahan, Iran, on 22nd December 1984. She obtained her high school diploma from Safura High school in 2003. In September of the same year, she attended a Pre-university program for one year, after which she started her Bachelor degree (BEng) in Electrical Engineering-electronics at University of Isfahan. After obtaining her BEng in 2009, she worked as a mathematics and physics teacher till 2011. She entered a Master program, Energy Science and Technology, on October 2011at Ulm University in Germany and received her MSc degree in 2013 with a thesis entitled "Epitaxial growth of (20-21) GaN on (22-43) sapphire substrate by means of MOVPE", under supervision of Prof. Ferdinand Scholz. After obtaining her MSc degree, she worked as a research assistant at Institute of Functional Nanosystems, Optoelectronics Division where she deepened her knowledge on semiconductor materials. During this time, she was a teaching assistant for "Electrical Engineering" course of the energy Science and Technology program at Ulm University.

In March 2015, Maryam started her PhD at Condensed Matter and Interfaces (CMI) at Utrecht University under the supervision of Prof. Daniel Vanmaekelbergh and Dr. Arjan Houtepen. During her PhD, she studied optoelectronic properties of two-dimensional (2D) PbSe and CdSe semiconductor superlattices. Most of the results presented in this thesis have been published in international scientific journals and presented at several international conferences. During her PhD, she supervised three bachelor students and second-year research projects. Furthermore, she was a teaching assistant for the "quantum chemistry"course.

دمای اتاق و به‌دست آمده از اندازه‌گیری‌های الکتروشیمیایی، بین 5 تا 18 سانتی‌متر مربع در یک ثانیه به ازای یک ولت پتانسیل اعمال شده ($cm^2\,V^{-1}\,s^{-1}$) می‌باشد. در فصل 6، تبدیل ابرشبکه‌های PbSe توسط روش تبادل به ابرشبکه‌های CdSe، نشان داده می‌شود. تحرک الکترون‌های مشاهده شده برای این ابرشبکه‌ها به حداکثر مقدار 10 سانتی‌متر مربع در یک ثانیه به ازای یک ولت پتانسیل اعمال شده می‌رسد که این مقدار با مشاهدات ابرشبکه‌های PbSe مشاهده شده در فصل‌های 4 و 5 قابل مقایسه می‌باشد. میزان تحرک الکترون‌ها برای همه‌ی ابرشبکه‌ها (با تنها یک لایه ضخامت)، مشابه یکدیگرند. تحرک الکترون‌ها در ابرشبکه‌های بیان شده در این پایان نامه، مقدار مشابه و حتی بیشتر از تحرک الکترون‌های اندازه‌گیری شده در لایه‌های ضخیم ساخته شده از نانوکریستال‌های دیگر دارند. این بدین معناست که وسایل الکترونیکی ساخته شده در آینده‌ای نه چندان دور می‌توانند کوچکتر و حتی بسیار مقرون به صرفه‌تر شوند. نکته قابل توجه دیگر آنست که تحرک الکترون‌ها برای ابرشبکه‌های مربعی و لانه زنبوری بسیار مشابهند. بنابراین نمی‌توان وجود مخروطهای دیراکی در ساختار نواری ابرشبکه‌های لانه زنبوری را اثبات کرد.

4- چشم انداز

با وجود اینکه نتایج ارائه شده در این پایان نامه نتایجی بسیار چشم‌گیر برای نیمه‌هادی‌هایی با تنها یک لایه ضخامت می‌باشند، ما هیچ‌گونه نشانه‌ای از وجود مخروطهای دیراکی در ساختار نواری ابرشبکه‌های لانه زنبوری مشاهده نمی‌کنیم. قابل ذکر است که تمامی آزمایشات این پایان‌نامه در دمای اتاق انجام شده‌اند. ساختار نواری محاسبه شده برای ابرشبکه‌ها اختلاف بسیار کمی را مابین هر خط انرژی نشان می‌دهد. این بدین معناست که اگر الکترون‌ها دارای انرژی گرمایی اندکی باشند، ممکن است نتوانند در مخروطهای دیراکی قرار گیرند. بنابراین انجام آزمایشات فوق در دمای بسیار پایین می‌تواند در نهایت اثر وجود مخروطهای دیراکی را درنتایج آزمایشات آشکار سازد.

مراجع

1. Graphene-Info: the graphene experts: https://www.graphene-info.com/graphene-mobileindustry.

2. Nextnano, software for semiconductor nanodevices: https://www.nextnano.de/nextnano3/tutorial/1Dtutorial_TightBinding_bulk_GaAs_GaP.htm.

3. Nair, R. R. *et al.* Fine structure constant defines visual transparency of graphene. *Science* **320**, 1308 (2008).

4. Fang, H. *et al.* Quantum of optical absorption in two-dimensional semiconductors. *Proc. Natl. Acad. Sci.* **110**, 11688–11691 (2013).

مقایسه‌ی تحرک الکترون‌ها در دو ابرشبکه مربعی و لانه زنبوری می‌تواند اطلاعات زیادی را در مورد وجود مخروطهای دیراکی پیش‌بینی شده در ساختار نواری ابرشبکه‌های لانه زنبوری فراهم آورد. روش استفاده شده برای بررسی این خواص اپتوالکترونیکی ترانزیستورهای الکتروشیمیایی[1] می‌باشد. ادوات مورد استفاده برای این اندازه‌گیری‌ها شامل الکترودهای به هم متصل شده از جنس طلا (سورس و درین[2]) برروی شیشه می‌باشد (شکل5 (الف)). ابرشبکه‌ها پس از تشکیل شدن بر لایه‌ی مایع چسبناک برروی این الکترودهای طلا انتقال داده می‌شوند. سلول الکتروشیمیایی استفاده شده‌در این آزمایشات دارای الکترود کار[3] (WE)، الکترود شمارنده[4] (CE) و الکترود مرجع[5] (RE) می‌باشد (شکل5 (ب)). پتانسیل الکترود کار با توجه به الکترود مرجع اندازه‌گیری می‌شود. جریان الکتروشیمیایی در مدار الکترود کار – الکترود شمارنده جاری می‌شود. جهت اعمال پتانسیل و اندازه‌گیری جریان، دستگاه شامل ابرشبکه‌ها درون حلال الکترولیت که شامل یون‌های مثبت است، قرار داده می‌شود. طرح کلی یک سلول الکتروشیمیایی سه الکترودی شامل الکترولیت، الکترود کار، الکترود شمارنده و الکترود مرجع در شکل5 (ب) نمایش داده شده است.

در فصل 4 و 5، به بررسی و مطالعه‌ی رسانایی الکتریکی و تحرک الکترون‌ها در ابرشبکه‌های مربعی و لانه زنبوری ساخته شده از نانوکریستال‌های PbSe می‌پردازیم. تحرک الکترون‌های اندازه‌گیری شده در

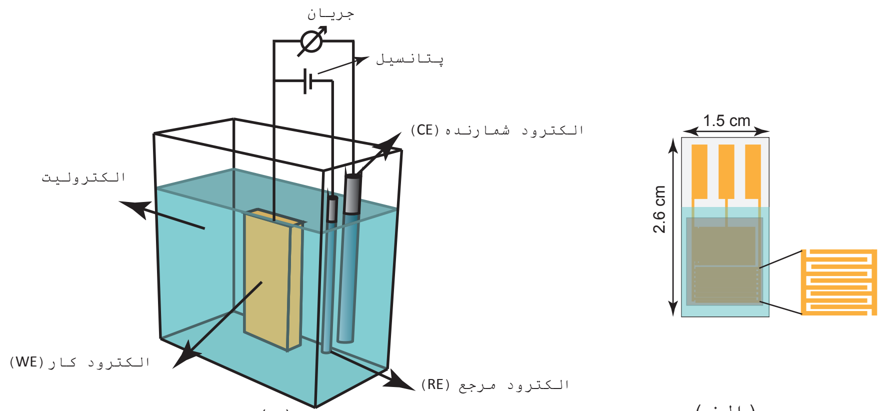

(ب) (الف)

شکل 5 – نمایی از طراحی سلول الکتروشیمیایی سه الکترودی برای اندازه‌گیری رسانایی الکتریکی و تحرک الکترون‌ها در ابرشبکه‌های دوبعدی، الف) دستگاه استفاده شده شامل الکترودهای به هم وصل شده از جنس طلا بر روی شیشه، ب) سلول الکتروشیمیایی سه الکترودی شامل الکترود کار، الکترود شمارنده و الکترود مرجع.

---

[1] Electrochemical gating
[2] Source and drain
[3] Working electrode (WE)
[4] Counter electrode (CE)
[5] Reference electrode (RE)

اضافه خواهد کرد. لازم به ذکر است که اندازه‌گیری جذب نور در این آزمایشات برروی گرافین‌های معلق صورت گرفته است و این بدین معناست که گرافین برروی هیچ جسم دیگری (مانند شیشه) قرار نگرفته است. گروه دیگری از دانشمندان دانشگاه کالیفرنیا نتایج مشابهی از اندازه‌گیری جذب نور بر مواد دوبعدی دیگر، آرسنید ایندیوم، را به‌دست آورده‌اند.[4] با این‌حال، مقدار نور جذب شده توسط این ماده اندکی کمتر (1.6 %) از مقدار نور جذب شده توسط گرافین است. دلیل این اختلاف اندک این است که اندازه‌گیری آن‌ها برروی آرسنید ایندیوم‌های معلق صورت نگرفته است، بلکه این مواد دوبعدی برروی جسم جامدی همچون فلوراید کلسیم قرار گرفته‌اند. فلوراید کلسیم نیز بخشی از نور را جذب خواهد کرد و این باعث کاهش جذب نور توسط خود آرسنید ایندیوم می‌شود.

از آنجا که چنین جذب بالایی از نور یک ویژگی امیدبخش در عرصه‌ی استفاده از نیمه‌هادی‌های دوبعدی در وسایل اپتوالکترونیکی می‌باشد، در فصل 3 این کتاب به بررسی جذب نور توسط ابرشبکه‌های خود پرداخته‌ایم. نشان داده می‌شود که این ابرشبکه‌ها تقریبا 1.6 % نور را، مستقل از نوع (PbSe یا CdSe) و طرح (مربع یا لانه زنبوری) آنها، جذب می‌کنند. شکل 4 (د)، (ه) و (و) نمودارهای جذب نور را برای تمام ابرشبکه‌ها نشان می‌دهد.

2-3 حرکت الکترون‌ها در ابرشبکه‌های دو بعدی

رسانایی الکتریکی و تحرک الکترون‌ها، دو خاصیت اپتوالکترونیکی دیگری هستند که به بررسی آن‌ها پرداخته‌ایم. رسانایی الکتریکی نشان‌دهنده میزان جابجایی الکترون‌ها در ماده است درحالی‌که تحرک الکترون‌ها نشان می‌دهد که الکترون‌ها با چه سرعتی در یک ماده قابلیت جابجایی دارند.

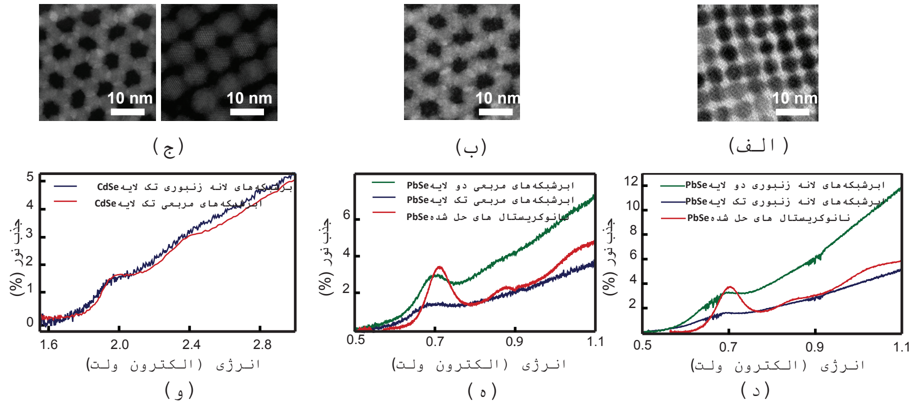

شکل 4 - (الف، ب و ج) تصاویر قسمتی از ابرشبکه‌های مربعی و لانه زنبوری PbSe و CdSe گرفته شده توسط میکروسکوپ الکترونی عبوری. (د و ه) نمودار جذب نور برای تک لایه و دو لایه‌ی ابرشبکه‌های PbSe. برای ابرشبکه‌هایی با تنها یک لایه ضخامت برروی کوارتز، مقدار جذب نور در انرژی 0.69 الکترون ولت برابر 1.5 % می‌باشد. اضافه کردن یک لایه دیگر، 1.5 % جذب نور را افزایش خواهد داد. (و) نمودار جذب نور برای یک لایه از ابرشبکه‌های CdSe. این ابرشبکه‌ها 1.65 % از نور را جذب می‌کنند.

نانوکریستال‌های CdSe امکان‌پذیر نمی‌باشد. به منظور بدست آوردن ابرشبکه‌های CdSe، ما ابرشبکه‌های pbSe را توسط یک واکنش تبادلی به ابرشبکه‌های CdSe تبدیل می‌کنیم. در این روش اتم‌های سرب با اتم‌های کادمیوم جایگزین خواهند شد. بدین منظور، ابرشبکه‌های تشکیل شده بر سطح مایع چسبناک را برروی هر بستر دلخواه، مانند شیشه، انتقال می‌دهیم. محلولی شامل عنصر کادمیوم آماده می‌کنیم و ابرشبکه‌های قرار گرفته بر روی بستر را درون محلول قرار می‌دهیم. سپس دمای محلول را تا 150 درجه‌ی سانتیگراد افزایش می‌دهیم. در این دمای بالا، اتم‌های سرب در ابرشبکه‌ها با اتم‌های کادمیوم در محلول جایگزین خواهند شد و در پایان ابرشبکه‌های CdSe بدست خواهند آمد.

3- خواص اپتوالکترونیکی ابرشبکه‌های دوبعدی

همانطور که قبلا اشاره شد، ما به تحلیل و بررسی خواص اپتوالکترونیکی ابرشبکه‌های ذکرشده توجه ویژه‌ای خواهیم داشت.

خواص اپتوالکترونیکی چه مفهومی دارند؟ اپتوالکترونیک، از دیدگاه علمی، با نور، آشکارسازی آن، ایجاد و دستکاری آن برای اهداف مختلف سروکار دارد. ابرشبکه‌های دوبعدی ما دارای پتانسیل بالایی برای استفاده در وسایل الکترونیکی مانند ترانزیستورها و یا وسایل اپتوالکترونیکی مانند سلول‌های خورشیدی و حسگرهای نوری هستند. در ادامه، خواص اپتوالکترونیکی ابرشبکه‌های دوبعدی خود را مطالعه و بررسی خواهیم کرد.

3-1- جذب نور توسط ابرشبکه‌های دوبعدی

طیف‌سنجی جذب نور یکی از تکنیک‌های استفاده شده در بررسی خواص اپتوالکترونیکی ابرشبکه‌هاست. نتایج به‌دست آمده از این بررسی در فصل 3 این کتاب ارائه شده است. در پدیده‌ی جذب نور، فرکانس موج نور تابیده شده دقیقا معادل یا نزدیک به سطح‌های انرژی الکترون‌ها در مواد است. بنابراین، الکترون‌ها انرژی موج نور را جذب کرده و در نتیجه سطح انرژی خود را تغییر خواهند داد. در این‌حالت، گزینه‌های متعددی برای آنچه که بعدا اتفاق می‌افتد وجود دارد. یکی از این موارد این است که این انرژی حفظ شده و توسط ماده جذب می‌شود. اگر با دقت به نمودار جذب نوری که از آزمایش طیف سنجی جذب نور به‌دست آمده توجه کنیم، طیف نور جذب شده حداکثری را نشان می‌دهد (مطابق شکل 4) که این مقدار حداکثر بیانگر جذب موج نور در آن دسته از انرژی‌ها می‌باشد. حال سوال مهم آنست که از این آزمایش بر روی ابرشبکه‌ها، چه اطلاعاتی می‌توان به‌دست آورد.

دانشمندان در دانشگاه منچستر نشان داده‌اند که گرافین‌های دوبعدی (مواد ساخته شده از اتم‌های کربن) مقدار مشخصی (تقریبا 2.3 %) از نور را جذب می‌کنند. آنها بر این باورند که این درصد به دو بعدی بودن این مواد ارتباط دارد.[3] علاوه بر آن، آنها نشان داده‌اند که اضافه کردن یک لایه‌ی دیگر از گرافین 2.3 % دیگر به میزان جذب نور

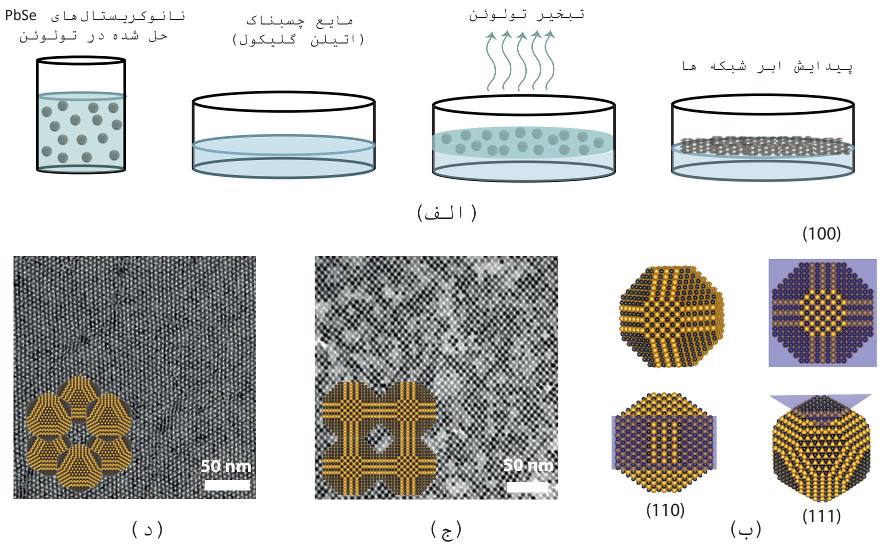

شکل 3 – الف) نمایش الگودار سیستم آزمایشی که برای تشکیل ابرشبکه‌های مربعی و لانه زنبوری از نانوکریستال‌های PbSe استفاده شده است. ما از نانومکعب‌های صفحه‌دار شده در یک محلول استفاده می‌کنیم. محلول رقیق شده‌ی نانوکریستال‌ها برروی یک لایه از مایع چسبناک (اتیلن گلیکول) ریخته می‌شود و بعد از مدت اندکی حلال تولوئن تبخیر می‌شود. نانوکریستال‌ها توسط صفحه‌های {100} خود به یکدیگر متصل شده و سورلتیس‌های دوبعدی با ساختار مربعی و لانه زنبوری را تشکیل می‌دهند. ب) طرح اتمی مکعب‌های صفحه‌دار نانوکریستال‌های PbSe شامل 6 صفحه‌ی {100}، 12 صفحه‌ی {110} و 8 صفحه‌ی {111}. دایره‌های مشکی (زرد) نمایشگر اتم‌های سرب (سلنیوم) هستند. ج) تصویر قسمتی از ابرشبکه مربعی PbSe گرفته شده توسط میکروسکوپ الکترونی عبوری[1]. نانوکریستال‌های PbSe توسط 4 صفحه از 6 صفحه‌ی {100} به یکدیگر متصل شده‌اند، همانطور که در شکل الحاق مشاهده می‌شود. د) تصویر قسمتی از ابرشبکه لانه زنبوری PbSe گرفته شده توسط میکروسکوپ الکترونیکی عبوری. نانوکریستال‌های PbSe توسط 3 صفحه از 6 صفحه‌ی {100} به یکدیگر متصل شده‌اند. تصویر الحاقی: طرح اتمی شش نانوکریستال در طرح ابرشبکه لانه زنبوری که توسط 3 صفحه‌ی {100} خود به یکدیگر متصل شده‌اند و یک ساختار دو لایه تشکیل داده‌اند.

نانوکریستال‌ها توسط چهارصفحه از شش صفحه‌ی {100} خود به یکدیگر متصل می‌شوند، همانطور که در شکل الحاقی به شکل3 (ج) مشاهده می‌شود. در ابرشبکه‌های لانه زنبوری، نانوکریستال‌ها توسط سه صفحه از شش صفحه‌ی {100} خود به یکدیگر متصل می‌شوند و یک ساختار دو لایه تشکیل می‌دهند (شکل 3 (د)).

برخلاف نانوکریستال‌های PbSe، نانوکریستال‌های CdSe مکعبی شکل نیستند بلکه به‌صورت کروی هستند. بنابراین به‌دلیل عدم وجود صفحه‌ها در سطح این نانوکریستال‌ها، تشکیل ابرشبکه‌ها به‌طور مستقیم از

---

[1] Transmission Electron Microscope (TEM)

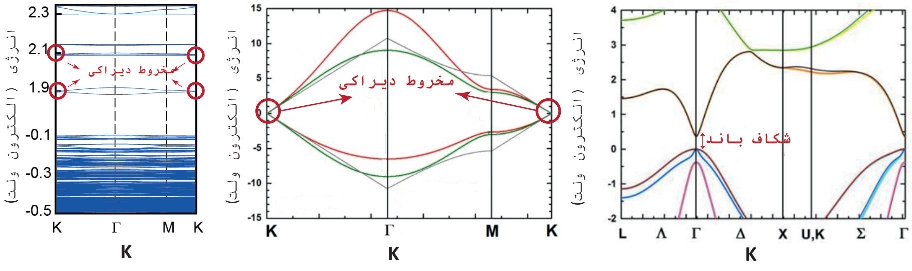

(ج) (ب) (الف)

شکل 2 – ساختار نواری الف) آرسنید ایندیوم[2] ب) گرافین با پیدایش مخروطهای دیراکی[2] و ج) ابرشبکه‌های لانه زنبوری سلنید کادمیوم. مخروطهای دیراکی نقاطی هستند که خطوط انرژی به هم می‌رسند.

در "مخروط دیراکی" خطوط انرژی به هم می‌رسند، در این نقاط هیچگونه شکاف انرژی وجود ندارد. این بدین معناست که الکترون‌ها می‌توانند سریع‌تر و آسان‌تر حرکت کنند اگر دارای انرژی کافی برای قرار گرفتن در نقاط مخروطهای دیراکی باشند. دانشمندان بر این باور هستند که این خاصیت گرافین برگرفته از طرح شش ضلعی آن است. بنابراین، انتظار می‌رود مخروطهای دیراکی در ساختار نواری ابرشبکه‌های لانه زنبوری نیز مشاهده شود. محاسبات تئوری، همانطور که در شکل2 (ج) نشان داده شده است، پیش‌بینی وجود مخروطهای دیراکی در ساختار نواری این ابرشبکه‌ها را تایید می‌کنند.

2- پیدایش ابرشبکه‌های دوبعدی

ابرشبکه‌های دوبعدی با طرح مربعی و لانه زنبوری با استفاده از روش لایه‌ی مایع[1] آماده می‌شوند. این روش در شکل3 (الف) نشان داده شده است. در اینجا نانوکریستال‌های PbSe را در یک حلال، معمولا تولوئن[2]، رقیق می‌کنیم. نانوکریستال‌های PbSe به شکل مکعب هستند، با این‌حال آنها یک مکعب کامل نیستند. برش‌هایی در گوشه‌ها و لبه‌های این نانوکریستال‌ها وجود دارند. این برش‌ها در سطح نانوکریستال‌ها صفحه‌هایی را ایجاد می‌کنند. این نانومکعبهای بریده شده، همانطور که در شکل3 (ب) نشان داده شده‌اند، دارای شش صفحه در راستای {100}، 12 صفحه در راستای {110} و 8 صفحه در راستای {111} هستند. محلول رقیق شده‌ی نانوکریستال‌ها بر روی یک لایه از مایع چسبناک (اتیلن گلیکول) ریخته می‌شود و بعد از مدت اندکی حلال تولوئن تبخیر می‌شود. نانوکریستال‌ها توسط صفحه‌های {100} خود به یکدیگر متصل می‌شوند و ابرشبکه‌های دوبعدی با ساختار مربعی و لانه زنبوری با تنها یک لایه ضخامت را تشکیل می‌دهند (شکل 3 (ج) و (د)). در ابرشبکه‌های مربعی،

---

[1] Liquid substrate procedure
[2] Toluene

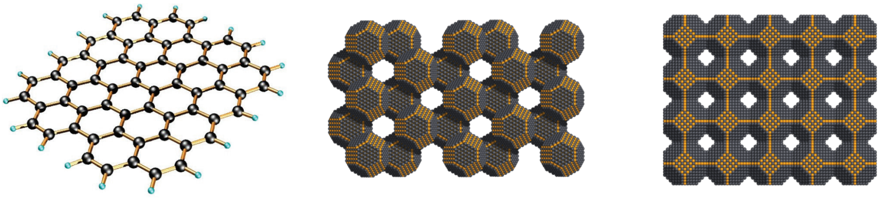

(الف) (ب) (ج)

شکل 1 – طرح اتمی الف) ابرشبکه‌های مربعی، ب) لانه زنبوری ساخته شده از نانوکریستال‌های PbSe. دایره‌های مشکی (زرد) نشان‌دهنده‌ی اتم‌های سرب (سلنیوم) هستند. ج) گرافین ساخته شده از اتم‌های کربن[1] (دایره‌های مشکی نشان‌دهنده اتم‌های کربن هستند).

(لانه زنبوری) شکل گرفته‌اند. این تک لایه‌ها ابرشبکه‌های دوبعدی نامیده می‌شوند. شکل1 (الف) و (ب) طرح اتمی ابرشبکه‌های مربعی و لانه زنبوری ساخته شده از نانوکریستال‌های PbSe را نشان می‌دهد. دلیل علاقه‌مندی ما به ابرشبکه‌های دوبعدی، الهام گرفتن از گرافین[1] است که همانطور که در شکل1 (ج) نشان داده شده است، دارای یک طرح شش‌ضلعی است. گرافین دارای خواص ویژه‌ای است که در ادامه به آن خواهیم پرداخت.

پیش از بررسی خاصیت ویژه گرافین، به مفهوم جدیدی در علم فیزیک به نام "ساختار نواری[2]" می‌پردازیم. همان‌طور که قبلا اشاره شد، مواد براساس حرکت الکترون‌ها به سه دسته رسانا، نارسانا و نیمه‌هادی‌ها تقسیم می‌شوند. محدوده انرژی‌ای که این الکترون‌ها (درون مواد) ممکن است داشته باشند و محدوده‌ای از انرژی‌هایی که ممکن است در آنها وجود نداشته باشد ("نوارهای ممنوعه[3]" یا "شکاف باند[4]") می‌تواند با "ساختار نواری" توصیف شود. ساختار نواری مواد می‌تواند با روش‌های مختلف محاسبه گردد. دانشمندان اطلاعات بسیار زیادی از ساختار نواری مواد بدست می‌آورند.

ساختار نواری آرسنید ایندیوم[5] (InAs) به‌عنوان مثال در شکل2 (الف) نشان داده شده است. هر خط در ساختار نواری نشان‌دهنده‌ی انرژی‌ای است که هر الکترون می‌تواند داشته باشد. عدم وجود خط به معنای وجود شکاف باند است. خاصیت ویژه گرافین حاصل ساختار نواری منحصر بفرد آن است، همانطور که در شکل2 (ب) نشان داده شده است. نقاطی در ساختار نواری گرافین وجود دارند که خطوط انرژی در آن‌ها به یکدیگر

---

[1] Graphene

[2] Band structure

[3] Forbidden bands

[4] Band gap

[5] Indium arsenide

1- مقدمه

پژوهش‌های به عمل آمده در این پایان‌نامه بر خواص اپتوالکترونیکی ابرشبکه‌های دوبعدی[1] ساخته شده از نانوکریستال‌های نیمه‌هادی تمرکز دارد. اما نانوکریستال‌های نیمه‌هادی چیست؟ دوبعدی بودن چه معنایی دارد و چگونه این ابرشبکه‌های دوبعدی ساخته می‌شوند؟ خواص اپتوالکترونیکی چیست و چگونه آن‌را برای ابرشبکه‌های دوبعدی‌مان اندازه گرفتیم؟ در این فصل به تمامی این سوالات پاسخ خواهیم داد.

نیمه‌هادی‌ها[2] چیستند؟ مواد می‌توانند براساس خواص خود به دسته‌های مختلف تقسیم شوند. می‌توان آنها را به سه دسته‌ی رسانا، نارسانا و نیمه‌هادی‌ها تقسیم کرد. این طبقه‌بندی براساس حرکت الکترون‌ها (جریان الکتریکی) در مواد انجام شده است. رساناها موادی هستند که الکترون‌ها به‌راحتی در آن‌ها حرکت می‌کنند مانند نقره و مس. در مقابل رساناها، عایق‌ها قرار دارند. نارساناها در مقابل حرکت الکترون‌ها مقاومت می‌کنند. شیشه، پلاستیک و کاغذ نمونه‌های خوبی از نارساناها هستند. نیمه‌هادی‌ها عملکردی بینابین رساناها و نارساناها دارند. در یک نیمه‌هادی چنانچه انرژی لازم به الکترون‌ها داده شود، الکترون‌ها قابلیت حرکت خواهند داشت. سیلیکون یکی از پراستفاده‌ترین نیمه‌هادی‌هاست.

نانوکریستال‌ها[3] چیستند؟ کریستال یک ماده جامد است که اجزای تشکیل‌دهنده‌ی آن (مانند اتم‌ها یا مولکول‌ها) در یک الگوی تکرار شونده مرتب شده‌اند. شکر، دانه‌های برف و سنگ‌های قیمتی همچون الماس و کوارتز، همگی کریستال هستند. پیشوند "نانو" به معنای "میلیاردم" است، بنابراین یک نانومتر یک میلیاردم متر است. ما در دنیای متر و کیلومتر به عنوان مقیاس اندازه زندگی می‌کنیم، بنابراین تصور یک شیء به این کوچکی بسیار دشوار است. امیدوارم مثال‌های زیر بتواند به شما برای استنباط مفهوم "مقیاس نانو" کمک کند. یک قطعه کاغذ معمولا دارای ضخامتی در حدود 10000 نانومتر است. اگر شما یکی از تارهای موی خود را در راستای طولی آن به صد هزار قطعه قسمت کنید، هر قطعه یک نانومتر است. یک نانو کریستال یک کریستال است که حداقل یکی از ابعاد آن در مقیاس نانومتر است. در تحقیقات ما، نانوکریستال‌های سلنید سرب[4] (PbSe) و سلنید کادمیوم (CdSe)[5] با ابعاد 6.3 – 5.5 نانومتر استفاده شده‌اند.

مواد دوبعدی چه موادی هستند؟ مواد دوبعدی، موادی که گاهی اوقات به عنوان مواد تک لایه شناخته می‌شوند، موادی هستند که شامل تنها یک لایه از اتم‌ها می‌باشند. در پژوهش‌های ما، یک لایه (تک لایه) به هم متصل شده از نانوکریستال‌های PbSe و CdSe در طرح‌های مربع و شش ضلعی

---

[1] 2D superlattices

[2] Semiconductor

[3] Nanocrystal

[4] Lead Selenide

[5] Cadmium Selenide

خلاصه به زبان فارسی

چکیده

در این فصل، خلاصه ای بر تحقیقات انجام شده در پایان نامه خواهیم داشت. ابتدا مقدمه‌ای مختصر درباره‌ی نیمه‌هادی‌ها و نانوکریستال‌ها ارائه خواهد شد، سپس نتایج اصلی به‌دست آمده در این پایان‌نامه و آزمایشات درنظر گرفته شده برای ادامه تحقیقات حاضر بیان خواهند شد.

ابر شبکه های شارژ شده

اشغال ساختار باند و انتقال الکترون در ابر شبکه های دو بعدی ساخته شده از نانوکریستال های سلنید سرب و سلنید کادمیم